

Jordan Journal of P H Y S I C S

An International Peer-Reviewed Research Journal

Volume 13, No. 2, August 2020, Muharram 1442 H

Jordan Journal of Physics (JJP): An International Peer-Reviewed Research Journal funded by the Scientific Research Support Fund, Jordan, and published biannually by the Deanship of Research and Graduate Studies, Yarmouk University, Irbid, Jordan.

EDITOR-IN-CHIEF:

Ibrahim O. Abu Al-Jarayesh

Department of Physics, Yarmouk University, Irbid, Jordan.

ijarayesh@yu.edu.jo

EDITORIAL BOARD:	ASSOCIATE EDITORIAL BOARD
<p>Prof. Nabil Y. Ayoub <i>President, American University of Madaba, Madaba, Jordan.</i> nabil.ayoub@ju.edu.jo</p> <p>Prof. Marwan S. Mousa <i>Department of Physics, Mu'tah University, Al-Karak, Jordan.</i> mmousa@mutah.edu.jo</p> <p>Prof. Jamil M. Khalifeh <i>Department of Physics, University of Jordan, Amman, Jordan.</i> jkalifa@ju.edu.jo</p> <p>Prof. Abdalmajeid M. Alyassin <i>Department of Physics, Yarmouk University, Irbid, Jordan.</i> alyassin@yu.edu.jo</p> <p>Prof. M-Ali H. Al-Akhras (AL-Omari) <i>Department of Physics, Jordan University of Science & Technology, Irbid, Jordan.</i> alakmoh@just.edu.jo</p> <p>Prof. Mohammad Al-Sugheir <i>Department of Physics, The Hashemite University, Zarqa, Jordan.</i> msugh@hu.edu.jo</p> <p>Prof. Tareq F. Hussein <i>Department of Physics, The University of Jordan, Amman, Jordan.</i> t.hussein@ju.edu.jo</p> <p>Prof. Ibrahim A. Bsoul <i>Department of Physics, Al al-Bayt University, Mafrqa, Jordan.</i> Ibrahimbsoul@yahoo.com</p>	<p>Prof. Mark Hagmann <i>Desert Electronics Research Corporation, 762 Lacey Way, North Salt Lake 84064, Utah, U. S. A.</i> MHagmann@NewPathResearch.Com</p> <p>Dr. Richard G. Forbes <i>Dept. of Electrical and Electronic Engineering, University of Surrey, Advanced Technology Institute and Guildford, Surrey GU2 7XH, UK.</i> r.forbes@surrey.ac.uk</p> <p>Prof. Roy Chantrell <i>Physics Department, The University of York, York, YO10 5DD, UK.</i> roy.chantrell@york.ac.uk</p> <p>Prof. Susamu Taketomi <i>2-35-8 Higashisakamoto, Kagoshima City, 892-0861, Japan.</i> staketomi@hotmail.com</p>

Editorial Secretary: Majdi Al-Shannaq.

Languages Editor: Haider Al-Momani

Manuscripts should be submitted to:

Prof. Ibrahim O. Abu Al-Jarayesh
Editor-in-Chief, Jordan Journal of Physics
Deanship of Research and Graduate Studies
Yarmouk University-Irbid-Jordan
Tel. 00 962 2 7211111 Ext. 2075
E-mail: jjp@yu.edu.jo
Website: <http://Journals.yu.edu.jo/jjp>

Jordan Journal of P H Y S I C S

An International Peer-Reviewed Research Journal

Volume 13, No. 2, August 2020, Muharram 1442 H

INTERNATIONAL ADVISORY BOARD

Prof. Dr. Ahmad Saleh

Department of Physics, Yarmouk University, Irbid, Jordan.
salema@yu.edu.jo

Prof. Dr. Aurore Savoy-Navarro

LPNHE Université de Paris 6/IN2P3-CNRS, Tour 33, RdC 4,
Place Jussieu, F 75252, Paris Cedex 05, France.
auore@lphnhep.in2p3.fr

Prof. Dr. Bernard Barbara

Laboratoire Louis Neel, Salle/Room: D 108, 25, Avenue des
Martyrs BP 166, 38042-Grenoble Cedex 9, France.
Barbara@grenoble.cnrs.fr

Prof. Dr. Bruno Guiderdoni

Observatoire Astronomique de Lyon, g, avenue Ch. Antre-F-69561,
Saint Genis Laval Cedex, France.
Bruno.guiderdoni@olos.univ-lyon1.fr

Prof. Dr. Buford Price

Physics Department, University of California, Berkeley, CA 94720,
U. S. A.
bprice@berkeley.edu

Prof. Dr. Colin Cough

School of Physics and Astronomy, University of Birmingham, B15
2TT, U. K.
c.cough@bham.ac.uk

Prof. Dr. Desmond Cook

Department of Physics, Condensed Matter and Materials Physics
Research Group, Old Dominion University, Norfolk, Virginia
23529, U. S. A.
Dcook@physics.odu.edu

Prof. Dr. Evgeny Sheshin

MIPT, Institutskij per. 9, Dogoprudnyi 141700, Russia.
sheshin@lafaet.mipt.ru

Prof. Dr. Hans Ott

Laboratorium fuer Festkorperphysik, ETH Honggerberg, CH-
8093 Zurich, Switzerland.
ott@solid.phys.ethz.ch

Prof. Dr. Herwig Schopper

President SESAME Council, Chairman Scientific Board UNESCO
IBSP Programme, CERN, 1211 Geneva, Switzerland.
Herwig.Schopper@cern.ch

Prof. Dr. Humam Ghassib

Department of Physics, The University of Jordan, Amman 11942,
Jordan.
humamg@ju.edu.jo

Prof. Dr. Khalid Tougan

Chairman of Jordan Atomic Energy Commission, Amman, Jordan.

Prof. Dr. Nasr Zubeidev

President: Al-Zaytoonah University of Jordan, Amman, Jordan.
President@alzaytoonah.edu.jo

Prof. Dr. Patrick Roudeau

Laboratoire de l'Accelérateur, Lineaire (LAL), Université Paris-
Sud 11, Batiment 200, 91898 Orsay Cedex, France.
roudeau@mail.cern.ch

Prof. Dr. Paul Chu

Department of Physics, University of Houston, Houston, Texas
77204-5005, U. S. A.
Ching-Wu.Chu@mail.uh.edu

Prof. Dr. Peter Dowben

Nebraska Center for Materials and Nanoscience, Department of
Physics and Astronomy, 255 Behlen Laboratory (10th and R
Streets), 116 Brace Lab., P. O. Box 880111, Lincoln, NE 68588-
0111, U. S. A.
pdowben@unl.edu

Prof. Dr. Peter Mulser

Institute fuer Physik, T.U. Darmstadt, Hochschulstr. 4a, 64289
Darmstadt, Germany.
Peter.mulser@physik.tu-darmstadt.de

Prof. Dr. Rasheed Azzam

Department of Electrical Engineering, University of New Orleans
New Orleans, Louisiana 70148, U. S. A.
razzam@uno.edu

Prof. Dr. Shawqi Al-Dallal

Department of Physics, Faculty of Science, University of Bahrain,
Manamah, Kingdom of Bahrain.

Prof. Dr. Wolfgang Nolting

Institute of Physics / Chair: Solid State Theory, Humboldt-
University at Berlin, Newtonstr. 15 D-12489 Berlin, Germany
Wolfgang.nolting@physik.hu-berlin.de

Prof. Dr. Ingo Hofmann

GSI Darmstadt, Planckstr. 1, 64291, Darmstadt, Germany.
i.hofmann@gsi.de

Prof. Dr. Jozef Lipka

Department of Nuclear Physics and Technology, Slovak University
of Technology, Bratislava, Ilkovicova 3, 812 19 Bratislava,
Slovakia.
Lipka@elf.stuba.sk



The Hashemite Kingdom of Jordan



Yarmouk University

Jordan Journal of PHYSICS

An International Peer-Reviewed Research Journal
Funded by the Scientific Research Support Fund

Volume 13, No. 2, August 2020, Muharram 1442 H

Instructions to Authors

Instructions to authors concerning manuscript organization and format apply to hardcopy submission by mail, and also to electronic online submission via the Journal homepage website (<http://jjp.yu.edu.jo>).

Manuscript Submission

1- **E-mail to :** jjp@yu.edu.jo

2- **Online:** Follow the instructions at the journal homepage website.

Original *Research Articles*, *Communications* and *Technical Notes* are subject to critical review by minimum of two competent referees. Authors are encouraged to suggest names of competent reviewers. *Feature Articles* in active Physics research fields, in which the author's own contribution and its relationship to other work in the field constitute the main body of the article, appear as a result of an invitation from the Editorial Board, and will be so designated. The author of a *Feature Article* will be asked to provide a clear, concise and critical status report of the field as an introduction to the article. *Review Articles* on active and rapidly changing Physics research fields will also be published. Authors of *Review Articles* are encouraged to submit two-page proposals to the Editor-in-Chief for approval. Manuscripts submitted in *Arabic* should be accompanied by an Abstract and Keywords in English.

Organization of the Manuscript

Manuscripts should be typed double spaced on one side of A4 sheets (21.6 x 27.9 cm) with 3.71 cm margins, using Microsoft Word 2000 or a later version thereof. The author should adhere to the following order of presentation: Article Title, Author(s), Full Address and E-mail, Abstract, PACS and Keywords, Main Text, Acknowledgment. Only the first letters of words in the Title, Headings and Subheadings are capitalized. Headings should be in **bold** while subheadings in *italic* fonts.

Title Page: Includes the title of the article, authors' first names, middle initials and surnames and affiliations. The affiliation should comprise the department, institution (university or company), city, zip code and state and should be typed as a footnote to the author's name. The name and complete mailing address, telephone and fax numbers, and e-mail address of the author responsible for correspondence (designated with an asterisk) should also be included for official use. The title should be carefully, concisely and clearly constructed to highlight the emphasis and content of the manuscript, which is very important for information retrieval.

Abstract: A one paragraph abstract not exceeding 200 words is required, which should be arranged to highlight the purpose, methods used, results and major findings.

Keywords: A list of 4-6 keywords, which expresses the precise content of the manuscript for indexing purposes, should follow the abstract.

PACS: Authors should supply one or more relevant PACS-2006 classification codes, (available at <http://www.aip.org/pacs/pacs06/pacs06-toc.html>)

Introduction: Should present the purpose of the submitted work and its relationship to earlier work in the field, but it should not be an extensive review of the literature (e.g., should not exceed 1 ½ typed pages).

Experimental Methods: Should be sufficiently informative to allow competent reproduction of the experimental procedures presented; yet concise enough not to be repetitive of earlier published procedures.

Results: should present the results clearly and concisely.

Discussion: Should be concise and focus on the interpretation of the results.

Conclusion: Should be a brief account of the major findings of the study not exceeding one typed page.

Acknowledgments: Including those for grant and financial support if any, should be typed in one paragraph directly preceding the References.

References: References should be typed double spaced and numbered sequentially in the order in which they are cited in the text. References should be cited in the text by the appropriate Arabic numerals, enclosed in square brackets. Titles of journals are abbreviated according to list of scientific periodicals. The style and punctuation should conform to the following examples:

1. Journal Article:

- a) Heisenberg, W., Z. Phys. 49 (1928) 619.
- b) Bednorz, J. G. and Müller, K. A., Z. Phys. B64 (1986) 189
- c) Bardeen, J., Cooper, L.N. and Schrieffer, J. R., Phys. Rev. 106 (1957) 162.
- d) Asad, J. H., Hijjawi, R. S., Sakaji, A. and Khalifeh, J. M., Int. J. Theor. Phys. 44(4) (2005), 3977.

2. Books with Authors, but no Editors:

- a) Kittel, C., "Introduction to Solid State Physics", 8th Ed. (John Wiley and Sons, New York, 2005), chapter 16.
- b) Chikazumi, S., C. D. Graham, JR, "Physics of Ferromagnetism", 2nd Ed. (Oxford University Press, Oxford, 1997).

3. Books with Authors and Editors:

- a) Allen, P. B. "Dynamical Properties of Solids", Ed. (1), G. K. Horton and A. A. Maradudin (North-Holland, Amsterdam, 1980), p137.
- b) Chantrell, R. W. and O'Grady, K., "Magnetic Properties of Fine Particles" Eds. J. L. Dormann and D. Fiorani (North-Holland, Amsterdam, 1992), p103.

4. Technical Report:

Purcell, J. "The Superconducting Magnet System for the 12-Foot Bubble Chamber", report ANL/HEP6813, Argonne Natl. Lab., Argonne, III, (1968).

5. Patent:

Bigham, C. B., Schneider, H. R., US patent 3 925 676 (1975).

6. Thesis:

Mahmood, S. H., Ph.D. Thesis, Michigan State University, (1986), USA (Unpublished).

7. Conference or Symposium Proceedings:

Blandin, A. and Lederer, P. Proc. Intern. Conf. on Magnetism, Nottingham (1964), P.71.

8. Internet Source:

Should include authors' names (if any), title, internet website, URL, and date of access.

9. Prepublication online articles (already accepted for publication):

Should include authors' names (if any), title of digital database, database website, URL, and date of access.

For other types of referenced works, provide sufficient information to enable readers to access them.

Tables: Tables should be numbered with Arabic numerals and referred to by number in the Text (e.g., Table 1). Each table should be typed on a separate page with the legend above the table, while explanatory footnotes, which are indicated by superscript lowercase letters, should be typed below the table.

Illustrations: Figures, drawings, diagrams, charts and photographs are to be numbered in a consecutive series of Arabic numerals in the order in which they are cited in the text. Computer-generated illustrations and good-quality digital photographic prints are accepted. They should be black and white originals (not photocopies) provided on separate pages and identified with their corresponding numbers. Actual size graphics should be provided, which need no further manipulation, with lettering (Arial or Helvetica) not smaller than 8 points, lines no thinner than 0.5 point, and each of uniform density. All colors should be removed from graphics except for those graphics to be considered for publication in color. If graphics are to be submitted digitally, they should conform to the following minimum resolution requirements: 1200 dpi for black and white line art, 600 dpi for grayscale art, and 300 dpi for color art. All graphic files must be saved as TIFF images, and all illustrations must be submitted in the actual size at which they should appear in the journal. Note that good quality hardcopy original illustrations are required for both online and mail submissions of manuscripts.

Text Footnotes: The use of text footnotes is to be avoided. When their use is absolutely necessary, they should be typed at the bottom of the page to which they refer, and should be cited in the text by a superscript asterisk or multiples thereof. Place a line above the footnote, so that it is set off from the text.

Supplementary Material: Authors are encouraged to provide all supplementary materials that may facilitate the review process, including any detailed mathematical derivations that may not appear in whole in the manuscript.

Revised Manuscript and Computer Disks

Following the acceptance of a manuscript for publication and the incorporation of all required revisions, authors should submit an original and one more copy of the final disk containing the complete manuscript typed double spaced in Microsoft Word for Windows 2000 or a later version thereof. All graphic files must be saved as PDF, JPG, or TIFF images.

Allen, P.B., “.....”, in: Horton, G.K., and Muradudin, A. A., (eds.), “Dynamical.....”, (North.....), pp....

Reprints

Twenty (20) reprints free of charge are provided to the corresponding author. For orders of more reprints, a reprint order form and prices will be sent with the article proofs, which should be returned directly to the Editor for processing.

Copyright




Submission is an admission by the authors that the manuscript has neither been previously published nor is being considered for publication elsewhere. A statement transferring copyright from the authors to Yarmouk University is required before the manuscript can be accepted for publication. The necessary form for such transfer is supplied by the Editor-in-Chief. Reproduction of any part of the contents of a published work is forbidden without a written permission by the Editor-in-Chief.

Disclaimer

Opinions expressed in this Journal are those of the authors and neither necessarily reflects the opinions of the Editorial Board or the University, nor the policy of the Higher Scientific Research Committee or the Ministry of Higher Education and Scientific Research. The publisher shoulders no responsibility or liability whatsoever for the use or misuse of the information published by JJP.

Indexing

JJP is currently indexing in:

	Emerging Sources Citation Index (ESCI)	 ULRICHSWEB™ GLOBAL SERIALS DIRECTORY
		

Jordan Journal of
P H Y S I C S

An International Peer-Reviewed Research Journal

Volume 13, No. 2, August 2020, Muharram 1442 H

Editorial Preface

This special issue of Jordan Journal of Physics (JJP) presents 18 selected papers presented at the Fourth International Symposium on Dielectric Materials and Applications (ISyDMA 4) that was held Under the Patronage of His Royal Highness Prince Hamzah Bin Al Hussein between 2-4/5/2019 at the IT Auditorium of the University of Jordan. These papers were subjected to standard refereeing of JJP.



Jordan Journal of
P H Y S I C S

An International Peer-Reviewed Research Journal

Volume 13, No. 2, August 2020, Muharram 1442 H

Fourth International Symposium on Dielectric Materials and
Applications (ISyDMA 4)

2nd to 4th May 2019

University of Jordan, Amman, Jordan

Guest Editor Preface

Welcome to this Special Issue containing articles selected from the Fourth Int. Symposium on Dielectric Materials and Applications (ISyDMA 4) organized by the Univ. of Jordan (JU), Amman, Jordan and the Jordan University of Science and Technology (JUST), Irbid, Jordan in cooperation with The Jordanian Club of Humboldt Fellows (JCHF), Al-Ahliyya Amman University (AAU), Moroccan Association of Advanced Materials and Moroccan Society of Applied Physics. After three prestigious editions, ISyDMA 1 (Rabat-Kenitra, Morocco, 4-6/5/2016), ISyDMA 2 (Bucharest, Romania, 11-14/7/2017) and ISyDMA 3 (Beni Mellal, Morocco, 18-20/4/2018), a 4th edition of ISyDMA was held in Amman; Under the Patronage of His Royal Highness Prince Hamzah Bin Al Hussein between 2-4/5/2019 at the IT Auditorium of UJ. This event provided an Int. forum for reporting recent developments in advanced dielectric materials and applications with technical, keynote and tutorial sessions covering hot topics in dielectric materials advances.

A Pre-Conf. School was organized by JUST jointly with the ISyDMA 4 at Al Karama Auditorium, JUST, from 30/4 to 1/5/2019, under the chairmanship of Prof. Dr. AL Omari Mohammed-Ali and full support from Dean of Science and Arts Faculty Prof. Dr. Qutaibah T. Khatatbeh. The scope of this School was to familiarize graduate students and junior researchers with the state of art in advanced materials for various applications.

The goal of the ISyDMA 4 Symposium was to provide a platform for researchers, scientists from all over the world to exchange ideas, hold a wide range of discussions on recent developments in dielectric materials and their innovative applications. It addressed materials scientists, physicists, chemists, biologists, and electrical engineers engaged in fundamental and applied research or technical investigations on such materials. It provided an Int. forum to discuss current research on electrical insulation, dielectric phenomena and related topics. The scope of the ISyDMA'4 includes, but is not limited to:

- Dielectric properties, polarization phenomena and applications, physics of space charge in non-conductive materials, polymers, composites, ceramics, glasses, biodielectrics, nanodielectrics, metamaterials, piezoelectric, pyroelectric and ferroelectric materials.

- Impedance spectroscopy applications to electrochemical and dielectric phenomena.
- Dielectrics for superconducting applications, industrial and biomedical applications, dielectric materials for electronics & photonics, diagnostic applications for dielectrics, dielectrics for electrical systems, electrical conduction and breakdown in dielectrics, surface and interfacial phenomena.
- Electrical insulation in high voltage power equipment and cables, ageing, discharges HV insulation, space charge and its effects in dielectrics, gaseous electrical breakdown and discharges.
- High voltage (HV) insulation design using computer based analysis. Partial discharges in insulation: detection methods and impact on ageing, monitoring and diagnostic methods for electrical insulation degradation, measurement techniques, modeling and theory.
- Solar energy Materials.

The accepted papers, offer a good look into the subjects covered by the meeting and are a bit of the 30 oral and 40 poster presentations made in the ISyDMA 4 under chairmanship of Prof. Dr. AL-HUSSEIN Mahmoud (UJ), Prof. Dr. MOUSA Marwan S. (Mu'tah Univ., Al-Karak, Jordan), Prof. Dr. Al OMARI Mohammed-Ali (JUST), Prof. Dr. AL-SOUD Yaseen (Al al-Bayt Univ., Al-Mafraq, Jordan), Dr. SHATNAWI Moneeb (UJ), Dr. JABER Ahmad A. (AAU), Prof. Dr. ACHOUR Mohammed Essaid (Univ. Ibn Tofail, Kenitra, Morocco), Prof. Dr. OUERAGLI Amane (Cadi Ayyad Univ., Marrakech, Morocco) and Prof. Dr. MABROUKI Mustapha (Sultan Moulay Slimane Univ., Beni-Mellal, Morocco) with help of scientific and organizing Committees.

The Symposium could summarize the reasons for which the Jordan Journal of Physics (JJP) devoted the issue number 02 of volume 13 to various Investigations on dielectric materials. An important reason for the success of the Symposium was the participation of Prof. Dr. COSTA Luis Cadillon (Portugal), Prof. Dr. GRACA Manuel Pedro Fernandes (Portugal), Prof. Dr. MABROUKI Mustapha (Morocco), Prof. Dr. OMARI Ahmad (Jordan), Prof. Dr. PETKOV Plamen (Bulgaria), Prof. Dr. PETKOVA Tamara, (Bulgaria), Prof. Dr. PETRA Uhlmann (Germany), Prof. Dr. POPOV Cyril (Germany) and Prof. Dr. Mahmood Sami H. (Jordan) as plenary conference speakers but the 100 participants created a good and rich scientific atmosphere.

Offering to the Int. Community some results from the conference, acknowledging JJP Editor in Chief Prof. Dr. ABU AL-JARAYESH Ibrahim from Yarmouk Univ., Irbid, Jordan, his Editorial Board and staff for the good job made to extend the Symposium to readers of this journal.

Guest Editors

Prof. Dr. ACHOUR Mohammed Essaid

Prof. Dr. MOUSA Marwan Suleiman

Prof. Dr. AL OMARI Mohammed-Ali

Dr. JABER Ahmad Asaad (Al Ahliyya Amman University)

Jordan Journal of

PHYSICS

An International Peer-Reviewed Research Journal

Volume 13, No. 2, August 2020, Muharram 1442 H

Fourth International Symposium on Dielectric Materials and Applications (ISyDMA 4)

2th to 4th May 2019

University of Jordan, Amman, Jordan

Prof. Dr. AL-HUSSEIN Mahmoud

Conf. Chairman

University of Jordan, Amman, Jordan

Prof. Dr. MOUSA Marwan Suleiman

Conf. Co-Chairman

Mu'tah University, Al-Karak, Al-karak, Jordan

Prof. Dr. AL OMARI Mohammed-Ali

Pre-Conf. School Chairman

Jordan University of Science and Technology, Irbid, Jordan

Prof. Dr. AL-SOUD Yaseen

Conf. Co-Chairman

Al al-Bayt University, Al-Mafraq, Jordan

Dr. SHATNAWI Moneeb

Conf. Co-Chairman

University of Jordan, Amman, Jordan

Prof. Dr. ACHOUR Mohammed Essaid

Conf. Chairman

University Ibn Tofail, Kenitra, Morocco

Prof. Dr. OUERIAGLI Amane

Conf. Co-Chairman

Cadi Ayyad Univeristy, Marrakech, Morocco

Prof. Dr. MABROUKI Mustapha

Conf. Co-Chairman

Sultan Moulay Slimane University, Beni-Mellal, Morocco

Organizing Committee

Prof. Dr. Mahmoud Al-Hussein
Department of Physics, The University of Jordan, Amman

Prof. Dr. Marwan Mousa
Department of Physics, Mu'tah University, Al-Karak

Prof. Dr. Bashar Lahlouh
Department of Physics, The University of Jordan, Amman

Prof. Dr. Moneeb Shatnawi
Department of Physics, The University of Jordan, Amman

Prof. Dr. Yaseen Alsoud
Dept. of Chemistry Faculty of Science Al al-Bayt University, Al-Mafraq

Prof. Dr. Mohammad El-Khateeb
Department of Applied Chemical Sciences Jordan University of Science and Technology Irbid

Prof. Dr. Mohammed-Ali Al-Omari
Department of Applied Physical Sciences Jordan University of Science and Technology

Prof. Dr. Mousa Jafar
Department of Physics, The University of Jordan, Amman

Prof. Dr. Sami Mahmood
Department of Physics, The University of Jordan, Amman

Prof. Dr. Ibrahim Abu-Aljarayesh
Department of Physics, Yarmouk University, Irbid

Prof. Dr. Qutaibah Khatatbeh
Department of Mathematics and Statistics Jordan University of Science and Technology Irbid

Prof. Dr. Ikhlas Tarawneh
Al-Hussein Bin Talal University

Dr. Ahmad Asaad Jaber
Al-Ahliyya Amman University, Amman

Dr. Inshad Yousef
German-Jordanian University, Amman

Dr. Amer Dakheel Al-Oqali
Physics Department, Mutah University

Dr. Ali Taani
Applied Science Department, Aqaba University College, Al-Balqa' Applied University

Dr. Riad Salem Ababneh
Department of Physics, Yarmouk University Irbid

Dr. Muna Abu-Dalo
Department of Applied Chemical Sciences Jordan University of Science and Technology Irbid

Dr. Nusaiba Al-Nemrawi
Department of Pharmaceutical Technology Jordan University of Science and Technology Irbid

Dr. Wala Al-Tamimi
Department of Physics, The University of Jordan, Amman

Dr. Joseph Bawalsah
Al-Ahliyya Amman University, Amman

Jordan Journal of P H Y S I C S

An International Peer-Reviewed Research Journal

Volume 13, No. 2, August 2020, Muharram 1442 H

Table of Contents:

Articles	Pages
Automated System for Optical Inspection of Defects in Resist-coated Non-patterned Wafer	93-100
A. Knápek, M. Drozd, M. Matějka, J. Chlumská, S. Král and V. Kolařík	
Applying the Field Emission Orthodoxy Test to Murphy-Good Plots	101-111
M. M. Allaham, R. G. Forbes and M. S. Mousa	
Impedance Spectroscopy and Dielectric Properties of Carbon Nanotube-Reinforced Epoxy Polymer Composites	113-121
Z. Samir, S. Boukheir, R. Belhimria, M. E. Achour, N. Éber, L. C. Costa and A. Oueriagli	
Theoretical Simulation of Backscattering Electron Coefficient for SixGe_{1-x}/Si Heterostructure as a Function of Primary Electron Beam Energy and Ge Concentration	137-147
A.M.D. Assa'd and H. Kawariq	
From Amorphous Red Phosphorus to a Few Layers of Black Phosphorus: A Low-cost and Efficient Preparation Process	149-155
G. Tiouitchi, F. ElManjli, O. Mounkachi, A. Mahmoud, F. Boschini, A. Kara, H. Oughaddou, M. Hamedoun, A. Benyoussef and M. Ait Ali	
Structural, Electrical and Thermal Properties of Composites Based on Conducting Polymer	157-163
N. Aribou, S. Barnoss, M. El Hasnaoui, M. E. Achour and L. C. Costa	
Structural and Dielectric Properties of Zn_{1-x}MoxO Nanoparticles	165-170
H. Basma, F. Al-Mokdad and R. Awad	
Similarities and Differences between Two Researches in Field Electron Emission: A Way to Develop a More Powerful Electron Source	171-179
M. S. Mousa, A. Knápek and L. Grmela	
Review Article	Pages
Structure, Synthesis and Applications of ZnO Nanoparticle: A Review	123-135
H. H. Azeez, A. A. Barzinjy and S. M. Hamad	

Automated System for Optical Inspection of Defects in Resist-coated Non-patterned Wafer

A. Knápek, M. Drozd, M. Matějka, J. Chlumská, S. Král and V. Kolařík

*Institute of Scientific Instruments of the Czech Academy of Science, Královopolská 147,
612 64 Brno, Czech Republic.*

Doi : <https://doi.org/10.47011/13.2.1>

Received on: 08/08/2019;

Accepted on: 9/2/2020

Abstract: Quality control of the resist coating on a silicon wafer is one of the major tasks prior to the exposition of patterns into the resist layer. Thus, the ability to inspect and identify the physical defect in the resist layer plays an important role. The absence of any unwanted defect in resist is an ultimate requirement for preparation of precise and functional micro- or nano-patterned surfaces. Currently used wafer inspection systems are mostly utilized in semiconductor or microelectronic industry to inspect non-patterned or patterned wafers (integrated circuits, photomasks, ... etc.) in order to achieve high yield production. Typically, they are based on acoustic micro-imaging, optical imaging or electron microscopy. This paper presents the design of a custom optical-based inspection device for small batch lithography production that allows scanning a wafer surface with an optical camera and by analyzing the captured images to determine the coordinates (X, Y), the size and the type of the defects in the resist layer. In addition, software responsible for driving the scanning device and for advanced image processing is presented.

Keywords: Optical inspection, Resist layer, Non-patterned wafer, Quality control.

Introduction

Silicon wafer is a typical substrate that is used in lithography process for microfabrication of various types of devices. The quality of the silicon wafer determines the quality of a lithographic process, just as the quality of the resist-coated surface prior to the lithography step is very important in terms of the final functionality of the fabricated micro-device. Several papers have been published reporting optical properties of polymethyl methacrylate (PMMA) films [1, 2, 3].

Generally, there are two categories of wafer inspection methods: non-patterned and patterned [4, 5]. Non-patterned wafer inspection typically investigates defects on the unprocessed silicon wafer. On the other hand, patterned wafer

inspection is used for wafer control after the lithography process.

Industrial inspection devices used in semiconductor and chip manufacturing are based on two main technologies: optical and electron-beam [6, 7]. The optical inspection device typically uses laser, deep ultraviolet (DUV) or a broadband plasma light source to illuminate the wafer and acquire an optical image in the bright field or the dark field. In general, a principle of function, where a reflected laser beam carries information about a position, is illustrated in Fig. 1. The e-beam based inspection uses highly specified and automatized scanning electron microscopes that are typically used only for detailed inspection of patterned wafers [6].

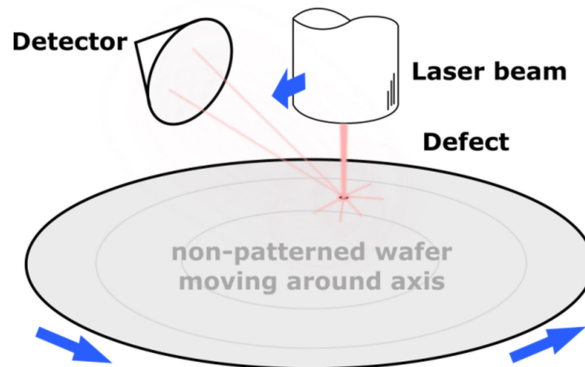


FIG. 1. Optically-based principle of defect inspection on a non-patterned wafer.

The devised approach is based on a motivation to develop an optical-based semi-automatic wafer inspection device that allows the inspection of a non-patterned [6] resist-coated wafer and would replace the current visual inspection of a wafer within the visible light microscope (VLM). Our primary aim is to find the position, the size and the type of the random defect at the layer of electron resist. That sort of evaluation is applied to a wafer surface by spin coating technique prior to its patterning by electron beam lithography (EBL).

Various types of defects are involved during the deposition of resist by spin-coating: dust contamination, micro-bubbles, bumps, craters,

comets, thickness inhomogeneity ... etc. [9, 10]. For the software, it is important to be able to identify not just the position of defects on the wafer, but also to estimate the type of defect, that may be considered as an essential feature, because not every type of defect can be equally problematic in the follow-up lithography process [9]. For example, a larger dust particle in or on the resist might cause a charging phenomenon, when the electron beam irradiates neighboring particles. Therefore, a charged dust particle can deflect the electron beam and reduce the dose received under and in the vicinity of the particle [11], as illustrated in Fig. 2.

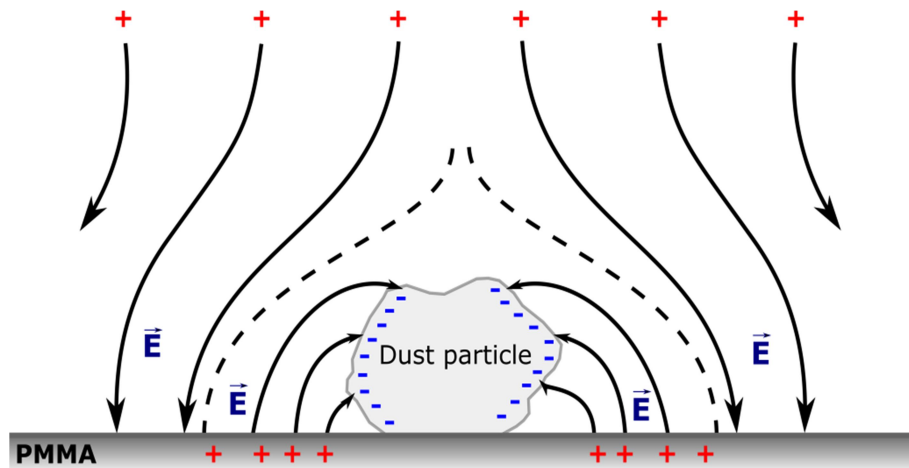


FIG. 2. Schematic of charging of a dust particle and the resulting defect in the EBL patterned wafer, with permission from Hitachi, Ltd., Tokyo, Japan [8].

It is critical to avoid patterning in the areas with particle contamination. Air bubbles might create holes in the resist after development. Comets can cause resist thickness inhomogeneity and thus an inadequate development of the recorded pattern.

Defect Analysis

The preparation of PMMA resist layers on silicon wafers by spin-coating method is performed under laminar flow in order to lower the chance of a defect occurring in the prepared layer. The PMMA and xylene solvent are mixed together and, according to viscosity, are filtered through syringe filters (the porosity level is 0.45

μm or $5\ \mu\text{m}$). Subsequently, the resist is poured onto the silicon wafer which in this case forms an approx. $2.5\ \mu\text{m}$ thick compact layer.

A variety of problems may occur during the coating process. In general, the above defects can be caused by impurities on the silicon wafer, such as dust particles, impurities or micro-bubbles in the resist mixture or by e.g. poor centering of the wafer on a spin coater. The parameters considered within the process of spin coating include rotation speed, acceleration, time and the application method of the liquid resist precursor.

The first class of defects is caused by impurities that stick to the resist layer during the deposition or during the baking process, as illustrated in Fig. 3. If a dust particle or fiber falls on the wafer during deposition, it becomes coated in the resist and forms a “comet” (a small thickness difference formed from the center of the particle to the edge of the wafer). Other possible particles are small resist flakes (i.e., dried resist) that stick to the layer and become permanently attached to the surface due to the baking process.

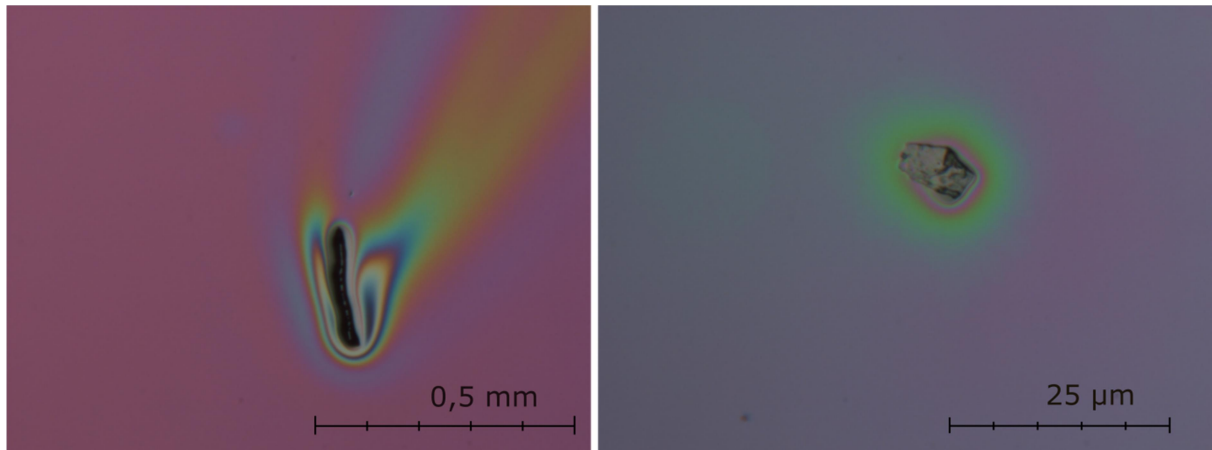


FIG. 3. Fiber creating a comet (left); a resist flake baked into the layer (right).

The second class of defects illustrated in Fig. 4 may occur randomly based on the processing technology. During the process of mixing of the resist and the solvent, air bubbles can form in the mixture. If a bubble is transferred on the wafer, it may form a defect called “micro-bubble”. It is a small spot (spherical shape) in the resist layer, where there is a huge thickness difference. It may cause problems during development (for example cracks in the resist layer around the spot). It can be prevented by degassing the mixture in the desiccator or really slow pouring of the resist mixture on the wafer. Another issue that may occur is related to inhomogeneity on a much bigger scale. For example, interference circles can be seen all over the wafer. The thickness difference is formed on a bigger

surface than in the case of micro-bubble defect. The exposed structure has afterwards different depths according to the location on the wafer. This type of defect can be caused by poor centering of the wafer on a spin coater, by an insufficiently levelled spin coater or by improper choice of the spin-coating parameters, as mentioned above. This type of defect cannot be seen using a microscope because of the small field of view. It can, however, be seen by the naked eye. Despite this kind of defect cannot be observed by the set-up, it has to be dealt with before the process of electron beam lithography and defected areas have to be avoided. This particular type of defect is further explained in the following paragraphs.

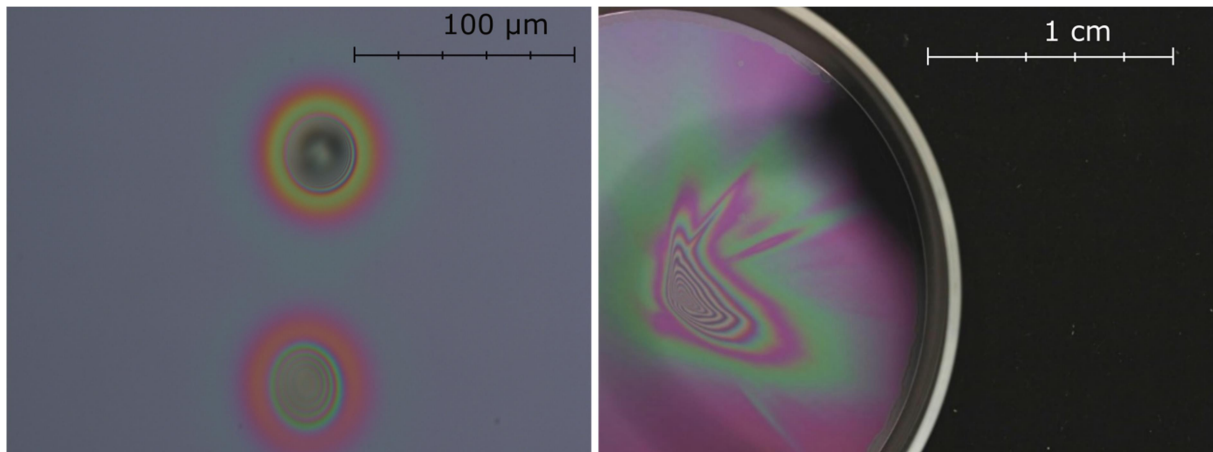


FIG. 4. Micro bubble (left), inhomogeneity all over the wafer (right). The left image was taken by VLM and the right one by a camera.

The interference effects, which can be seen in Figs. 3 and 4, are determined by the optical path length (OPL) through the thin PMMA film in a phenomenon called thin-film interference. Optical path length is the product of the geometric length d of the path of light through a system and the index of refraction n of the medium through which the light propagates, hence $OPL = nd$. Through this concept, a phase of the light can be determined by governing interference and diffraction of light as it propagates.

Recently, as was reported by Lalova [2], refractive index n , extinction coefficient k and thickness d of the spin-coated PMMA films deposited on a silicon wafer were determined by using minimization of a function. The function consists of the discrepancies between measured and calculated R spectra by means of multi-wavelength nonlinear curve fitting. The

refractive index was described using Sellmeier's equation in the following form:

$$n^2(\lambda) = 1 + \frac{A_1 \lambda^2}{\lambda^2 - A_2^2}, \quad (1)$$

where A_1 and A_2 are the Sellmeier's coefficients. The dispersion of the extinction coefficient was described using the following exponential dependence [2]:

$$k = B_1 \exp\left(\frac{B_2}{\lambda}\right), \quad (2)$$

where B_1 and B_2 are dispersion coefficients. Based on Eqs. (1) and (2), it has been found out that the refractive index of the thin PMMA increases with the increase of the thickness following an exponential law of the type $n = n_0 + A_1 (1 - \exp(-d/d_1))$, where n_0 is the initial value of the refractive index and $A_1 = -0.9$ and $d_1 = 31.91$ are parameters.

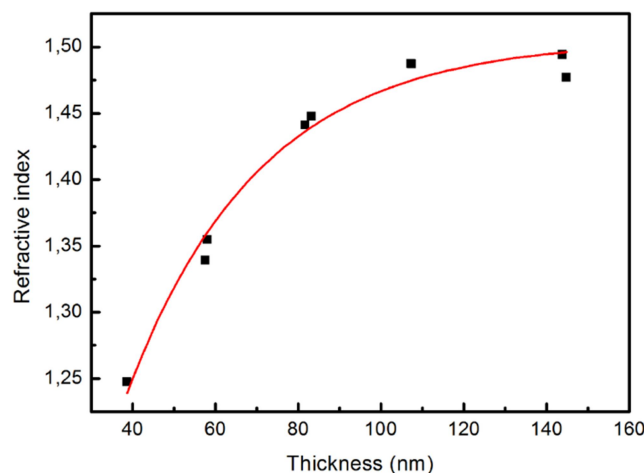


FIG. 5. Dependence of the refractive index on the thickness of thin spin-coated PMMA films at a wavelength of 600 nm, with permission from *Bulgarian Chemical Communications* [2].

Based on the dependence illustrated in Fig. 5, it has been concluded that the refractive index is thickness-dependent for values of $d < 110$ nm. For thin films with thicknesses greater than 110 nm, the coating possess refractive index is close to that of the bulk [2].

Measurement Set-Up

The measurement set-up illustrated in Fig. 6 consists of a table moving along the axis Y and a camera placed above the table which moves

along the axis X. The camera is based on a classical color CMOS sensor working at a resolution of 1.3 megapixels, allowing obtaining 15 screens per second with a resolution of 1280×1024 pixels over the USB 2.0 bus. The camera provides also a white LED lighting, whose intensity can be controlled manually. In order to reduce a distortion caused by the lens that may appear near the edges of the image, only the inner part of the image (approx. 70% of the original image) is used and further processed.

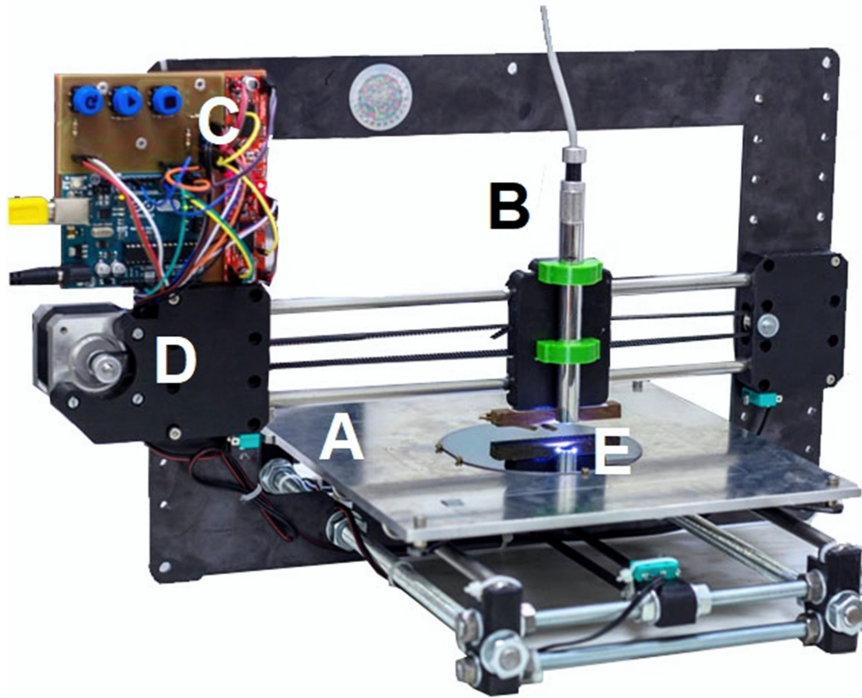


FIG. 6. Prototype of the measurement set-up scanning over a 4-inch wafer showing all the electronic and mechanical parts: (A) moving table, (B) camera on a moving holder, (C) Arduino board with buttons and stepper motor drivers, (D) stepper motor drive and (E) the evaluated 4-inch wafer.

The mechanical system was originally adapted from a 3D-printer-based platform with two precise stepper motors (see Figs. 6 and 7). The XY movement is based on the two stepper motors controlled through a microcontroller board Arduino UNO® based on the Microchip ATmega328P. The Arduino board contains its own program responsible for interpreting received commands from the WaferScan software (illustrated in Fig. 8, left), which includes driving of the movements. The board also generates a response when limit switches have reached the end of the track in one of the axes. The power supply to the motors is provided through two Easy Driver expansion boards. The whole system is powered using an external 12V DC power supply.

The main algorithm consists of a few simple steps that are implemented within an algorithm, whose flowchart is illustrated in Fig. 8 (right). In the beginning, the position of a calibration mark is located. The calibration mark is situated on a calibration sample, which is a silicon chip (1 cm^2) with a cross-structure etched into the surface. This sample is placed on the stage table that contains also the evaluated wafer. After the position of the mark is read, a new coordinate system is set. This system of coordinates is then used for determining positions of any defect found during the scanning over the surface of the evaluated wafer. The flowchart illustrated in Fig. 8 (right) of the main scanning algorithm is implemented using Matlab graphic user interface (GUIDE®) and Matlab Instrumentation

toolbox®. Matlab instrumentation toolbox provides software means to communicate with all the components directly from the software by using text-based Standard Commands for Programmable Instruments (SCPI) command or *via* instrument drivers. The process follows a simple line scanning procedure, as it is known from any other scanning devices, which means that when an image is obtained, the camera

moves to another field of view until the whole surface is mapped. The implementation of post-processing uses advanced image processing and recognition techniques, whose description is outside of the scope of this paper; so, let us just simply conclude that the software returns precise coordinates and sizes of the defects found in the taken images.

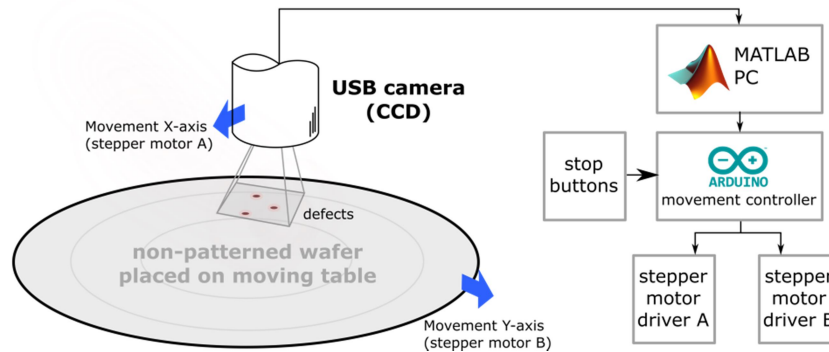


FIG. 7. Schematic illustration of the measurement set-up.

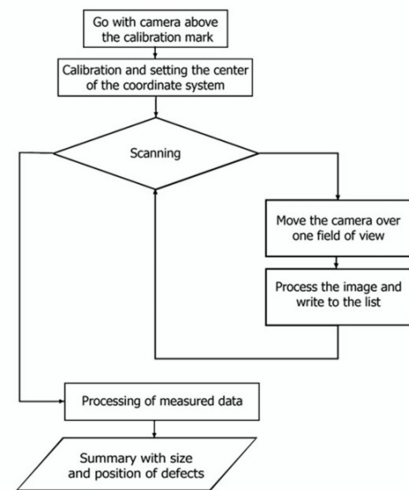
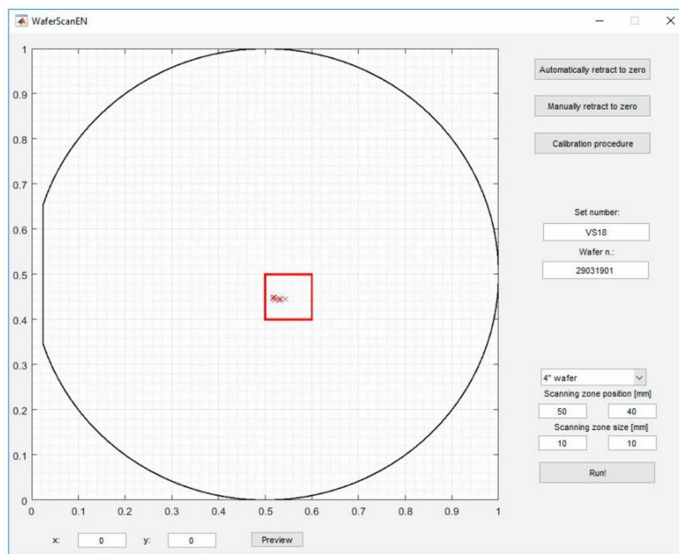


FIG. 8. The screen of the WaferScan software showing located defects in the red box (left); the flowchart of scanning algorithm schematically showing the implemented scanning procedure (right).

The WaferScan software (Fig. 8 left) allows running the initial calibration procedure both manually and automatically as well as precisely determining the area on the wafer to be scanned. On the background, the software saves a list of defects and their parameters as well as the particular images that are continually obtained for a possible further inspection. Using the saved images, it is possible to determine the size of the located defects.

Results and Discussion

A comparison of two particular defects found is illustrated in Fig. 9, showing the output of our WaferScan system compared to the images obtained by manual inspection using a classical visible-light microscope. The map of defects shows the precise positions of the particular defects found.

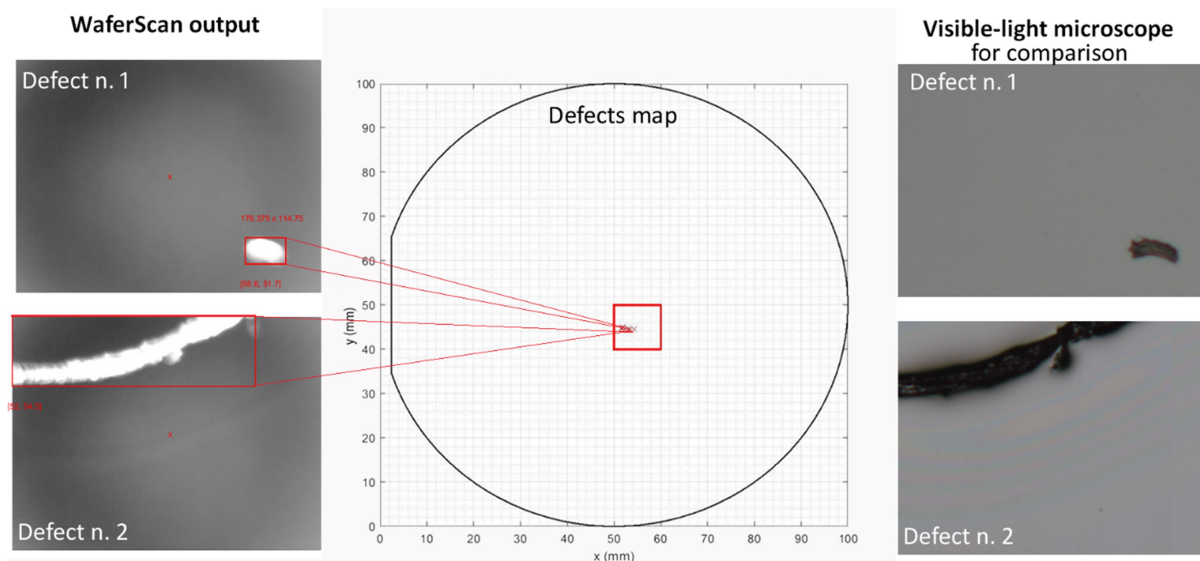


FIG. 9. Results provided for two selected defects (left top and above) within the scanning area (that is located within the red borders). On the right side, there are images from a visible-light microscope.

Summary and Conclusions

This paper presents an important tool that has been developed to cover certain needs of complex research, which are connected with the development of large-sized micro-structure diffractive optical elements as well as sub-micron diffractive holography structures for industrial holography applications.

The devised set-up enables to scan a non-patterned wafer stepwise and to find defects as small as 10 μm by means of a precise CCD camera that scans the surface. Software, that is an essential part of the device, allows determining the size of a defect and its position on the wafer. This is the most significant benefit of this set-up, since the evaluation of a small series was in most cases done manually. Moreover, the accuracy of the process was increased and its error rate was decreased.

Further development will focus on precise characterization of particular defect types and automated distinction between defects, such as micro-bubbles, fiber or dust, in addition to revealing inhomogeneities of the resist layer on a smaller scale. The set-up will be further extended by addition of an automated focusing system that would make the process more precise. Among the other future goals, the set-up may be also extended to be used for patterned wafers and to implement White Light Reflectance Spectroscopy (WLRs).

Acknowledgements

The research was supported by the Ministry of Industry and Trade of the Czech Republic, MPO-TRIO project FV10618. The research infrastructure was funded by the Czech Academy of Sciences (project RVO: 68081731).

References

- [1] Norrman, K., Ghanbari-Siahkali, A. and Larsen, N.B., Annual Reports Section "C" (Physical Chemistry), 101 (2005) 174.
- [2] Lalova, A. and Todorov, R., Bulgarian Chemical Communications, 47 (2015) 29.
- [3] Hussein, A.S., Shinen, M.H. and Abdali, M.S., Journal of University of Babylon for Pure and Applied Sciences, 27 (4) (2019) 169.
- [4] Franssila, S., "Introduction to Micro-fabrication", (John Wiley & Sons, Ltd., 2006), pp.1-15 s. ISBN 0-470-85105-8.
- [5] Lapedus, M. "Inspecting Unpatterned Wafers", Semiconductor engineering, [online], 16 August 2018, Available at: <https://semiengineering.com/inspecting-unpatterned-wafers/>
- [6] Oberai, A. and Yuan, J.-S., Electronics, 6 (2017) 87.

- [7] Lapedus, M., "E-Beam vs. Optical Inspection", Semiconductor engineering [online], 16 July 2016, Available at: <https://semiengineering.com/e-beam-vs-optical-inspection/>
- [8] Yoda, H. et al., IEEE Transactions on Pattern Analysis and Machine Intelligence, 10 (1) (1988) 4.
- [9] Peerson, I., Thompson, G., DiBiase, T., Ashkenaz, S. and Pinto, R.H., Yield Management Solutions, 2 (3) (2000) 17.
- [10] Koch, Ch., Rinke, T.J., "Photolithography: Basic of Microstructuring", 1st Ed., (MicroChemicals, GmbH, 2017), pp.58-62 s. ISBN 978-3-9818782-1-9.

Jordan Journal of Physics

ARTICLE

Applying the Field Emission Orthodoxy Test to Murphy-Good Plots

M. M. Allaham^a, R. G. Forbes^b and M. S. Mousa^a

^aSurface Physics and Materials Technology Lab., Department of Physics, Mutah University, Al-Karak 61710, Jordan.

^bAdvanced Technology Institute & Department of Electrical and Electronic Eng., Faculty of Eng. & Physical Sciences, University of Surrey, Guildford, Surrey GU2 7XH, UK.

Doi : <https://doi.org/10.47011/13.2.2>

Received on: 10/10/2019;

Accepted on: 16/1/2020

Abstract: In field electron emission (FE) studies, it is important to check and analyze the quality and validity of results experimentally obtained from samples, using suitably plotted current-voltage [$I_m(V_m)$] measurements. For the traditional plotting method, the Fowler-Nordheim (FN) plot, there exists a so-called "orthodoxy test" that can be applied to the FN plot, in order to check whether or not the FE device/system generating the results is "ideal". If it is not ideal, then emitter characterization parameters deduced from the FN plot are likely to be spurious. A new form of FE $I_m(V_m)$ data plot, the so-called "Murphy-Good (MG) plot", has recently been introduced (R.G. Forbes, Roy. Soc. Open Sci. 6 (2019) 190912). This aims to improve the precision with which characterization-parameter values (particularly values of formal emission area) can be extracted from FE $I_m(V_m)$ data. The present paper compares this new plotting form with the older FN and Millikan-Lauritsen (ML) forms and makes an independent assessment of the consistency with which slope (and hence scaled-field) estimates can be extracted from an MG plot. It is shown that, by using a revised formula for the extraction of scaled-field values, the existing orthodoxy test can be applied to Murphy-Good plots. The development is reported of a prototype web tool that can apply the orthodoxy test to all three forms of FE data plot (ML, MG and FN).

Keywords: Field emission, Field electron emission, Murphy-Good plot, Fowler-Nordheim plot, Millikan-Lauritsen plot, Orthodoxy test.

Introduction

The process of field electron emission (FE) occurs in many technological contexts. This paper is about the analysis of measured current-voltage [$I_m(V_m)$] data that relate to FE processes, devices and systems. The conventional methods of analyzing this data are to make either (a) a Fowler-Nordheim (FN) plot, i.e., a plot of the form $\log_{e,10}\{I_m/V_m^2\}$ vs $1/V_m$, or (b) (in older work) a Millikan-Lauritsen plot, i.e., a plot of the form $\log_{e,10}\{I_m\}$ vs $1/V_m$. Such plots are often approximately straight. Emitter characterization parameters are then extracted from the slope of

the plot and from the intercept that a fitted straight line makes with the $1/V_m = 0$ axis.

With logarithmic expressions, such as $\log\{x\}$ or $\ln\{x\}$, an international convention [1] is used in this paper that the symbol $\{x\}$ means "the numerical value of x , when x is measured in the stated units". In this paper, in all equations, all figures and all tables, voltages are *always* measured in volts and currents are *always* measured in amperes. Brackets not part of logarithmic expressions are used normally.

A so-called *ideal* FE device/system is one where the measured $I_m(V_m)$ characteristics are determined only by unchanging system geometry and surface properties and by the electron emission process. An ideal system is termed *orthodox* if, in addition, it is an adequate approximation to assume that emission takes place through a Schottky-Nordeim (SN) ("planar image rounded") potential-energy barrier and hence that Murphy-Good FE theory applies.

For an orthodox device/system, FN plot (or ML plot) analysis leads to correct values for emitter characterization parameters. However, for a variety of reasons (for example, series resistance in the measurement circuit), many real FE devices/systems are not ideal (and hence cannot be orthodox). When conventional FN plot (or ML plot) analysis techniques are applied to $I_m(V_m)$ data taken from non-ideal devices/systems, spurious values can be (and often are) derived for emitter characterization parameters.

The so-called *Orthodoxy Test* [2] is a test that can be applied to a FN plot (or to an ML plot), in order to establish whether or not the plotted data are derived from an orthodox FE device/system (and hence whether extracted characterization parameters are valid or spurious).

For a field emitter with local work function ϕ , subject to a local electrostatic field of magnitude F_L , a corresponding *scaled field* f_L can be defined by:

$$f_L \equiv c_S^2 \phi^{-2} F_L \equiv (e^3/4\pi\epsilon_0) \phi^{-2} F_L \equiv F_L/F_R, \quad (1)$$

where c_S is the Schottky constant, e is the elementary positive charge, ϵ_0 is the vacuum electric permittivity and $F_R [\equiv c_S^{-2} \phi^2]$ is the reference field needed to pull the top of an SN barrier of zero-field height ϕ down to the Fermi level. Emitter behaviour can be described in terms of characteristic field (F_C) and scaled-field (f_C) values, usually taken as the values at the emitter apex (for a pointed emitter) or at the apex of a prominent individual emitter (for large-area field electron emitters).

The range of f_C -values in which emitters normally operate is well established (see spreadsheet associated with [2]). When $I_m(V_m)$ data is plotted in the form of a Fowler-Nordheim (FN) plot or a Millikan-Lauritsen (ML) plot, the plot can be used to extract values of f_C that correspond to the range of electrostatic fields *apparently* used in the experiments. The

orthodoxy test compares these apparent f_C -values with the known f_C -values at which emitters normally operate and draws appropriate conclusions. For example, if an extracted f_C -value is higher than the known f_C -value at which an emitter melts or self-destructs, it is concluded that the FE device/system is not ideal and that any characterization results derived from the FN (or ML) plot are likely to be spurious.

Fowler-Nordheim plots came into use because the FE equation derived by FN in 1928 [3] predicted that an FN plot would be linear. But, in 1953, Burgess, Kroemer and Houston (BKH) [4] found a physical mistake in FN's thinking and a mathematical mistake in a related paper by Nordheim [5]. In 1956, Murphy and Good (MG) used the BKH results to develop a revised FE equation [6]. (For a modern derivation, using the International System of Quantities (ISQ), see [7]).

Murphy-Good plots are a new form of FE $I_m(V_m)$ data plot that has recently been developed [8]. They are based on improved mathematical understanding of MG theory, developed from 2006 onwards and have the form $\log_{e,10}\{I_m/V_m^k\}$ vs $1/V_m$, where the voltage exponent κ for the SN barrier used in MG theory has the value:

$$\kappa = 2 - \eta/6. \quad (2)$$

The parameter η depends only on the assumed work-function ϕ and is given by [2, 9]:

$$\eta \cong 9.836239 (\text{eV}/\phi)^{1/2}. \quad (3)$$

More generally, in the expression $\ln\{I_m/V_m^k\}$, the value to be allocated to the general voltage exponent κ depends on the plot type, as shown in Table 1.

TABLE 1. Values of the voltage exponent κ for the three plot types under discussion.

Plot type	Voltage exponent (κ)
Murphy-Good (MG)	$\kappa = (2-\eta/6)$
Fowler-Nordheim (FN)	2
Millikan-Lauritsen (ML)	0

In the work reported in this paper, we will confirm that using an MG plot is an improved method to analyse FE data. This is because modern Murphy-Good theory predicts that (unlike an ML plot or an FN plot) an MG plot will be "almost exactly" a straight line. This means that, for ideal measured current-voltage

data, we can extract well-defined emitter characterisation parameters more precisely and more easily than with the older plot forms.

We also develop a form of orthodoxy test that applies to Murphy-Good plots and report on the development of a software tool that implements this test for any of the three plot forms shown in Table 1.

Theoretical Background

The so-called *Extended Murphy Good (EMG) equation* [8] for the local emission current density (LECD) J_L^{EMG} can be written in the linked form:

$$J_L^{\text{EMG}} = \lambda J_{\text{KL}}^{\text{SN}}, \quad (4)$$

$$J_{\text{KL}}^{\text{SN}} \equiv a\phi^{-1}F^2 \exp[-v_F b \phi^{3/2}/F_L]. \quad (5)$$

Here: λ is an ‘‘uncertainty factor’’, of unknown functional dependence or value, called the *local pre-exponential correction factor*; $J_{\text{KL}}^{\text{SN}}$ is called the *kernel LECD for the SN barrier*; and a and b are the *first* and *second FN constants* as usually defined ([2], also see Table 2 here). The parameter v_F , which acts as the barrier-form correction factor for the SN barrier defined by ϕ and F_L , is a particular value of a special mathematical function $v(x)$, where x is the Gauss variable (i.e., the independent variable in the Gauss Hypergeometric Differential Equation) and usually is adequately given by the simple good approximation:

$$v_F = v(x = f) \approx 1 - f + (f/6) \ln f, \quad (6)$$

where f is to be interpreted as the *local scaled field* f_L as defined above or as its characteristic value f_C .

Integrating Eq. (4) over the emitter surface, we can find the *total emission current* I_e^{EMG} as:

$$I_e^{\text{EMG}} = A_n^{\text{EMG}} \lambda J_{\text{KL}}^{\text{SN}}, \quad (7)$$

where A_n^{EMG} is the related *notional emission area*. On defining the *formal emission area (for the SN barrier)* A_f^{SN} by:

$$A_f^{\text{SN}} = \lambda A_n^{\text{EMG}}, \quad (8)$$

and on assuming that the measured current I_m is equal to I_e^{EMG} , we obtain the $I_m(F_C)$ form of the EMG equation, as:

$$I_m(F_C) = A_f^{\text{SN}} a \phi^{-1} F_C^2 \exp[-v_F b \phi^{3/2}/F_C]. \quad (9)$$

The characteristic barrier field F_C can be related to the measured voltage V_m by the formula:

$$F_C = V_m / \zeta_C, \quad (10)$$

where ζ_C is a system-geometry parameter called the *characteristic voltage conversion length (VCL)*. This parameter ζ_C is constant for ideal FE devices and systems, because their $I_m(V_m)$ characteristics are determined only by the emission process and unchanging system geometry and surface properties. Additional background theory is given in [7-9].

The Theory of Murphy-Good (MG) Plots

Development of a Theoretical Equation for the MG Plot

This section reviews the theory [8] of Murphy-Good plots. To develop the theory, it is necessary to put Eq. (9) into the so-called *scaled form*. From Eq. (1), for characteristic values, we have $F_C = c_S^{-2} \phi^2 f_C$. We can define two scaling parameters $\eta(\phi)$ and $\theta(\phi)$ by:

$$\eta(\phi) = b c_S^2 \phi^{-1/2}, \quad (11)$$

$$\theta(\phi) = a c_S^{-4} \phi^3. \quad (12)$$

Inserting these three relationships into Eq. (9) yields the *scaled EMG equation*:

$$I_m(f_C) = A_f^{\text{SN}} \theta f_C^2 \exp[-v_F \eta / f_C], \quad (13)$$

where, for simplicity, we do not explicitly show that η and θ depend on ϕ . Making use of approximation (6), with $f = f_C$, yields (after some algebraic manipulation):

$$I_m(f_C) = A_f^{\text{SN}} \theta f_C^{(2-\eta/6)} \exp[\eta] \exp[-\eta/f_C]. \quad (14)$$

Eq. (14) now needs to be converted into a form where the measured voltage V_m is the independent variable. For an ideal device/system, the *reference measured voltage* V_{mR} is related to the *reference field* F_R (that corresponds to $f_C = 1$) by:

$$V_{mR} \equiv F_R \zeta_C. \quad (15)$$

Combining this with Eq. (10) and definition (1) for characteristic scaled field f_C yields:

$$f_C = F_C / F_R = V_m / V_{mR}. \quad (16)$$

In Eq. (14), we use Eq. (2) to replace $(2-\eta/6)$ by κ and use Eq. (16) to replace f_C , yielding:

$$I_m(V_m) = \{A_f^{SN} \theta \exp[\eta] V_{mR}^{-\kappa}\} V_m^\kappa \exp[-\eta V_{mR}/V_m]. \quad (17)$$

Dividing both sides by V_m^κ and taking the *natural logarithms* of both sides give us the equation for the *theoretical MG plot*:

$$\ln\{I_m/V_m^\kappa\} = \ln\{A_f^{SN} \theta \exp[\eta] V_{mR}^{-\kappa}\} - \eta V_{mR}/V_m. \quad (18)$$

Extracting Parameters from an MG Plot

MG plots have the form ($\log_{e,10}\{I_m/V_m^\kappa\}$ vs $1/V_m$), but we discuss only the natural logarithmic form here. We can define the following expressions:

$$Z \equiv 1/V_m \quad (19)$$

$$Y \equiv \ln\{I_m/V_m^\kappa\} \quad (20)$$

$$\alpha \equiv A_f^{SN} \theta \exp[\eta] V_{mR}^{-\kappa} \quad (21)$$

$$\beta \equiv -\eta V_{mR}. \quad (22)$$

For a given work-function value, β , α and $\ln\{\alpha\}$ are constants. On substituting Eqs. (19) to (22) into Eq. (18), we obtain the linear equation:

$$Y(X) = \ln\{\alpha\} + \beta Z. \quad (23)$$

Thus, $\ln\{\alpha\}$ is the *theoretical intercept* of the MG plot and β is its *theoretical slope*. It can also be seen that:

$$\alpha|\beta|^\kappa = A_f^{SN} \theta \eta^\kappa \exp[\eta] = A_f^{SN} (\theta \eta^2) \eta^{-\eta/6}. \quad (24)$$

From Eqs. (11) and (12), it follows that $\theta \eta^2 = ab^2 \phi^2$; so, we obtain:

$$\alpha|\beta|^\kappa = A_f^{SN} \theta \eta^\kappa \exp[\eta] = A_f^{SN} (ab^2 \phi^2) (\eta^{-\eta/6} \exp[\eta]). \quad (25)$$

Let S_{MG}^{fit} denote the slope of a straight line fitted to an experimental MG plot (made using natural logarithms) and let $\ln\{R_{MG}^{fit}\}$ denote the intercept that this line makes with the $(1/V_m) = 0$ axis. It follows from the equations above that an extracted value of formal emission area A_f^{SN} can be obtained from the extraction formula:

$$\{A_f^{SN}\}^{extr} = \Lambda_{MG} R_{MG}^{fit} |S_{MG}^{fit}|^\kappa, \quad (26)$$

where the *extraction parameter for the MG plot*, $\Lambda_{MG}(\phi)$, is given by:

$$\Lambda_{MG}(\phi) = 1/[(ab^2 \phi^2)(\eta^{-\eta/6} \exp[\eta])]. \quad (27)$$

Examples of the numerical dependence of $\Lambda_{MG}(\phi)$ on ϕ are given in [8].

It also follows that extracted values of V_{mR} and ζ_C can be obtained from:

$$\{V_{mR}\}^{extr} = -S_{MG}^{fit}/\eta, \quad (28)$$

$$\{\zeta_C\}^{extr} = -S_{MG}^{fit}/b\phi^{3/2}. \quad (29)$$

For large area field electron emitters (LAFEs), an extracted value of a characteristic (dimensionless) field enhancement factor (FEF) γ_{MC} , can then be obtained from:

$$\{\gamma_{MC}\}^{extr} = d_M/\{\zeta_C\}^{extr}, \quad (30)$$

where d_M is the macroscopic distance used to define the FEF (often, but not necessarily, the separation between two parallel planar plates).

Once a value has been extracted for V_{mR} , Eq. (14) can be used to determine (for an ideal device/system) the characteristic scaled-field value f_C that corresponds to any measured voltage. This is equivalent to using the extraction formula:

$$\{f_C\}^{extr} = V_m/\{V_{mR}\}^{extr} = -(\eta/S_{MG}^{fit})/(1/V_m). \quad (31)$$

This can be contrasted with the formula for extracting f_C -values from an FN plot made against $1/V_m$, which is [2]:

$$\{f_C\}^{extr} = -(s_t \eta/S_{FN}^{fit})/(1/V_m). \quad (32)$$

Clearly, the MG-plot formula does not contain the slope correction factor s_t .

Orthodoxy Test for a Murphy-Good Plot

Description of the Test

Since the orthodoxy test is based on comparing extracted ranges of f_C with acceptable and unacceptable ranges of f_C , as defined in Ref. [2] and shown in Tables 2 and 3 below, it is straightforward to apply an orthodoxy test to a Murphy-Good plot, by using Eq. (31) to extract apparent f_C -values.

To describe the test procedure, we use the simulated ideal $I_m(V_m)$ MG plot shown in Fig. 1. The method of generating this plot is described later in detail. The test procedure is as follows:

- (1) Fit a straight line to the experimental (or simulated) plot. Regression techniques can be used, but usually defining a straight line with a ruler is good enough.
- (2) Identify the position on the line that has the same X -coordinate (X_{up}) as the *lowest- X* data-

point you wish to use and determine the Y -coordinate (Y_{up}) of this position on the line. These coordinates (X_{up} , Y_{up}) define the *upper point* shown in Fig. 1. (The apparently contradictory terminology arises because "up" refers to the related value of V_m , rather than of $1/V_m$.)

- (3) Carry out a similar procedure for the *lower point* shown in Fig. 1.
- (4) Evaluate the (negative) *slope* $S_{\text{MG}}^{\text{fit}}$ of the fitted line, using the formula:

$$S_{\text{MG}}^{\text{fit}} = (Y_{\text{up}} - Y_{\text{low}})/(Z_{\text{up}} - Z_{\text{low}}). \quad (33)$$

- (5) Extract the range-defining scaled-field values, by applying Eq. (31) to the $(1/V_m)$ -values that define the ends of the range, as follows:

$$f_{\text{low}}^{\text{extr}} = -(\eta/S_{\text{MG}}^{\text{fit}})/(1/V_m)_{\text{low}}, \quad (34)$$

$$f_{\text{up}}^{\text{extr}} = -(\eta/S_{\text{MG}}^{\text{fit}})/(1/V_m)_{\text{up}}. \quad (35)$$

- (6) Apply the test condition, as derived from Tables 2 and 3.

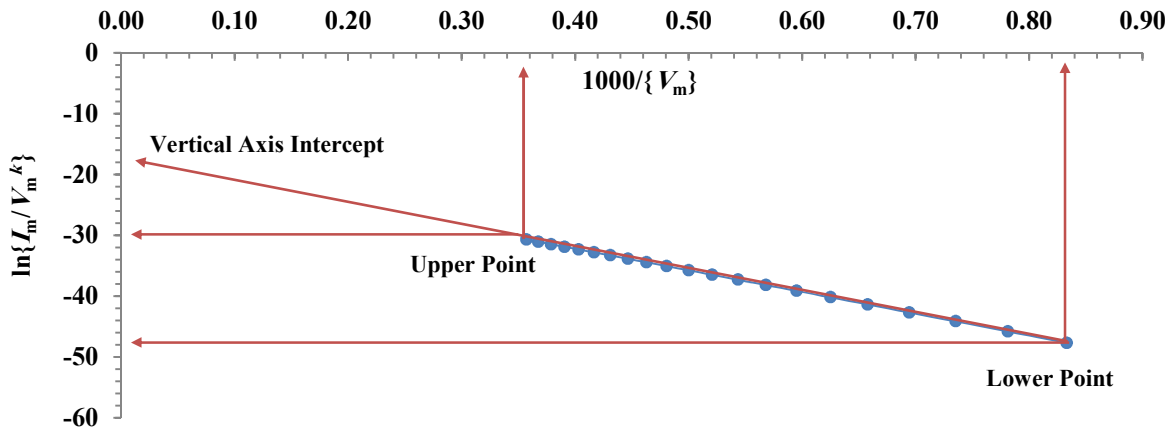


FIG. 1. Murphy-Good (MG) plot showing the upper and lower data points that define the range of voltages used. This plot covers the range from 1.2 to 2.8 kV (corresponding to the scaled-field range from 0.15 to 0.35), for an emitter with $\phi = 4.50$ eV. Voltages are measured in volts and currents in amperes. The parameter $k = \kappa = 2 - \eta/6$.

In Table 2, $f_{\text{low}}^{\text{extr}}$ is the extracted f_c -value for the lower point, $f_{\text{up}}^{\text{extr}}$ is the extracted f_c -value for the upper point and the superscripts (A/ NA) indicate the allowed/ disallowed limits for the extracted f_c -values. (For simplicity, the subscript

"C" is omitted in Eqs. (34) and (35) and in the tables). Table 3 shows the values of these limits for various work-function values [2]. If necessary, linear interpolation between these limits can be used.

TABLE 2. General criteria for the orthodoxy test.

Condition	Result	Explanation
$f_{\text{low}}^{\text{A}} \leq f_{\text{low}}^{\text{extr}}$ AND $f_{\text{up}}^{\text{extr}} \leq f_{\text{up}}^{\text{A}}$	Pass	Reasonable range
$f_{\text{low}}^{\text{extr}} \leq f_{\text{low}}^{\text{NA}}$ OR $f_{\text{up}}^{\text{NA}} \leq f_{\text{up}}^{\text{extr}}$	Fail	Clearly unreasonable range
$f_{\text{low}}^{\text{NA}} \leq f_{\text{low}}^{\text{extr}} \leq f_{\text{low}}^{\text{A}}$	Inconclusive	More investigation is needed
$f_{\text{up}}^{\text{A}} \leq f_{\text{up}}^{\text{extr}} \leq f_{\text{up}}^{\text{NA}}$	Inconclusive	More investigation is needed

TABLE 3. Orthodoxy-test range-limits, as a function of work function ϕ .

ϕ (eV)	$f_{\text{low}}^{\text{NA}}$	$f_{\text{low}}^{\text{A}}$	f_{up}^{A}	$f_{\text{up}}^{\text{NA}}$
5.50	0.09	0.14	0.41	0.69
5.00	0.095	0.14	0.43	0.71
4.50	0.10	0.15	0.45	0.75
4.00	0.105	0.16	0.48	0.79
3.50	0.11	0.17	0.51	0.85
3.00	0.12	0.18	0.54	0.91
2.50	0.13	0.20	0.59	0.98

The physical meanings of the two "fail" ranges are easy to state. The "low- f_c " one corresponds to the situation where the extracted f_c -value is thought too low for a measurable current to be detected in normal experiments; the "upper- f_c " one corresponds to the situation where the extracted f_c -value is higher than f_c -values at which the emitter is known to electroform (i.e., change shape due to atomic migration) or self-destruct. In both cases, it has to be concluded that the FE device/system is not ideal and that any characterization parameters extracted from the plot are likely to be spurious.

At a recent conference [10], we reported on the development of a prototype of a web tool that can apply an orthodoxy test to either an ML or an FN plot, and—if the test is passed—extract values of relevant emitter characterization parameters. The output of this prototype is shown in Fig. 2. During the work reported here, we have extended this prototype to include MG plots. At the time of writing, this prototype can be found at link [11]. The web tool is still under development and the final version will be made openly available in due course. It is also planned to develop a downloadable spreadsheet version.

ORTHODOXY Test for Field Emission Data Analysis Plots

Data Inputs

Project Name: MG Plot Example Graph Number: 1

Upper (Left) Point X-value: 0.00035 Upper (Left) Point Y-value: -24.6

Lower (Right) Point X-value: 0.00083 Lower (Right) Point Y-value: -42.3

X Axis Scaling: Y Axis Scaling:

Vertical Axis Intercept: —>Click here to obtain all Orthodoxy Test Outputs<—

Work-Function [eV]: 4.5 Plot Type: Murphy Good Logarithm Base: e

Orthodoxy Test Results

Project Name:	MG Plot Example	Test Result:	PASS
f_{low}^{extr} :	0.151	f_{up}^{extr} :	0.359

ORTHODOXY Test for Field Emission Data Analysis Plots

Data Inputs

Project Name: FN Plot Graph Number: 2

Upper (Left) Point X-value: 0.00035 Upper (Left) Point Y-value: -30.8

Lower (Right) Point X-value: 0.00083 Lower (Right) Point Y-value: -47.8

X Axis Scaling: Y Axis Scaling:

Vertical Axis Intercept: —>Click here to obtain all Orthodoxy Test Outputs<—

Work-Function [eV]: 4.5 Plot Type: Fowler Nordheim Logarithm Base: e

Orthodoxy Test Results

Project Name:	FN Plot	Test Result:	PASS
f_{low}^{extr} :	0.150	f_{up}^{extr} :	0.355

ORTHODOXY Test for Field Emission Data Analysis Plots

Data Inputs

Project Name: FN Plot Graph Number: 2

Upper (Left) Point X-value: 0.00035 Upper (Left) Point Y-value: -14.9

Lower (Right) Point X-value: 0.00083 Lower (Right) Point Y-value: -33.6

X Axis Scaling: Y Axis Scaling:

Vertical Axis Intercept: —>Click here to obtain all Orthodoxy Test Outputs<—

Work-Function [eV]: 4.5 Plot Type: Milikan Lauritsen Logarithm Base: e

Orthodoxy Test Results

Project Name:	FN Plot	Test Result:	PASS
f_{low}^{extr} :	0.149	f_{up}^{extr} :	0.354

FIG. 2. Current outputs of orthodoxy test web tool, for: (a) MG plot; (b) FN plot; (c) ML plot.

Consistency of Scaled-Field Extraction for MG Plot

For an MG plot, the physical consistency of the extraction process can be checked in the following simple way. Highly precise simulated ideal $I_m(V_m)$ data-sets can be generated by using: (a) Eqs. (13) and (14); (b) chosen values for system input parameters ϕ , V_{mR} and A_f^{SN} ; (c) a high-precision (HP) formula for $v(f)$, given in [7] and also in the Appendix to [8] (in the range $0 \leq f \leq 1$, $v(f)$ varies from 1 down to 0 and the HP formula yields $v(f)$ values known to have errors less than 8×10^{-10}); and (d) a chosen set of values for f_C .

Values of parameters used in (or related to) this simulation are shown in Table 4. The chosen values of f_C (as shown in Table 5) lie in the range $0.15 \leq f_C \leq 0.35$. This range is used because it is known [2] that, for tungsten FE devices, experimental f_C -values often lie within this

range. Table 5 also shows the resulting simulated values of quantities relevant to drawing the MG plot shown in Fig. 1.

For simplicity, the "lower" and "upper" data points on the MG plot are assumed to have the horizontal ("Z") and vertical ("Y") coordinates given by the values in columns 4 and 5 of Table 5, for the f_C -values 0.15 and 0.35. The resulting "fitted" slope, S_{MG}^{fit} , derived using Eq. (33), is shown in Table 4. The corresponding extracted values $\{f_C\}^{extr}$ are shown as the last column in Table 5 and are consistent with the input values, apart from a small systematic error of 0.27%. The cause of this error is the small discrepancy between the highly precise numerical formula for $v(f)$ used in the simulations and the "simple good approximation" (6) used to develop MG-plot theory, which is known to have an error of this order of magnitude. For practical purposes, the error is negligible.

TABLE 4. Parameters used for preparing simulation data for MG plot and extracted outputs related to its slope. Universal constants are shown to seven significant figures. Other parameters are shown to four or five figure precision. Asterisks indicate the chosen input-parameter values.

Parameter name	Symbol	Numerical value	Units
Input and related data			
First FN constant	a	1.541 434	$\mu A \text{ eV V}^{-2}$
Second FN constant	b	6.830 890	$eV^{-3/2} (V/nm)$
Schottky constant	c_S	1.999 985	$eV (V/nm)^{-1/2}$
Local work function*	ϕ	4.500	eV
Reference field	F_R	14.06	V/nm
Exponent scaling factor	η	4.637	—
Pre-exponent scaling factor	θ	6.774×10^{13}	$A \text{ m}^{-2}$
Voltage exponent (SN barrier)	κ	1.227	—
Reference measured voltage*	V_{mR}	8000	V
Voltage conversion length	ζ_C	56.90	nm
Formal area (SN barrier)*	A_f^{SN}	100.0	nm
Extracted data			
Fitted slope	S_{MG}^{fit}	-3.6995×10^4	Np V
Extracted value of V_{mR}	$\{V_{mR}\}^{extr}$	7987	V
Extracted value of ζ_C	$\{\zeta_C\}^{extr}$	56.73	nm

TABLE 5. Typical simulation data for a current-voltage $[I_m(V_m)]$ - based MG Plot and related extracted values of characteristic scaled field f_C .

f_C	V_m	I_m	$1/V_m$	$\ln\{I_m/V_m^\kappa\}$	$\{f_C\}^{extr}$	% error
—	(V)	(A)	(V ⁻¹)	—	—	
0.15	1200	2.755×10^{-15}	8.33×10^{-4}	-42.2	0.15040	0.27%
0.20	1600	8.747×10^{-12}	6.25×10^{-4}	-34.5	0.20054	0.27%
0.25	2000	1.172×10^{-9}	5.00×10^{-4}	-29.9	0.25067	0.27%
0.30	2400	3.196×10^{-8}	4.17×10^{-4}	-26.8	0.30081	0.27%
0.35	2800	3.488×10^{-7}	3.57×10^{-4}	-24.6	0.35094	0.27%

Table 4 also shows the extracted values of the reference measured voltage and the voltage conversion length. Again, these are very close to the input values.

The various good agreements just discussed, between extracted values and input values, serve to demonstrate the physical self-consistency of the MG plot and related extraction formulae, when these are applied to an orthodox FE device/system.

A more detailed investigation was also carried out, in order to confirm the high consistency level with which characterization parameters can be extracted from an MG plot for an orthodoxly behaving FE device/system (if likely statistical errors in measured data are disregarded). This investigation was similar to,

but performed independently of, that described in [8].

A data-set was created by using the same basic input data as above, but using f_C -values at intervals of 0.01 in the range $0.15 \leq f_C \leq 0.35$. This f_C -range was then divided into four different smaller ranges, in order to check how much the extracted slope S_{MG}^{fit} varied, depending on the particular range chosen. As shown in the first five columns of Table 6, it was found that, to a very good level of precision, the extracted MG-plot slope does not depend on the range used.

For the MG plot, the residual variations shown in Table 6 presumably result, as before, because the simple good approximation (6), used to derive MG-plot theory, is not an exactly precise expression for $v(f)$.

TABLE 6. Simulation of extraction of fitted slope S_{MG}^{fit} , for an MG plot, and fitted slope S_{FN}^{fit} for an FN plot, for various different ranges of characteristic scaled field f_C (and hence of predicted measured voltage V_m). Input data as in Table 4.

$(f_C)_{low}$	$(f_C)_{up}$	$(V_m)_{low}$	$(V_m)_{up}$	S_{MG}^{fit}	S_{FN}^{fit}
		(V)	(V)	(Np V)	(Np V)
0.16	0.20	1280	1600	-37006	-35902
0.21	0.25	1680	2000	-36992	-35577
0.26	0.30	2080	2400	-36981	-35256
0.31	0.35	2480	2800	-36974	-34938
Total variation :				32	964

Comparisons between the Plot Types

It is known that a Fowler-Nordheim plot is not expected to be an exactly straight line and that this gives rise to difficulties when interpreting a straight line fitted to an experimental FN plot. Within the framework of the prevailing "smooth planar metal emitter (SPME)" methodology almost-universally used for interpreting FE current-voltage data (see next section), the Murphy-Good plot was designed [8] to be "very nearly" a straight line and to remove these interpretation difficulties.

The superior quality of the MG plot is illustrated in Fig. 3, which shows the same set of basic $I_m(V_m)$ data plotted in the three ways under discussion. These plots are each based on a large set of data points, distributed over a wider f_C -value range than was used to produce Fig. 1. The MG plot is "very nearly" straight, as $1/V_m$ gets smaller, whereas the FN plot curves slightly downwards and the ML plot curves upwards.

The differences are small and normally difficult to see. However,—because the "lever effect" operates when extracting, from experimental data points well away from the $(1/V_m) = 0$ axis, a value for the intercept on the axis—these small differences significantly affect the accuracy with which the intercept value can be extracted.

To illustrate this quantitatively, we carried out for an FN plot a simulation exercise analogous to that described for an MG plot, using the same set of values of f_C , V_m and I_m . The results for the FN-plot fitted slope S_{FN}^{fit} are listed in the last column of Table 6: the variation in S_{FN}^{fit} (around 3%) is around 30 times higher than the variation in the fitted slope S_{MG}^{fit} for the MG plot. This again demonstrates the superiority of the MG plot as a tool for the precise analysis of $I_m(V_m)$ data (within the framework of SPME methodology).

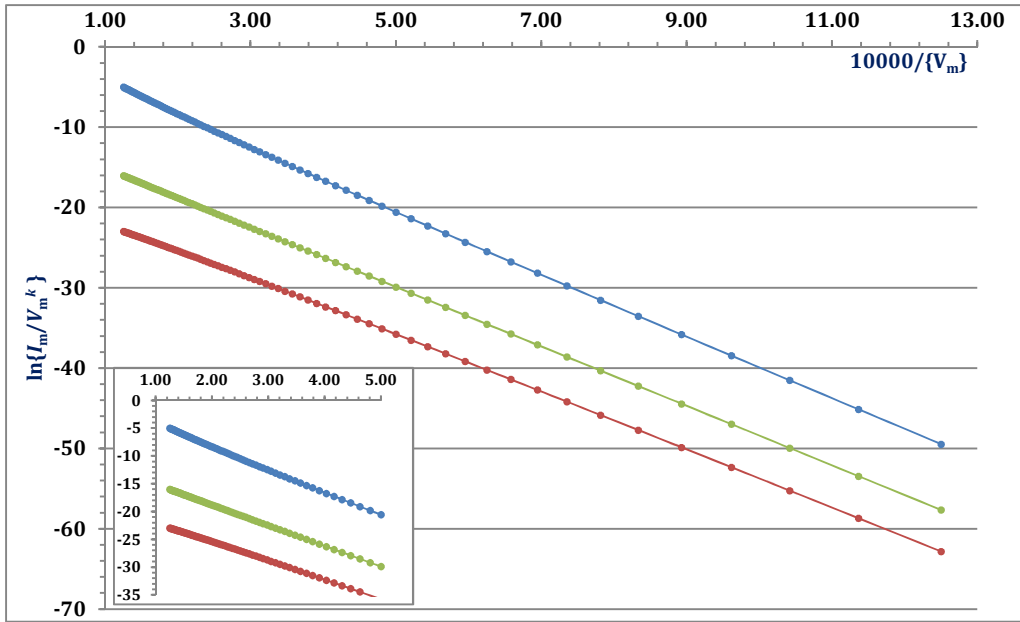


FIG. 3. Comparison between plot types. The ML plot (top) has voltage exponent $k = 0$; MG plot (middle) has $k = \kappa = 2 - \eta / 6$; FN plot (bottom) has $k = 2$. Voltages are measured in volts and currents in amperes.

Obviously, this difference between MG plots and FN plots aligns with the fact that Eq. (30) contains the slope correction factor s_t , but Eq. (29) does not. It is known (e.g. [7]) that the slope correction function $s(f)$ is a function of f , albeit a weak one. Thus, the "fitting value" $s_t [= s(f_t)]$ will be a function of the fitting value f_t (f_t is the value of characteristic scaled-field at which the experimental plot and the tangent to the theoretical plot are assumed to be parallel). However, normal practice is to take s_t as having the constant value 0.95; this is part of the cause of the observed discrepancy. (One of the problems with precise FN-plot analysis is determining the precise value of s_t).

Note that the numerics presented here have been generated specifically for the purpose of confirming the theoretical performance of an MG plot and comparing this with that of an FN plot. These numerics should not be interpreted as likely errors when MG plots are used to interpret real experimental data. In the application of FN plots and MG plots to real experimental data, other factors come into play, including noise in the data, non-ideality and weaknesses in SPME methodology.

Applicability to Non-Metals and Non-Planar Emitters

Obviously, the whole discussion here has been within the framework of the near-universal experimentalists' assumption (whatever the

material they are working with) that, theoretically, emitters can be treated as if: (a) the existence of atomic structure can be disregarded; (b) emission is coming from a limited area of a smooth planar surface of very large extent; and (c) Sommerfeld free electron-metal theory applies. This has been called elsewhere [8] the "smooth planar metal-like emitter" (SPME) methodology. The above set of assumptions is obviously unrealistic for some modern field electron emitters (in particular, for low-apex-radius carbon nanotubes). Clearly, for such emitters important questions are: "how should FE $I_m(V_m)$ data-analysis techniques be modified?" and (in the context of the present paper) "do new test(s) of FE 'ideality' need to be developed to replace the orthodoxy test?"

To a large extent, these questions are outside the scope of the present paper. The MG plot is a method for improving the precision of data analysis within the framework of SPME methodology and the focus of this paper has been on developing and testing a form of orthodoxy test applicable to an MG plot. These things have merit in themselves. Nevertheless, the following points deserve making.

In reality, the situation is more favourable than it might seem at first sight. (1) (Except perhaps for *very* sharp emitters) most of the causes of non-orthodoxy in FE devices/systems are associated with breakdown of the assumption that V_{mR} is constant, rather than with breakdown

of the assumption that the emission is adequately described by Murphy-Good theory. But, the causes of breakdown in the constant- V_{mR} assumption are much the same, whatever the emitter material. (2) In breakdown of the assumption that the EMG FE equation applies, the biggest factor will probably be that the true barrier is not an SN barrier. But, except possibly for *very* sharply curved emitters, the effect on FN-plot analysis is known to be a change in the value of s_t by a relatively small amount (typically of the order of a few percent); equivalently, one would expect (qualitatively) that the numerical validity of MG-plot analysis would be only slightly affected. (3) Differences in the electron supply function would be expected to have only a very small effect on the FN plot or MG plot slope, since they primarily affect the plot intercept. (4) With very sharp emitters, it is likely that both FN and MG plots would be noticeably curved and thus obviously non-orthodox. (5) Lack of strict applicability of orthodoxy test theory is more likely to result in a false determination that the FE device-system is non-orthodox, than a false determination that the FE device/system is orthodox. In fact, for further development of FE theory, a false determination of the first kind is of limited importance, because only results that pass the orthodoxy test are of scientific use. (6) The orthodoxy test is an "engineering triage" test, with generous margins of uncertainty built in.

Although more-exact tests for "ideality/non-ideality" may be developed in due course, this seems unlikely to happen soon. For the time being, we consider that the orthodoxy test, whether applied to FN or MG plots, is a technological test of "ideality or otherwise" that is sufficient for the purpose.

A final point is that development of data-analysis theory for non-metal emitters and for very sharp emitters is inhibited by lack of sufficiently good understanding of emission theory for such emitters. Probably a higher strategic priority is to first develop a form of data-analysis theory that deals with metal

emitters that have the shape of pointed needles or of rounded posts or are otherwise sharp (but not "very sharp"). This topic is beginning to be an active area of research and some of the issues involved have recently been discussed (see doi:10.13140/RG.2.2.32112.81927 and doi:10.13140/RG.2.2.35337.19041).

Summary

This paper has reviewed the theory of Murphy-Good (MG) plots and made some comparisons with the theories of Fowler-Nordheim (FN) plots and Millikan-Lauritsen (ML) plots. If experimental current-voltage characteristics conform to the so-called "Extended MG equation", then an experimental MG plot is expected to be "very nearly" a straight line and "much more nearly straight" than either an FN plot or an ML plot. We have confirmed this to be the case. Also, by extracting (from a simulated MG plot) slope values that correspond to different voltage ranges, we have shown that (for an MG plot taken from an orthodoxly behaving FE device/system) the process of slope extraction generates very consistent slope values, irrespective of voltage range

Because values of characteristic scaled field f_c can be extracted from an MG plot by using Eq. (31), an orthodoxy test can be applied to an MG plot by using the same rules about scaled-field ranges as in the case of the FN plot. A prototype web tool that can apply the orthodoxy test to any of the three types of FE data plot discussed (ML, MG or FN) is partially completed, though still under development. It is planned that there should eventually also be a downloadable spreadsheet version.

A particular application that we have in mind is to use the new data-analysis techniques discussed here; namely Murphy-Good plots and the related orthodoxy test, to enhance the analysis of experimental results obtained in the field emission laboratory at Mu'tah University.

References

- [1] International Standards Organization (ISO), "International Standard ISO 80000-1:2009 Quantities and Units-Part 1: General", (Geneva, ISO, 2009). See Section 6.
- [2] Forbes, R.G., Proc. R. Soc. Lond. A, 469 (2013) 20130271.
- [3] Fowler, R.H. and Nordheim, L., Proc. R. Soc. Lond. A, 119 (1928) 173.
- [4] Burgess, R.E., Kroemer, H. and Houston, J.M., Phys. Rev., 90 (1953) 515.
- [5] Nordheim, L.W., Proc. R. Soc. Lond. A, 121 (1928) 626.
- [6] Murphy, E.L. and Good, R.H., Phys. Rev., 102 (1956) 1464.
- [7] Forbes, R.G. and Deane, J.H.B., Proc. R. Soc. Lond. A, 463 (2007) 2907.
- [8] Forbes, R.G., R. Soc. Open Sci., 6 (2019) 190912.
- [9] Forbes, R.G., Deane, J.H.B., Fischer, A. and Mousa, M.S., Jordan J. Phys., 8 (2015) 125.
- [10] Mousa, M.S., Al-Laham M. and Forbes, R.G., "Testing of field emission orthodoxy by using a simple web application", 4th International Symp. on Dielectric Materials and Applications, (Amman, Jordan, May 2019), [Abstracts, p. 76].
- [11] (<http://fieldemissionanalysis.weebly.com/>).

Impedance Spectroscopy and Dielectric Properties of Carbon Nanotube-Reinforced Epoxy Polymer Composites

Z. Samir^a, S. Boukheir^{a,b}, R. Belhimria^a, M. E. Achour^a, N. Éber^c,
L. C. Costa^d and A. Oueriagli^b

^a *Laboratory of Material Physics and Subatomic, Faculty of Sciences, Ibn Tofail University, BP 242, 14000 Kenitra, Morocco.*

^b *Laboratoire LN2E, Faculté des Sciences, Université Cadi Ayyad, B.P. 2390, Marrakech, Morocco.*

^c *Institute for Solid State Physics and Optics, Wigner Research Centre for Physics, Hungarian Academy of Sciences, H-1525 Budapest, P.O.Box 49, Hungary.*

^d *Physics Department, University of Aveiro, 3810-193 Aveiro, Portugal.*

Doi : <https://doi.org/10.47011/13.2.3>

Received on: 08/08/2019;

Accepted on: 29/12/2019

Abstract: The aim of this work is to investigate the electric properties of carbon nanotube-reinforced epoxy polymer composites, using impedance spectroscopy, in the frequency range from 1 Hz to 10 MHz and over the temperature range from 25 to 105 °C. The dielectric response was analyzed using the complex permittivity and the electrical modulus formalisms, depending on temperature and filler concentration in the polymer matrix. Furthermore, an equivalent circuit model is proposed to describe the impedance response of carbon nanotubes/epoxy composites. The impedance studies disclosed the appearance of grain and grain-boundary effects, as confirmed by the Nyquist plot.

Keywords: Carbon nanotubes, Composites, Impedance spectroscopy, Equivalent circuit model, Grain effect, Grain-boundary effect.

Introduction

The use of carbon nanotubes (CNTs) in polymer nanocomposites has received much attention due to their enormous potential to enhance or modify particular mechanical and electric properties [1, 2]. These possibilities include the use of CNTs as conductive filler in insulating polymer matrices and as reinforcement in structural materials [3-8]. The aspect ratio, the amount and the dispersion states of carbon nanotubes determine how easily CNTs can interact with each other to construct an interconnecting network of percolation able to transfer electrons and phonons to improve the properties of the nanocomposite [9-11]. On the

other hand, epoxy resins are well established as advanced composites displaying a series of promising characteristics for a wide range of applications. So, CNT incorporation into epoxy resins results in carbon nanotubes / epoxy composites allowing many potential applications, ranging from microelectronics to aerospace [12-15].

As an extension of our recent research for exploring electrical properties [16-22], we report in this paper a detailed investigation of the dielectric and electrical properties of CNT-loaded epoxy polymers using impedance spectroscopy. Based on the obtained results, we

can readily make the following observations. On the one hand, the analysis of the behavior of complex electric modulus revealed the existence of two dielectric relaxation processes. One of these relaxations was associated with dipolar interactions at high frequencies, whereas the other, appearing at lower frequencies, was consistent with the interfacial polarization effect. On the other hand, an important thermoelectric phenomenon of transition was shown in this type of materials, below and above the conduction threshold (in our case the percolation threshold was found at $x = 2.7\%$), which is the positive temperature coefficient in resistivity effect (PTCR). In addition, we report the behavior of the impedance that reveals the presence of grain and grain-boundary effects confirmed by single and double arcs in the Nyquist representation.

Experimental

Materials

Multi-walled carbon nanotubes, with an outer diameter of about 50 nm, a length in the range of 10–20 μm and purity higher than 95 wt% (Cheap-Tubes, USA Laboratories), were selected in this work. The matrix used was an insulating epoxy matrix DGEBA (diglycidyl ether of bisphenol 1A) produced by A.W. Chesterton Company, Boston (USA). DGEBA had a DC electrical conductivity of the order of $1.4 \times 10^{-14} \text{ Sm}^{-1}$ and density of 1.19 g/cm^3 . The CNTs were dispersed uniformly through the polymer matrix in different concentrations, before adding 1% of hardener to make each mixture cohesive. The CNT/DGEBA gelation took 5 minutes after pouring into the mold. Finally, the obtained samples were unmolded after a few hours.

Differential scanning calorimetry (DSC) was carried out using a DSC Q100 V9.9 Build 303 (TA Instruments Co-USA) programmed between 0°C and 500°C , at a heating rate of $5^\circ\text{C}/\text{min}$. The results were used to determine the glass transition temperature of the composite for four selected nanotube concentrations besides the neat, undoped polymer. In our previous work [21], it was observed that the glass transition temperature decreased from 63°C for the neat polymer to 58°C for the sample with 5.0% CNT concentration. This decrease of the glass transition temperature can be attributed to the creation of a dense polymer package which is the result of this filler loading increase that affects the free volume of polymer.

Experimental Procedures

Electrical Impedance Spectroscopy Measurements

The impedance measurements on the samples were performed using a Novocontrol Alpha-A Analyzer combined with the ZG4 impedance interface, in a 4-wire arrangement in the frequency range of $1 \text{ Hz} < f < 10 \text{ MHz}$ under isothermal conditions, at temperatures ranging between 25°C and 105°C . The solid samples in the form of discs with a diameter of 13 mm and thickness of 2 mm were placed between two parallel plated electrodes. The studied composite materials were modeled by a lumped circuit consisting of a resistor and a capacitor connected in parallel. Impedance analysis provides a simple method to determine various complex formulations: permittivity (ϵ^*), modulus (M^*) and impedance (Z^*). The complex impedance $Z^*(\omega) = Z'(\omega) + jZ''(\omega) = 1/(G(\omega) + jB(\omega))$ can be converted into the complex permittivity $\epsilon^*(\omega) = \epsilon'(\omega) - j\epsilon''(\omega)$ by the relations:

$$\epsilon'(\omega) = B(\omega)d / \epsilon_0 A \omega \quad (1)$$

$$\text{and } \epsilon''(\omega) = G(\omega)d / \epsilon_0 A \omega \quad (2)$$

where $j = \sqrt{-1}$ is the imaginary unit, $\omega = 2\pi f$ is the circular frequency, A is the electrode area of the sample, d is its thickness and ϵ_0 is the permittivity of vacuum ($\epsilon_0 = 8.85 \times 10^{-12} \text{ Fm}^{-1}$). The terms $G(\omega)$ and $B(\omega)$ are the conductance and the susceptance of the samples. The electrical modulus, $M^*(\omega)$, is defined in terms of the reciprocal of the complex relative permittivity, $\epsilon^*(\omega)$:

$$M^*(\omega) = 1/\epsilon^*(\omega) = M'(\omega) + jM''(\omega) \quad (3)$$

where $M'(\omega)$ and $M''(\omega)$ are the real and imaginary parts of the electrical modulus which can be expressed by using the complex dielectric constants *via* the following relations:

$$M'(\omega) = \epsilon'(\omega) / (\epsilon'^2(\omega) + \epsilon''^2(\omega)) \quad (4)$$

$$M''(\omega) = \epsilon''(\omega) / (\epsilon'^2(\omega) + \epsilon''^2(\omega)) \quad (5)$$

Results and Discussion

Dielectric and Electrical Modulus Properties

The complex permittivity of the specific samples of $x = 0.8\%$ and $x = 5.0\%$ (x is the concentration of carbon nanotubes) is shown in Fig. 1 and Fig. 2, respectively, which depict the imaginary part and in the inset the real part of the complex permittivity as a function of frequency, for different temperatures. For the composite with a lower CNT volume fraction; i.e., $x = 0.8\%$ (Fig. 1), we can observe that a relaxation process is present, which is expressed by the maximum in the imaginary part of the complex permittivity and the inflection in the real part. The amplitude of this maximum increases as the temperature increases. The relaxation phenomenon is probably the result of

the combination of two principal polarization mechanisms [23-25]. The first one corresponds to the dielectric properties of the polymer, which is generally attributed to the re-orientation of dipoles. The other mechanism is related to the CNT presence. This polarization mechanism causes an electric charge concentrated at the CNT/epoxy interface.

For the higher CNT volume concentration, i.e., $x = 5.0\%$ (Fig. 2), the relaxation peak vanishes. Indeed, the material is characterized by the formation of an infinite cluster of CNT particles, which allows the displacement of electrons through large distances. Interfacial polarization phenomena on surfaces of the finite clusters can always exist, but they are masked by the process of conduction.

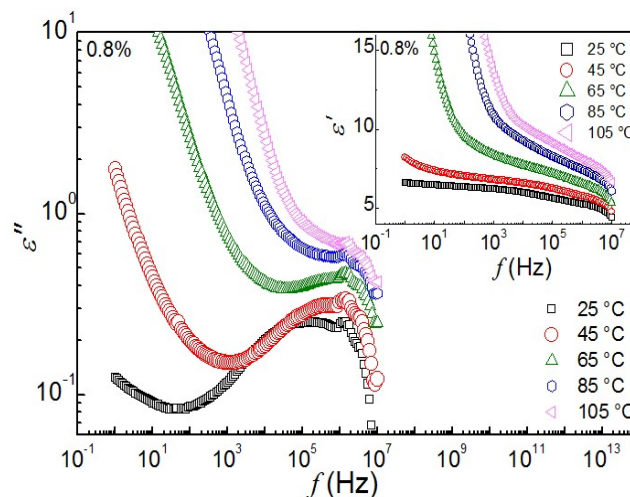


FIG. 1. Frequency dependence of the real and imaginary parts of the complex permittivity for various temperatures at the concentration of $x = 0.8\%$.

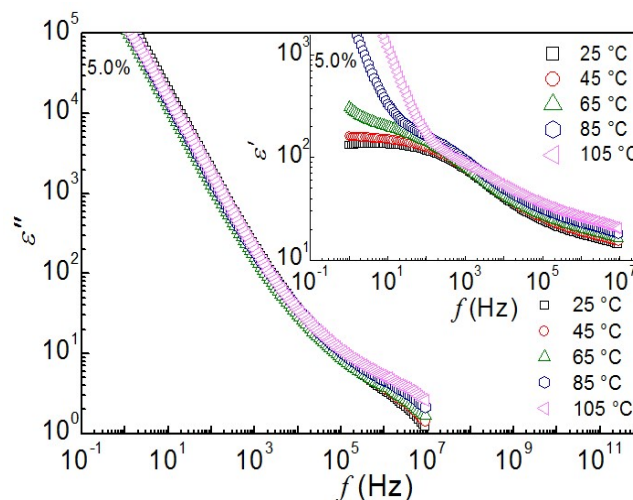


FIG. 2. Frequency dependence of the real and imaginary parts of the complex permittivity for various temperatures at the concentration of $x=5.0\%$.

Figs. 3 and 4 show the modulus spectra for two CNT concentrations ($x = 0.8\%$ and $x = 5.0\%$, respectively), at different temperatures. In Fig. 3, we observe the presence of one relaxation at the temperatures of $25\text{ }^{\circ}\text{C}$ and $45\text{ }^{\circ}\text{C}$ and the existence of two successive relaxations above the temperature $45\text{ }^{\circ}\text{C}$. The first relaxation, at high frequencies, represents the orientation of

dipolar interaction groups, whereas the other, at low frequencies, is related to the interfacial polarization at the CNT/epoxy interfaces that gives rise to the Maxwell-Wagner-Sillars (MWS) polarization [26,27]. For $x = 5.0\%$ (Fig. 4), the two relaxations are superimposed giving a single distorted peak in $M''(\omega)$ at all temperatures.

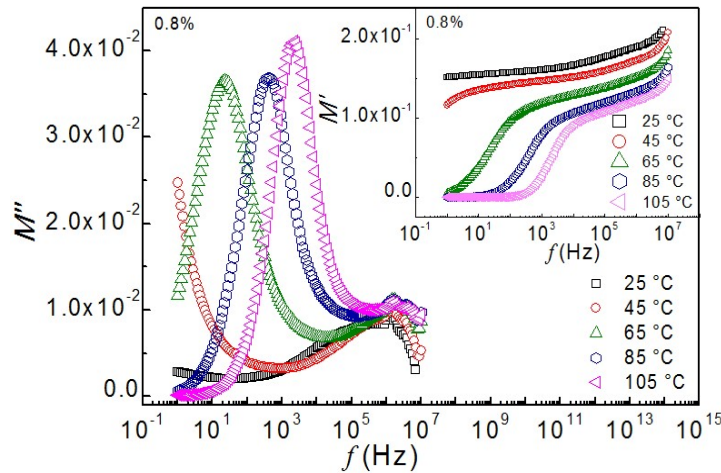


FIG. 3. Imaginary part of the electric modulus as a function of frequency for various temperatures at the concentration of $x = 0.8\%$. The inset is a similar plot for the real part of the electric modulus.

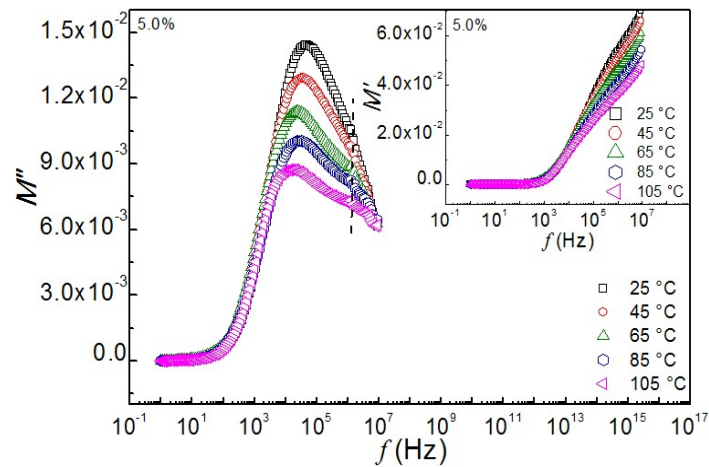


FIG. 4. Imaginary part of the electric modulus as a function of frequency for various temperatures at the concentration of $x = 5.0\%$. The inset is a similar plot for the real part of the electric modulus.

Impedance Analysis

The impedance spectra of CNT/epoxy composites were analyzed by fitting to an equivalent electrical circuit which, instead of being a parallel R-C circuit, was the parallel combination of a resistance and a constant phase element (CPE) on the basis of brick-layer model [27–30]. The CPE was modeled as a non-ideal capacitor:

$$Z_{CPE} = 1 / [Q(j\omega)^n] \quad (6)$$

Here, Z_{CPE} is the impedance of the constant phase angle component, $0 < n < 1$ and Q is a constant. The CPE becomes equivalent to a capacitance when $n = 1$ [31]. This equivalent circuit model (Fig. 5a) is usable if only grain effect is present. If an additional grain-boundary effect is also to be taken into account, the equivalent circuit model has to be supplemented by a second, similar subcircuit of parallel R and CPE, connected in series (Fig. 5b). For the equivalent circuit models proposed, the total impedances Z_a and Z_b in the simple (Fig. 5a)

and the extended (Fig. 5b) equivalent circuit models, respectively, can be expressed as:

$$Z_a = \frac{R_g}{1 + R_g Q_g (j\omega)^{n_g}} \quad (7)$$

$$Z_b = \frac{R_g}{1 + R_g Q_g (j\omega)^{n_g}} + \frac{R_{gb}}{1 + R_{gb} Q_{gb} (j\omega)^{n_{gb}}} \quad (8)$$

Here, R_g and R_{gb} are the grain and the grain-boundary resistances, respectively, Q_g , Q_{gb} , n_g , and n_{gb} are constants.

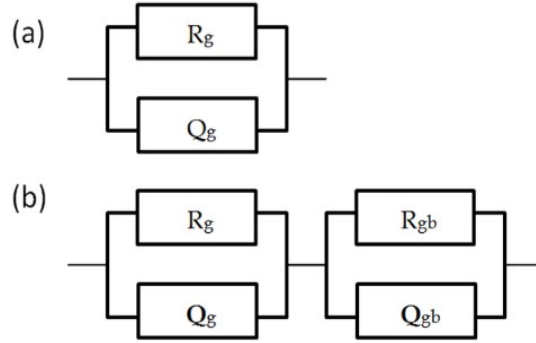


FIG. 5. Equivalent electrical circuits used to fit the impedance spectra of CNT/epoxy composites taking into account the effects related to (a) grain effect only, (b) both grain and grain-boundary effects.

To extract more information on the electrical responses and the structure-properties relationship, complex impedance spectroscopy is normally used. The Nyquist plots $Z''(Z')$ of the complex impedance for CNT/epoxy composites with 0.8% and 5.0% CNT content are shown in Figs. 6a-6b, respectively, for various temperatures from 25 °C to 105 °C. At room temperature measurements, no semicircle formation takes place. With increasing temperature, the behavior of Z'' versus Z' transforms into semicircles; this should be attributed to the grain effect in CNT particles (Fig. 6a) [32, 33]. In Fig. 6b, all the plots exhibit one single arc from room temperature (25 °C) to 85 °C representing grain effect only. When the temperature reaches 105 °C, a small segment of an arc appears at the low frequency side, which connects to the first semicircle. This suggests a process, in which the grain effect is gradually replaced by grain-boundary effect at increasing temperature [34]. It is also observed that the radius of the semicircles first increases, but then decreases with the increase in temperature, indicating a non-monotonic behavior of resistivity. Its depression at high temperatures is

due to the statistical distribution of relaxation times.

Fig. 7 shows the temperature dependence of the maximum value Z''_{max} of the impedance $Z''_{max}(\omega)$ for the three concentrations. In Figs. 7b and 7c, it can be seen that Z''_{max} increased first with increasing temperature, which is obviously a positive temperature coefficient in resistivity (PTCR) effect, while negative temperature coefficient in resistivity (NTCR) effect appeared when the temperature was over 65 °C. For composites with 3.0% and 5.0% of CNT content, both the PTCR and the NTCR effects were very strong, while at 0.8% CNT content (Fig. 7a), only the NTCR effect was detectable. The PTCR could be attributed to volume expansion of the composites, which resulted in an increase of the distance between conductive tubes. However, the expansion could be paused when the distance of expansion was over the grid size of the cross-linked network in the rubber-matrix composites. With a further increase in temperature, electrons with enough energy could have an electron tunneling effect, which resulted in the NTCR effect.

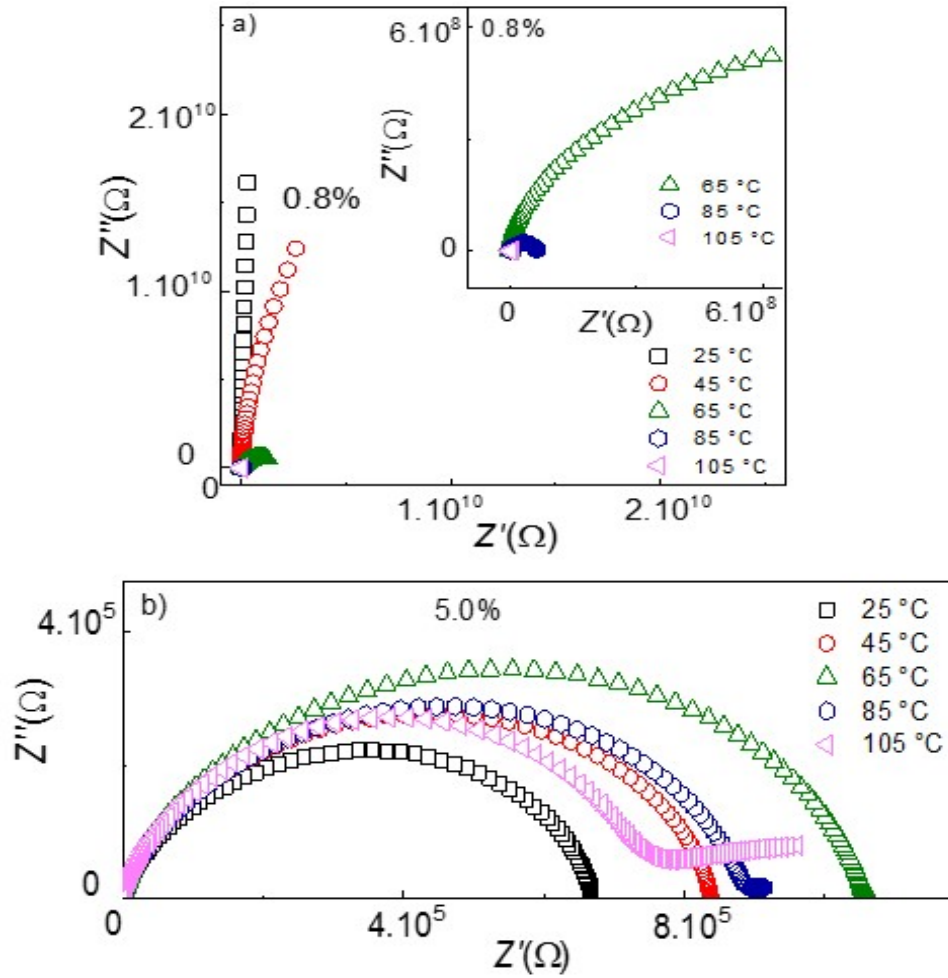


FIG. 6. Nyquist plots of the impedance of $x = 0.8\%$ (a) and $x = 5.0\%$ (b) CNT measured at different temperatures.

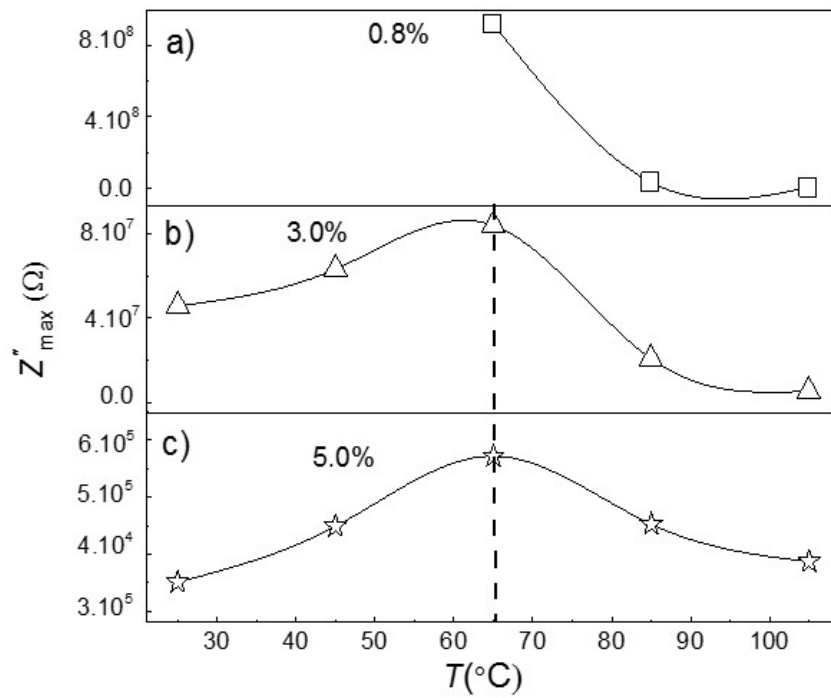


FIG. 7. Z''_{\max} vs. temperature, for $x = 0.8\%$, $x = 3.0\%$ and $x = 5.0\%$ CNT concentrations.

Fig. 8 compares the Nyquist plots of the complex impedance (symbols) with fitted data (solid line). For $x = 0.8\%$, it is clearly shown that semicircular arcs are formed, whose shape remains almost the same as changing the temperature (Figs. 8a-8b). The experimental data was fitted with the impedance of the equivalent circuit in Fig. 5a, consisting of a parallel combination of a resistance and a CPE and representing the grain effect. For $x = 5.0\%$, at low temperature (85°C , Fig. 8c), the same equivalent circuit could be employed. However, at the higher temperature of 105°C , a small segment of arc appeared from the low frequency side, which is connected to the first semicircle (Fig. 8d). This suggests a process, in which the grain effect is gradually replaced by the grain-boundary effect. In this case, the fitted curve was

obtained using the extended equivalent circuit in Fig. 5b, consisting of two subcircuits in series that correspond to the two semicircular arcs. In addition, this also indicates that there exist two different relaxation processes and there is a distribution of the relaxation time rather than one particular relaxation time. The fitted parameters of grain and grain-boundary effects are tabulated in Table 1. The spectra reconstructed with the fitted parameters and the measured impedance spectra show good agreement with each other. Table 1 presents parameters also for CNT concentrations, whose spectra were not shown. From this table, it is found that the resistances R_g and R_{gb} decrease, while Q_g and Q_{gb} increase with CNT loading. The behavior for $x = 2.5\%$ was qualitatively the same as for $x = 0.8\%$, while for $x = 3.0\%$, it was similar to $x = 5.0\%$.

TABLE 1. Fitted parameters of the Nyquist plots of CNT/epoxy composites with different CNT concentrations.

x (%)	T ($^\circ\text{C}$)	R_g (Ω)	Q_g (F)	n_g	R_{gb} (Ω)	Q_{gb} (F)	n_{gb}
0.8	25	-	-	-	-	-	-
	65	1.72×10^9	7.45×10^{-11}	0.74	-	-	-
	105	7.47×10^6	7.89×10^{-11}	0.86	-	-	-
2.5	25	-	-	-	-	-	-
	65	0.10×10^9	0.25×10^{-9}	0.74	-	-	-
	105	1.72×10^6	0.32×10^{-9}	0.80	-	-	-
3.0	25	9.11×10^7	0.20×10^{-9}	0.79	-	-	-
	65	0.15×10^9	0.21×10^{-9}	0.79	-	-	-
	105	1.05×10^7	0.16×10^{-9}	0.86	5.66×10^6	7.92×10^{-8}	0.56
5.0	25	6.71×10^5	0.68×10^{-9}	0.76	-	-	-
	65	1.60×10^6	0.89×10^{-9}	0.75	-	-	-
	105	7.35×10^5	0.57×10^{-9}	0.81	3.39×10^5	0.73×10^{-6}	0.54

Conclusion

The present work reports the results of our investigation on the electrical properties of CNT/epoxy composites. Both the permittivity and the modulus formalisms were used to interpret the relaxation processes at different temperatures. However, the electric modulus formalism was capable of revealing the interfacial relaxation which, in most cases, is covered by the conductivity of the material when represented in the dielectric. Positive temperature coefficient in resistivity and negative temperature coefficient in resistivity were also exploited, which is strongly dependent on the carbon nanotube content. A novel equivalent circuit model is proposed to describe the impedance response of the composites. The

impedance measurements reveal the presence of grain and grain-boundary effects and confirm the temperature-dependent non-Debye type electrical relaxation processes in CNT/epoxy composites.

Acknowledgement

Financial support by the Moroccan (CNRST) - Hungarian (NKFIH) bilateral project TÉT_12_MA-1-2013-0010 as well as by the Budapest Neutron Centre (www.bnc.hu) is gratefully acknowledged. We also thank FEDER funds through the COMPETE 2020 Programme and National Funds through FCT - Portuguese Foundation for Science and Technology under the project UID/CTM/50025/2019.

References

- [1] Breuer, O. and Sundararaj, U., *Polym. Compos.*, 25 (2004) 645.
- [2] Xie, X.L., Mai, Y.W. and Zhou, X.P., *Mater. Sci. Eng. Rep.*, 49 (2005) 112.
- [3] Allaoui, A., Bai, S., Cheng, H.M. and Bai, J.B., *Compos. Sci. Technol.*, 62 (2002) 1998.
- [4] Putz, K.W., Mitchell, C.A., Krishnamoorti, R. and Green, P.F., *J. Polym. Sci. B.*, 42 (2004) 2293.
- [5] Du, F., Fischer, J.E. and Winey, K.I., *J. Polym. Sci. B.*, 41 (2003) 3338.
- [6] Dai, J., Wang, Q., Li, W., Wei, Z. and Xu, G., *Mater. Lett.*, 61 (2007) 29.
- [7] Valentini, L., Puglia, D., Frulloni, E., Armentano, I., Kenny, J.M. and Santucci, S., *Compos. Sci. Technol.*, 64 (2004) 33.
- [8] Ounaies, Z., Park, C., Wise, K.E., Siochi, E.J. and Harrison, J.S., *Compos. Sci. Technol.*, 63 (2003) 1646.
- [9] Sandler, J., Shaffer, M.S.P., Prasse, T., Bauhofer, W., Schulte, K. and Windle, A.H., *Polymer.*, 40 (1991) 5971.
- [10] Ivanov, E., Kotsilkova, R. and Krusteva E., *J. Nanopart. Res.*, 13 (2011) 3403.
- [11] Jin, F.L. and Park, S.J., *Carbon Lett.*, 14 (2013) 13.
- [12] Pourzahedi, L., Zhai, P., Isaacs, J.A. and Eckelman, M.J., *J. Clean Prod.*, 142 (2017) 1978.
- [13] Verma, S., *US Patents.*, 5,872,332A, Feb. 23, 1999.
- [14] Albano, M., Micheli, D., Gradoni, G., Morales, R.B., Marchetti, M., Moglie, F. and Primiani, V.M., *Acta Astronaut.* 87 (2013) 39.
- [15] Gooch, J.W. and Daher, J.K., "Electromagnetic Shielding and Corrosion Protection for Aerospace Vehicles", (New York, NY, USA: Springer, 2007).
- [16] Samir, Z., El Merabet, Y., Graça, M.P.F., Teixeira, S.S., Achour, M.E. and Costa, L.C., *Polym. Compos.*, 39 (2016) 1302.
- [17] Samir, Z., El Merabet, Y., Graça, M.P.F., Teixeira, S.S., Achour, M.E. and Costa, L.C., *J. Compos. Mater.*, 51 (2017) 1837.
- [18] Boukheir, S., Len, A., Füzi, J., Kenderesi, V., Achour, M.E., Éber, N., Costa, L.C., Outzourhit, A. and Oueriagli, A., *J. Appl. Polym. Sci.*, 134 (2016) 44514.
- [19] Boukheir, S., Len, A., Füzi, J., Kenderesi, V., Achour, M.E., Éber, N., Costa, L.C., Outzourhit, A. and Oueriagli, A., *Spectroscopy Letters*, 50 (2016) 188.
- [20] Samir, Z., Belhimria, R., Boukheir, S., Achour, M.E. and Costa, L.C., *Jordan J. Phys.*, 11 (1) (2018) 35.
- [21] Boukheir, S., Samir, Z., Belhimria, R., Kreit, L., Achour, M.E., Éber, N., Costa, L.C., Oueriagli, A. and Outzourhit, A., *J. Macromol. Sci. B*, 57 (2018) 221.
- [22] Samir, Z., Boukheir, S., Belhimria, R., Achour, M.E. and Costa, L.C. *Journal of Superconductivity and Novel Magnetism*, 32 (2019) 185. <https://doi.org/10.1007/s10948-018-4696-6>.
- [23] Asami, K., *Prog. Polym. Sci.*, 27 (2002) 165.
- [24] Barucci, M., Bianchini, G., Gottardi, E., Peroni, I. and Ventura, G., *Cryogenics*, 39 (1999) 966.
- [25] Achour, M.E., Salome, L., Benaboud, K., Carmona, F. and Miane, J.L., *Adv. Mater. Res.*, 1 (1994) 468.
- [26] Belattar, J., Graça, M.P.F., Costa, L.C., Achour, M.E. and Brosseau, C., *J. Appl. Phys.*, 107 (2010) 124111.
- [27] Mcclory, C., Seow, J.C. and McNally, T., *Aust. J. Chem.*, 62 (2009) 785.
- [28] Kolekar, Y.D., Sanchez, L.J. and Ramana, C.V., *J. Appl. Phys.*, 115 (2014) 144106.
- [29] Mohanty, S., Choudhary, R.N.P., Padhee, R. and Parida, B.N., *Ceram. Int.*, 40 (2014) 9025.
- [30] Nayek, C., Murugavel, P., Kumar, S.D. and Subramanian, V., *Appl. Phys. A*, 120 (2015) 622.
- [31] Orazem, M.E., Frateur, I., Tribollet, B., Vivier, V., Marcelin, S., Pèbère, N. and Musiani, M., *J. Electrochem. Soc.*, 160 (2013) C225.

- [32] Sanli, A., Müller, C., Kanoun, O., Elibol, C. and Wagner, M.F.X., *Compos. Sci. Technol.*, 122 (2016) 26.
- [33] Messaoud, N.B., Ghica, M.E., Dridi, C., Ali, M.B. and Brett, C.M., *Sens. Actuator B-Chem.*, 253 (2016) 522.
- [34] Kumar, M., Shankar, S., Kumar, S., Thakur, O. P. and Ghosh, A.K., *Phys. Lett. A.*, 381 (2017) 386.

Jordan Journal of Physics

REVIEW ARTICLE

Structure, Synthesis and Applications of ZnO Nanoparticles: A Review

H. H. Azeez^a, A. A. Barzinjy^{a,b} and S. M. Hamad^{c,d}

^a Department of Physics, College of Education, Salahaddin University-Erbil, Kurdistan Region, Iraq.

^b Department of Physics Education, Faculty of Education, Tishk International University, Erbil, Kurdistan Region, Iraq.

^c Scientific Research Centre, Soran University, Soran 44008, Kurdistan Region, Iraq.

^d Computer Department, Cihan University-Erbil, Kurdistan Region, Iraq.

Doi : <https://doi.org/10.47011/13.2.4>

Received on: 08/08/2019;

Accepted on: 1/12/2019

Abstract: Nanotechnology deals with the creation and utilization of materials at a nanoscale. Nanoparticles, in general, possess enormous surface area per unit volume and have explicit characteristics. Zinc oxide (ZnO) - based nanomaterials have been recognized to be of countless uses for numerous important requests from the beginning of nanoscience as a result of the great quantity of zinc element and the comparatively simple adaptation of its oxide to nanostructures. Currently, ZnO as nanoparticles, nanowires, nanofibers in addition to other classy nanostructures occurs amongst the innovator nanomaterials utilized in solar cell systems, fuel cells, water purification and biomedical fields. ZnO nanoparticles had been a research target for many investigations because of their vast band-gap and extraordinary exciton binding energy. The performance of ZnO nanoparticles is completely different from those of corresponding bulk materials, through enhancing the properties and using lesser amount of materials, which leads to price reduction. The main purpose behind this review article is to give a deep view on structure, synthesis and applications of ZnO nanoparticles prepared through various approaches to give the reader a comprehensive understanding.

Keywords: ZnO, Nanoparticles, Structure, Synthesis, Applications.

Introduction

In recent years, among metal oxide NPs, a lot of research focused on zinc oxide, because it has strange chemical, optical, magnetical and mechanical characteristics that are clearly unlike those of corresponding bulk materials [1]. Currently, nanotechnology is available in different scientific fields. Also, different techniques have been utilized for the operation of nanoparticles (NPs) in nano-scale range. NPs are an extensive type of materials comprising

particulate materials which possess at least one dimension below 100 nm [2].

ZnO has distinctive chemical and physical properties; for instance, higher photostability, higher chemical stability, naturality, paramagnetism, a wide range of radiation absorption and higher electrochemical coupling coefficient [3]. Due to famous performance of ZnO nanostructured material in photonics, optics and electronics, it acquired great attention. The lack of a center of symmetry in wurtzite

structure, joined with great electro-mechanical coupling, strong pyroelectric and piezoelectric properties are reasons behind using ZnO in piezoelectric detectors and mechanical actuators. Moreover, zinc oxide possesses a broad energy gap (3.370 eV), which is typical for a compound semiconductor, sufficient for different types of applications; for instance, in power generators, solar cells, ultraviolet (UV) lasers [4], gas detectors [5], photo catalysts, field emission devices, capacitors [6, 7]. It can also be utilized for clear UV resistance coating, electro-photography, photo-printing, electrochemical and electromechanical nano-devices, anti-bacterial agents, sun blockers, anti-hemorrhoids, cosmetic wound healing [8], eczema and excoriation from human medicine [9]. Zinc oxide powder is broadly utilized as an additive in many products and materials involving ceramics [10], rubber, cement, lubricants, glass, paints, adhesives, ointments, plastics, pigments, sealants, food, ferrites, batteries and fire retardants [8]. ZnO-based coating can be utilized as a protecting layer against moisture in woody samples [11].

ZnO nanoparticles can be classified depending on physical and chemical properties; for instance, crystal structure, shape, surface area, size and other properties changing with size reduction. This has given rise to the improvement of methods to prepare mixtures [12], as well as mechanic and chemical procedures [13, 14], procedure of precipitation [15, 16], surfactant precipitation [17], sol-gel [18], hydrothermal and solvothermal procedures [19], technique of microwave [20], emulsion [21], technique of microemulsion [22], CVD (chemical vapor deposition) [23], MBE (molecular beam epitaxy) [24], spray method [25], laser ablation [26], among others.

To our best knowledge, there is only a few review articles regarding ZnO NPs, such as Ref. [27] and Ref. [28]. Thus, due to the importance of ZnO NPs and their potential applications, this review article is originally designed to give a comprehensive understanding of the structure and the main approaches of synthesizing ZnO NPs, which are not fully covered by previous review. Further detail has been given to chemical and physical properties. The mechanical, electro-chemical, electrical and photoluminescence

properties are among the properties that took more explanation during this investigation.

Zinc Oxide Structure

Zinc oxide nanoparticles are categorized among the materials that have potential applications in many areas of nanotechnology [29, 30]. ZnO possesses one-, two- and three-dimensional structures. 1D structure involves tubes, needles, ribbons, nanorods helices, belts, combs, wires, rings and springs [12]. Two-dimensional structure involves nanoplates and nanosheets that can give us zinc oxide. However, three-dimensional structure of zinc oxide includes snowflakes, coniferous, urchin-like flowers and dandelions. Zinc oxide gives greatly different particles among materials [27]. Also, zinc oxide in different shapes and structures can be seen in Fig. 1.

Crystal Structure

Crystallization of zinc oxide exists in two types: cubic zinc-blende and hexagonal wurtzite structure. The structure of wurtzite is stable and common in ambient situations. At ambient temperature and pressure, zinc oxide is crystal in the wurtzite structure type B4, as displayed in Fig. 2. It is a hexagonal lattice, going to the P6₃mc space group and can be characterized *via* two connecting lattices O²⁻ and Zn²⁺; each Zn ion is bounded *via* a tetrahedral of O²⁻ ions or *vice versa*. The coordination of this tetrahedral provides an increase to polar symmetry on the hexagonal axis [10]. This polarity is superior to a few properties of zinc oxide, involving (piezoelectricity and spontaneous polarizations). However, it is a hindrance factor from crystal growth, defect generation and etching. The ultimate face terminations of wurtzite zinc oxide are the polar (Zn) terminated (0001) and (O) terminated (000.1) faces [c-axis oriented], as well as the nonpolar (11.2) (a-axis) and (10.1) faces. This can commonly hold an equal number of atoms of Zn and O. On the other hand, polar faces are identified to possess different physical and chemical properties and the (O) terminated face possesses a slightly changed electronic structure compared to the other three faces of O [35].

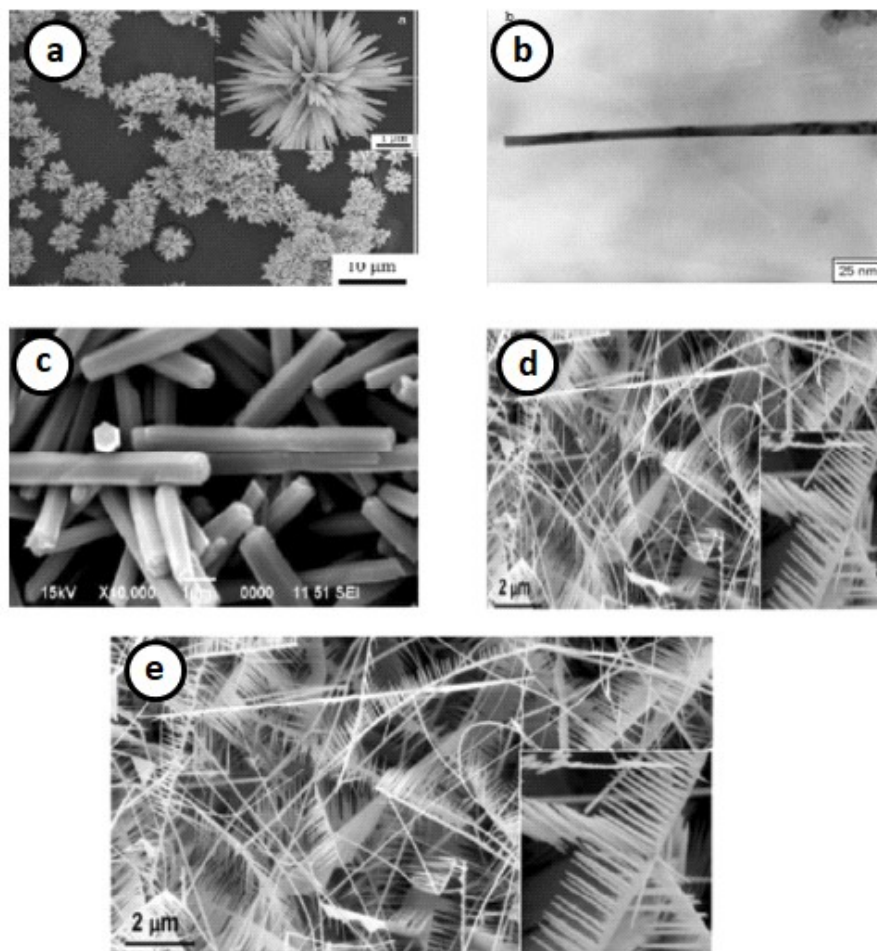


FIG. 1. Different structures and shapes of zinc oxide, (a) flower [31], (b) wire [32], (c, d) rod & mushroom [33], (e) comb [34].

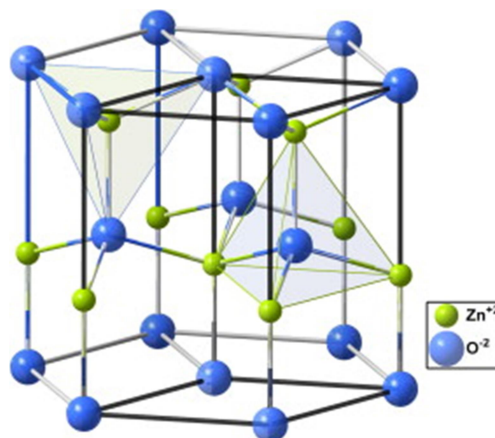


FIG. 2. Crystal structure of zinc oxide NPs [10].

Preparation Methods of ZnO NPs

Preparation of nanoparticles simply requires a low-cost and high-yield process. The approaches to preparing zinc NPs can be detached into solid phase, liquid phase and gas phase procedures. The solid phase methods involve mechanical milling and mechanochemical processes. The liquid phase methods involve exploding wire,

laser ablation, decomposition process and solution reduction. However, the gas phase methods include laser ablation, exploding wire, gas evaporation and spark discharging [36], as well as chemical bath deposition (CBD) [37], green preparation [7] and wet chemical approach [38].

Mechanochemistry

Mechanochemistry is a field that deals with thermal or ultra-fast chemical reactions between solids or between solids and surrounding gaseous or liquid molecules under mechanical forces. Mechanochemistry includes the composition of mechanical and chemical incidence at molecule scale and involves mechanical breaking and chemical display of straining of mechanics in solids. Mechanochemical preparation is different from ball milling. A classic ball milling procedure under inert atmosphere effects in a reasonable drop of particle powder size yields eventually the creation of nano-size grains in micro-size particles. The mechanochemical treatment includes the beginning of a displacement solid state reaction throughout the ball milling procedure in which nano-scale size particles drop to near 5 nm in size fixed through big particle production phase [39]. Synthesis by mechanochemical processing was predicted by Ao *et al.* [13]. They prepared zinc oxide in a standard size crystallite of 21 nanometers. Milling procedure took six hrs, manufacturing ZnCO_3 through the zinc oxide precursor. However, calcination of the precursor at 600 °C created zinc oxide in the form of hexagonal structure. Investigations displayed that the size of the ZnO crystallites changed by the change of milling time and temperature of calcination. Increasing the milling time (from 2 to 6 h) reduces the crystalline size (from 25 to 21.5 nm), which may show the presence of a (critical moment). Temporarily, a rise in the temperature of calcination from 400- 800 °C initiated a growth in the size of the crystalline (from 18 to 35 nm) [13]. The advantages of this mechanochemical approach are: finer particle size, higher purity of production, faster reactivity speed and different micro-reaction mechanism [40].

Sol-Gel Approach

The sol-gel preparation procedure of NPs was changed to the formation of inorganic composition along chemical reaction of a given solution. The importance of utilizing sol-gel technique is that this method produces best thermal stability ratio, best solution resistance, higher mechanical stability and the probability to the transform simulation.

Sol-gel and calcination method was used for the synthesis of zinc oxide NPs by Darroudi *et*

al. [41]. ZnO NPs formed after characterization of that crystal structure including particle size and morphology. The results revealed that good procedure situation for the preparation of ZnO NPs was predictable at 60 minutes of ultra-sonication time and pH 10. The crystal size of the created ZnO NPs was 45.350 nm, with high morphology homogeneity. The particle size of ZnO NPs is about 50 nm with a ZnO content of 87.31 percent [42]. The main advantages accompanying the sol-gel approach include lower dispensation temperatures, extraordinary levels of purity, control of dopant concentrations and the aptitude to manufacture multicomponent compositions in dissimilar product forms [43].

Hydrothermal Approach

The hydrothermal technique doesn't require using (organic solvents) or supplementary processes of grinding and calcination; so, it's an easy and environmentally friendly method. This method requires an autoclave place when the substrate combination is heated gradually to a temperature between 100 and 300 °C and left for more days. Consequently, after cooling, (crystal nuclei) are created, with an increase in size. This method has a lot of advantages; it can be applied at low temperatures and size and shape of the crystals depend on the structure of the mixture and the temperature of the process as well as on pressure. Moezzi and coworkers [42] have manufactured ZnO nanotubes synthesized by hydrothermal approach utilizing $\text{Zn}(\text{NO}_3)_2$ as a precursor. However, the outer diameter and length of the ZnO nanotubes were about 200nm and 2.4µm, respectively [44]. Advantages of the hydrothermal method over other types of nanoparticle preparation methods include the ability to create crystalline phases which are not stable at the melting point. Also, materials which have a high vapor pressure near their melting points can be grown by using the hydrothermal method [45].

Liquid Phase Approach

PLD (Pulsed laser deposition) is an amazing synthesis approach because of its capability to create NPs in a small size and a low impurity level. There are 3 famous steps to participate in the laser ablation preparation approach and create NPs in a target sunk in liquid. Yoshitak explains that the morphological phase in controlling zinc oxide crystals was aware of the simple water solution approach. Zinc oxide nanotubes were produced at (50 °C) with a

length of 50 μm and a width of around 100 nm [46].

Liquid-phase synthesis methods have several advantages over other gas-phase and solid-phase synthesis methods. Liquid phase synthesis is the most common synthesis method for preparing nanoparticles (NPs) and nanostructured materials together with gas-phase synthesis. Also, size and shape control of NPs obtained could be achieved at low temperatures within a short time ranging from minutes to hours [47].

Precipitation Control

A general way to obtain ZnO is controlled precipitation, given the fact that it makes it possible to obtain results with repeated properties. This procedure includes quick and natural reduction of ZnCl_2 solution utilizing a reducing agent, to stop the increase of particle size with the definite dimensions, through deposition of a precursor of zinc oxide in the solution. This precursor is then under the effect of thermal treatment, through milling for removal of impurities. It is too difficult for breaking collective form; consequently, the powders calcined have a higher scale of particle collection. The deposition procedure is prohibited *via* parameters like temperature, pH and deposition time. ZnO is deposited in water solutions of ZnCl_2 , ZnSO_4 and $\text{ZnC}_4\text{H}_6\text{O}_4$, where the reagent concentration controlling factors are the ratio of adding of the substrates and the reaction temperature. Zinc oxide NPs with the average size of 30 nm were found by using William-Hal approach by Sadraei *et al.* [48].

Precipitation method relies upon the precipitation of nanometer-sized particles within an incessant fluid solvent. An inorganic metal salt, such as chloride, nitride ... and so on, is dissolved in water. Metal cations exist in the form of metal hydrate species. The hydrolyzed species condense and are then washed, filtered, dried and calcined in order to obtain the final product [49].

Vapor Transport Approach

The famous approach to manufacture zinc oxide NPs is the vapor transport procedure. It is able to be clamped into a catalytic (free vapor-solid VS) procedure and a (catalyst-assisted vapor liquid solid VLS) procedure depending upon the variation in the creation mechanisms of the nanostructures. The vapor-solid procedure can generally generate a large scale of nano-

structures, such as nanorods, nanowires, nanobelts, among others. In a usual vapor-solid procedure, composite zinc oxide nanostructures like nanobelts and nanohelices were prepared by Kong *et al.* [50], establishing through synthesized NPs a belt pattern in lengths greater than hundreds of micrometer, thicknesses from 5 to 20 nm and widths from 10 to 60 nm [50]. In some processes like this, the vapor of zinc, oxygen or oxygen vapor are volatile and interact with each other, creating zinc oxide NPs. There are many ways to generate zinc and O vapor. Zinc oxide decomposition is a direct and easy approach; however, it is confined to higher temperatures [51]. From the vapor-solid procedure, the NP structure is created via contracting directly in the phase vapor. While different NP structures can be grown, this way prominently gives fewer control in the geometrical shape, arrangement and specific position of zinc oxide nanostructures. The geometrical nanobelt parameters are found to be T519 nm and W528 nm. Table 1 summarizes the different ways of zinc oxide nanostructure creation.

The vapor transport method has full advantages represented in impulsively accumulating pure one-dimensional single crystals directed by developing along the lowermost energy direction, favored orientation and least energy surface, leading to creation of low index crystallographic planes of NPs [52].

Physical Properties of Zinc Oxide Nanostructures

Zinc oxide NPs have different physical properties. It should be noted that since the dimensions of semiconductor materials are continuously reduced to a nanometer or even smaller size, several physical properties fall under the effects of changes called (quantum size effects). For instance, quantum confinement rises the energy band gap of quasi, one-dimensional (Q1D) zinc oxide, which was accepted via optical radiation [34]. It can be stated that quantum confinement is the alteration of electronic and optical characteristics once the material tested is of an adequately tiny size; characteristically 10 nm or less. The band gap rises as the dimensions of the nanostructure decrease. Explicitly, the consequence is that electrons and holes are pressed into a dimension

that is close to a critical quantum measurement, named the exciton Bohr radius [53].

Acceptance of primary physical properties is critical to the intelligible design of useful devices' properties. Investigation of specific zinc oxide NPs is required to examine their potential application as building blocks for nano-scale

view devices. This review article is going to summarize the previous research on the physical properties of zinc oxide NPs, involving magnetic properties, electrical properties, mechanical properties and properties of photoluminescence [54].

TABLE 1. Summary of ZnO NP preparation approaches.

Technique	Precursors	Synthesis conditions	Properties and uses	Ref.
Mechanochemical 1 process 2 process	$ZnCl_2$, Na_2CO_3 , NaCl	calcination: 2 h, 600 °C 400-800 °C	hexagonal structure particle diameter 21-25 nm hexagonal structure	[13] [14]
Precipitation process	$Zn(NO_3)_2$, NaOH ZnO powder, NH_4HCO_3	synthesis: 2 h; drying: 2h, 100 °C reaction: r-Z h, 25 °C; drying: 80 °C; calcination: 1 h, 350 °C	particles of spherical size of around 40 nm hexagonal wurtzite structure; flower-like and rod-like shapes (D: 15-25 nm, BET: 50- 70 m ² /g)	[15] [16]
Precipitation in the presence of surfactants	$Zn(NO_3)_2$, NaOH, SDS, TEA (trieth- anolamine)	precipitation: 50-55 min, 101 °C	wurtzite structure, rod-like shape (L: 3.6 nm, D: 400 500 nm) nut-like shape and rice-like shape, size: 1.2-1.5 µm	[17]
Sol - gel	$Zn(CH_3COO)_2$, oxalic acid, ethanol and methanol	reaction temperature: 60 °C; drying: 24 h, 80 °C; calcination: 500 °C	zincite structure; aggregate particles: ~100 nm; rod-like shape; particles L: ~500 nm, D: ~100 nm; BET: 53 m ² /g	[18]
Solvothennal hydrothermal and microwave techniques	$Zn(CH_3COO)_2$, $Zn(NO_3)_2$, LiOH, KOH, NH_4OH $ZnCl_2$, NaOH	reaction: 10-48 h, 120-250 °C reaction: 5-10 h, 100-220 °C in teflon- lined autoclave	hexagonal (wurtzite) structure, size of micro- crystallite: 100 nm - 20 µm particle morphology: bullet-like (100 - 200 nm), rod-like (100 - 200 nm), sheet (50 - 200 nm), polyhedron (200 - 400 nm), crushed stone-like (50-200 nm)	[19] [20]
Emulsion	$Zn(CH_3COO)_2$, heptane, Span- 80, NH_4OH	reaction: 1 h; aging: 2.5 h; drying: in rotary evaporator; calcination: 2 h, 700 - 1000 °C	hexagonal structure; spherical shape; particle diameter: 0.05-0.15 µm	[21]
Microemulsion	$Zn(NO_3)_2$, NaOH, heptane, hexanol, Triton X-100, PEG400	reaction: 15 h, 140 °C; drying: 60 °C	hexagonal (wurtzite) structure; particle morphology: needle-like (L: 150-200 nm, D: ~55 nm), nanocolumns (L: 80-100 nm, D: 50-80 nm), spherical (~45 nm)	[22]

Mechanical Properties of ZnO NPs

After the traditional elasticity theory, the bending coefficient was determined. Determination of the mechanical properties of the specific NPs is moderately difficult, since the classic measurement approach for bulk substances does not directly apply. Based on the resonant excitation caused by the electric field, according to Bai *et al.* [51], the bending coefficient of zinc oxide nanobelts is characterized by TEM. By this way, distinctive holder sample TEM was performed to apply an oscillating electric field between the zinc oxide nanobelt and a static electrode. This field of

electricity led the nanobelt vibration and increased resonance oscillation due to heavy frequency tuning. Based on the conventional elasticity theory, bending modulus was calculated. Zinc oxide nanobelt proves to be a capable material as nanocantilever and nanoresonator. Its size is decreased and its sensitivity improvement differs from that of (conventional cantilever) invented by micro-technology displayed in Fig. 3 [51]. Hughes *et al.* [55] stated the influence of the zinc oxide nanobelt to chosen position and length. This indicates the possibility of applying it as a very atomic force microscope (AFM) cantilever [55].

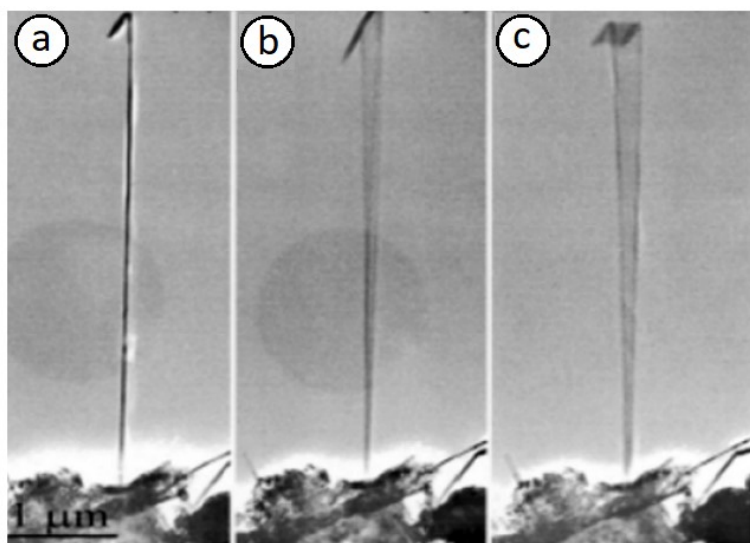


FIG. 3. A particular zinc oxide nanobelt through a curved end (a) (stationary), (b) (resonant) at (731 kHz) from the parallel plane to the looking direction and (c) (resonant) at (474 kHz) from the perpendicular plane to the looking direction [51].

Electrical Properties

The important revision of electrical properties of zinc oxide NPs is difficult to increase their applications in nano-technology. Measurement of electrical transfer has been carried out on specific nanowires and nanorods [38, 56]. Private zinc oxide nanowire was arranged as a field effect transistor through several techniques. Isopropanol alcohol was first synthesized to install a nanowire suspension system and then deposited on SiO_2 / Si material. Lithography photo has been used to characterize (contact electrode range) and (degenerately doped Si substrate) worked as a (back gate electrode). Due to population defects like (oxygen vacancy) and (zinc interstitials), zinc oxide nanowires described clearly the behavior of n-type semiconductors.

It is established that the electrical properties of zinc oxide depend on the ratio of doping ions, as found by Chu and Li [57], when they worked on the improvement of electrical properties of doped zinc oxide via electrochemical deposition. Following this, just pure zinc oxide displays the behavior of a resistive switch, indicating that defects in zinc oxide are importantly responsible for determining the behavior of a resistive switch. From Fig. 4a for pure zinc oxide, it is clear that a rapid fall of leak of current demonstrates that it has a higher resistance and is non-volatile, while according to Fig. 4b and Fig. 4c, In^{3+} and Al^{3+} are dopings to zinc oxide, which correspondingly do not display the behavior of a resistive switch. By (Al^{3+}) doping, conductivity rose and In^{3+} displayed a rectifying behavior as a current reduction upon growing voltage [57].

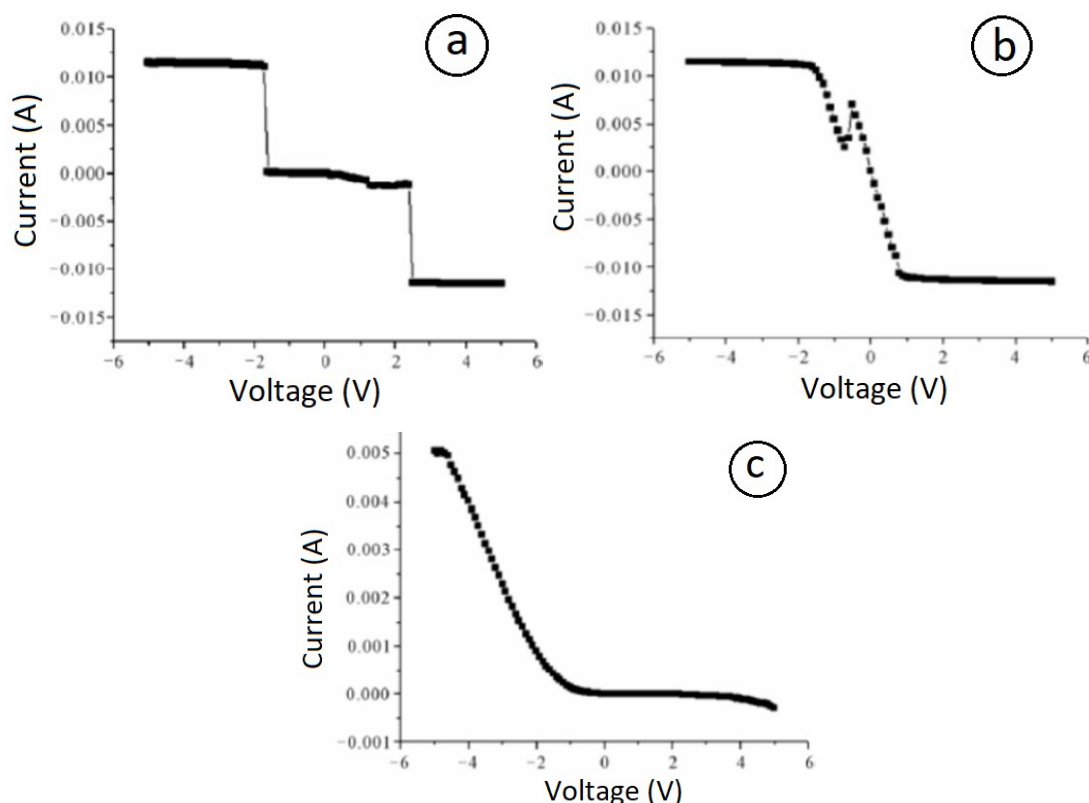


FIG. 4. I-V characteristics of (a) pure zinc oxide, (b) indium (In^{3+})-doped zinc oxide and (c) aluminum (Al^{3+})-doped zinc oxide created on the (FTO/ZnO/Pt) structure [57].

Madhuri *et al.* [58] measured the electrical properties of zinc oxide and films of rGO-ZnO measured by Madhuri *et al.* are shown in Fig. 5a. Contacts are created by utilizing an Ag paste on the films composed under (SiO_2 300 nm/Si) substrates. Currents are determined in light and dark situations by external UV illumination at $\lambda = 365$ nm. (I-V) curves of zinc oxide are rectifying (Schottky) in nature, causing metal and semiconductor contacts as shown in Fig. 5b. At -1 V bias, the current in the on state is approximately 7 times higher than in the off

state. Fig. 5c displays I-V curves acquired on (rGO-ZnO hybrid films). The curves are a little nonlinear and rGO contact with zinc oxide takes place near Schottky junctions aiding effective charge transport. Dark current of rGO-ZnO is closely 50 times higher than that of zinc oxide. The rising amount of current in the off state is caused by less film resistivity, while the existence of zinc oxide is obviously demonstrated in UV-On situation. In the two cases, we observed a linear increase in current with the voltage [58].

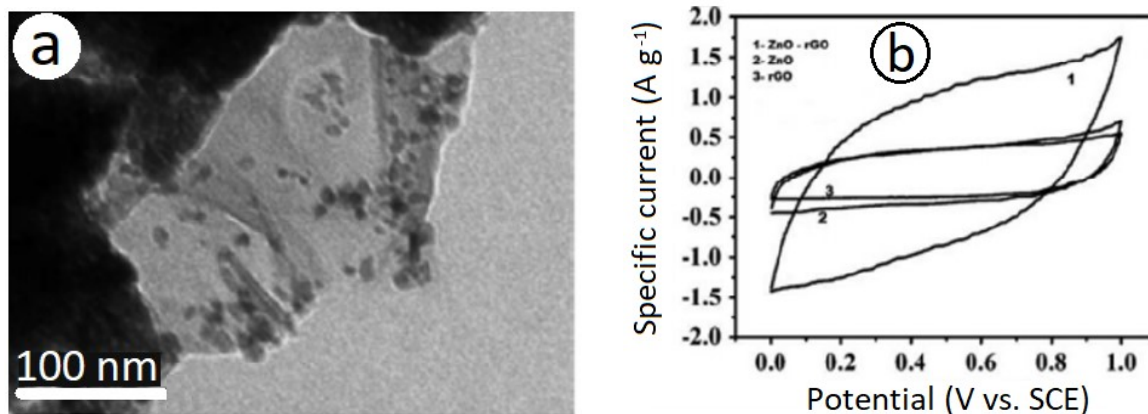


FIG. 5. (a) Circuit graphic for 2-probe measurement, (b) I-V characteristic curves of films manufactured of zinc oxide nanoparticles and (rGO-ZnO) nanoparticles on silicon dioxide by (UV illumination) [58].

Electrochemical Properties of ZnO NPs

The electrochemical properties of ZnO NP substances were studied *via* galvanic static and cyclic voltammetry (CV). Measurement of dynamic electrochemical potential is concerned with measuring the potential along the work electrode and the reference electrode *via* the current measured along the work electrode and the counter electrode. Specific capacitance was determined [59, 60] as:

$$C_s = \frac{Q}{\Delta V \times m} = \frac{I \times t}{\Delta V \times m} \quad (1)$$

where C_s : specific capacitance of the electrode, I : current through the discharge process, t : time discharge, ΔV : potential window and m : mass of active electrode substance.

Raja *et al.* [61] synthesised ZnO/rGO compound by chemical wet preparation as displayed in Fig. 6a. CV curve indicates a high

integral area of (positive synergetic effects) in a particular capacitance as displayed in Fig. 6b. Specific capacitance is about 280 F/g which is greater than that of the pure zinc oxide and (rGO) under a current density of (1 A/g) [61].

Babu *et al.* [63] perceived from electrochemical experiments that the zinc oxide/graphene nano-compound produces an elementary charge capacity of (420 mAh g⁻¹) and that the nano-compound displays a clearly enhanced cycling stability associated to simple zinc oxide causing buffer, conduction and confinement effects [63]. As in Fig. 7, Song *et al.* [62] synthesized ZnO/graphene compound utilizing *in-situ* hydrothermal preparation, with a capacitance of (300 mAh g⁻¹) after twenty-five cycles. However, the capacitance of pure zinc oxide decreased to (101 mAh g⁻¹) after the same cycles. Combination of graphene improved the cyclic stability of pure zinc oxide [62].

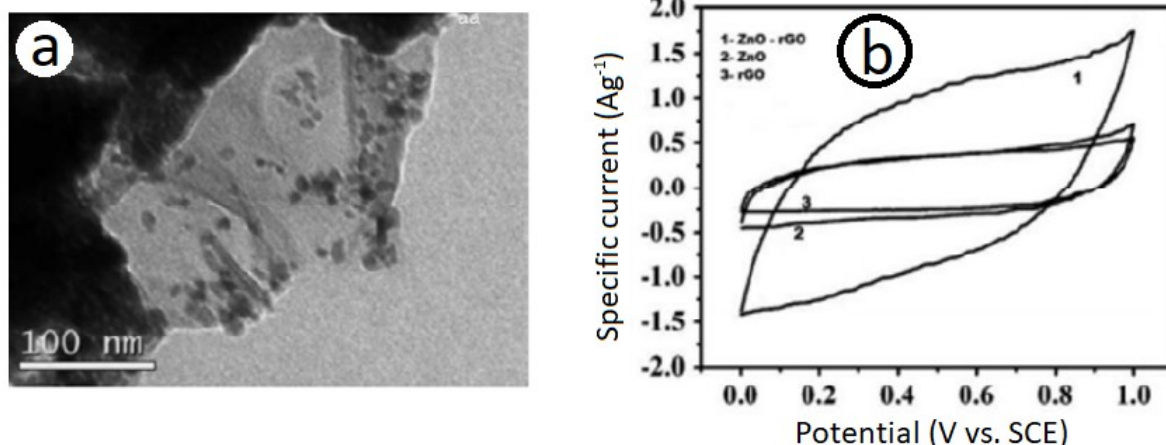


FIG. 6. (a) (ZnO/rGO) compound TEM image and (b) CV characteristics for (zinc oxide), (rGO) and (ZnO/rGO) compound as electrodes from (0.1M Na₂SO₄ electrolyte) at a sweep ratio of (5mV/s) [61].

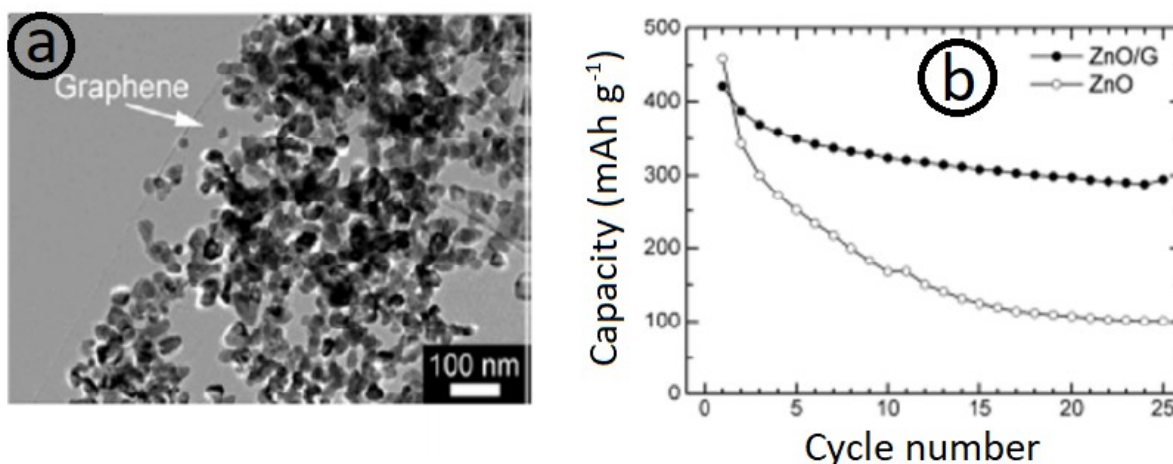


FIG. 7. (a) (ZnO/G) TEM image and (b) differences of (cycling stability) along (zinc oxide) and (ZnO/G) at (50mA g⁻¹) [62].

Luo and co-workers [64] synthesized ZnO-SnO₂ compound *via* the (electro-spinning) method and displayed enriched cyclic production at 700 °C owing to small-size particles of zinc oxide and stannic oxide as shown in Fig. 8. Through a flexible capacity of (560 mAh g⁻¹) after (100 cycles) while the compound was heated at 800 °C to 900 °C, the capacity

decreased after (100 cycles) [64]. Guler *et al.* [65] prepared ZnO-MWCNTs having a capacity of 527 mAh g⁻¹ by larger cyclic stability up to 100 cycles, as displayed in Fig. 9. This best stability is attributed to zinc oxide NP adhesion over CNT through having higher electrical conductivity, best relaxation stress and best flexibility [65].

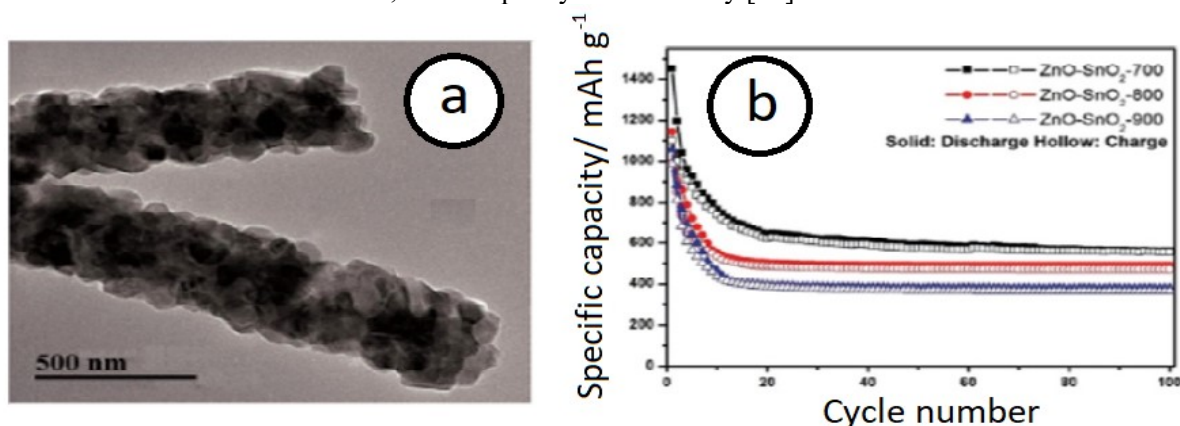


FIG. 8. (a) (ZnO-SnO₂) compound nano-fiber TEM image and (b) (cycling performance) and (Coulombic efficiencies) [64].

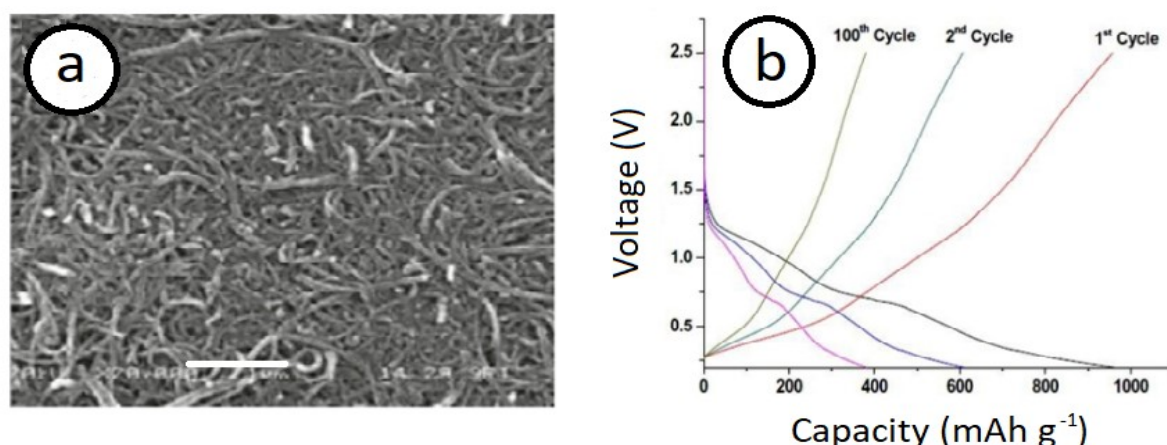


FIG. 9. (a) (SEM) and (HRTEM) images for the oxidized films from (99.99 %) of (high-purity oxygen) and Ar (99.999 %) at a rate of (a) (1:4) and (b) curves of galvanostatic charge/discharge of the oxidized films below (a) (1:4) (oxygen & argon) gas pressures [65].

Photoluminescence Properties of ZnO NPs

Photoluminescence properties of zinc oxide and nano-substance were considered by Rauwel *et al.* [66]. Zinc oxide gives the photoluminescence emission from the UV and visible ranges depending upon preparation shape, routes, deep level, size and surface defects. Once zinc oxide NPs are pooled between carbon nano-substances, surface defects are converted.

Zinc oxide permits the organization of photoluminescence properties to create as white light. Furthermore, the efficient transfer of energy in zinc oxide to the carbon nanotubes makes it suitable not just for energy gathering applications, but also as photo-detectors, biosensors and thermal imaging at low temperatures. Furthermore, it was shown that zinc oxide NP embodiment from (metal oxide matrix) creates changes in the (PL) response causing the inactivation of (surface defects) [66]. Different colors emitted by zinc oxide include: red, orange, green and blue [67].

Applications of ZnO NPs

ZnO has different chemical and physical properties. It can be used in numerous fields. Zinc oxide is important in a wide range of applications, from medicine to agriculture, from paints to chemicals and from tires to ceramics. Fig. 10 displays the universal consumption of ZnO via area [27].

Medicinal Applications

Zinc oxide NPs have certain properties that make them appropriate for applications associated with the central nervous system (CNS) and possibly with the improvement procedures of disease treatment over (mediating neuronal excitability) or (even the release of neurotransmitters). Several types of research have shown that zinc oxide influenced unlike tissues, cells or functions, as well as neural tissue engineering and biocompatibility [68].

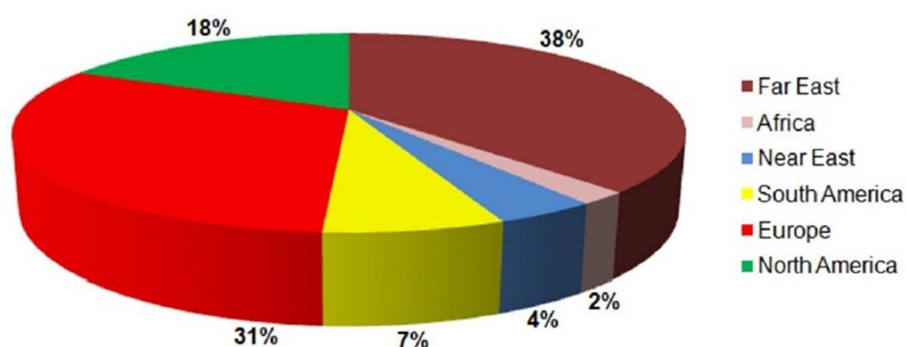


FIG. 10. Universal consumption of ZnO [27].

Agricultural Applications

ZnO NPs have potential to enhance the growth of food crops. Seeds fixed by various ZnO NP concentrations improved seed propagation, seed strength and plant growth. ZnO NPs showed to be active in growing roots stems and seeds [69]. Importance of zinc oxide NPs in biotechnology area was investigated by Paul and Ban [70]. They observed the effect of

chemically prepared ZnO NPs on the biological system. Zinc oxide is also used at different concentrations from (*Streptococcus pneumonia*, *Bacillus subtilis*, *E.Coli* and *Pseudomonas aeruginosa*). A quick rise of enzymatic activity was found through high concentrations of zinc oxide [70]. A summary of ZnO uses in different fields is shown in Fig. 11 [27].

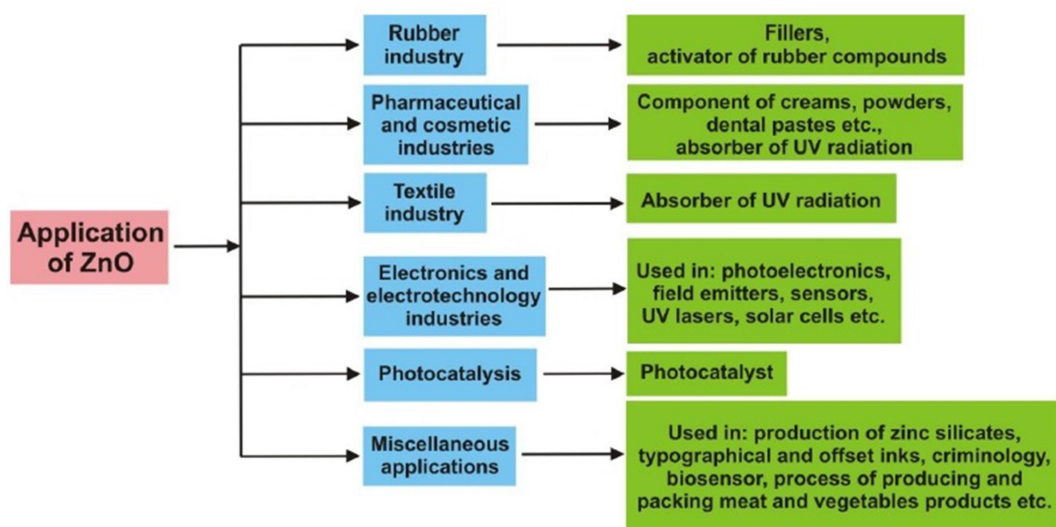


FIG. 11. Chart showing zinc oxide applications stated in the manuscript [27].

Summary

ZnO is a useful, most functional and single material with some distinguished properties; therefore, zinc oxide proposes unbelievable potential to future applications, such as electronic, magnetoelectronic and optoelectronic devices. The authors believe that this review article intensively focused on ZnO NPs from preparation, structure and application points of view. According to the assessment of studies presented here, ZnO NPs can be formed by numerous approaches. These can be alienated into metallurgical and chemical approaches. In metallurgical procedures, ZnO NPs are acquired by the burning of a suitable zinc ore, through a straight or unintended procedure.

This study indicated that zinc oxide NPs constitute building blocks in a massive range of devices and a plenty of applications. This investigation suggested that continuous effort is required to attain large arrays of structural programs for constructing recoverable architectures. Thus, attention to ZnO NPs will remain to develop and this will cause the growth of novel potentials for their request.

Acknowledgments

The authors would like to express their deep appreciations to Salahaddin University-Erbil, Kurdistan Region, Iraq, Tishk International University in Erbil and Soran Research Center for providing all of the facilities and support to complete this study.

References

- [1] Kumar, H. and Rani, R., *International Letters of Chemistry, Physics and Astronomy*, 14 (2013) 26.
- [2] Khan, I., Saeed, K. and Khan, I., *Arabian Journal of Chemistry*, 12 (7) (2019) 908.
- [3] Parihar, V., Raja, M. and Paulose, R., *Reviews on Advanced Materials Science*, 53 (2) (2018) 119.
- [4] Wang, D. et al., *Nano-Structures & Nano-Objects*, 10 (2017) 1.
- [5] Tomchenko, A.A. et al., *Sensors and Actuators B: Chemical*, 93 (1-3) (2003) 126.
- [6] Marci, G. et al., *The Journal of Physical Chemistry B*, 105 (5) (2001) 1033.
- [7] Singh, S. et al., *Nano-Structures & Nano-Objects*, 11 (2017) 1.
- [8] Serpone, N., Dondi, D. and Albin, A., *Inorganica Chimica Acta*, 360 (3) (2007) 794.
- [9] Ozgur, U., Hofstetter, D. and Morkoc, H., *Proceedings of the IEEE*, 98 (7) (2010) 1255.
- [10] Sabir, S., Arshad, M. and Chaudhari, S.K., *The Scientific World Journal*, 2014 (2014) 1.
- [11] Makarona, E. et al., *Nano-Structures & Nano-Objects*, 10 (2017) 57.
- [12] Frade, T., Jorge, M.M. and Gomes, A., *Materials Letters*, 82 (2012) 13.
- [13] Ao, W. et al., *Powder Technology*, 168 (3) (2006) 148.
- [14] Stanković, A. et al., *Journal of Materials Science*, 46 (11) (2011) 3716.
- [15] Lanje, A.S. et al., *Advanced Powder Technology*, 24 (1) (2013) 331.
- [16] Khoshhesab, Z.M., Sarfaraz, M. and Houshyar, Z., *Synthesis and Reactivity in Inorganic, Metal-Organic and Nano-Metal Chemistry*, 42 (10) (2012) 1363.
- [17] Li, P. et al., *Journal of Solid State Chemistry*, 178 (3) (2005) 855.
- [18] Mahato, T. et al., *Journal of Hazardous Materials*, 165 (1-3) (2009) 928.
- [19] Dem'Yanets, L., Li, L. and Uvarova, T., *Journal of Materials Science*, 41 (5) (2006) 1439.
- [20] Chen, D., Jiao, X. and Cheng, G., *Solid State Communications*, 113 (6) (1999) 363.
- [21] Lu, C.-H. and Yeh, C.-H., *Materials Letters*, 33 (3-4) (1997) 129.
- [22] Li, X. et al., *Journal of Colloid and Interface Science*, 333 (2) (2009) 465.
- [23] Park, J.-H. et al., *Applied Physics Letters*, 89 (12) (2006) 121108.
- [24] Fons, P. et al., *Physical Review Letters*, 96 (4) (2006) 045504.
- [25] Joseph, B. et al., *Materials Chemistry and Physics*, 58 (1) (1999) 71.
- [26] Chen, J. et al., *Applied Physics Letters*, 87 (17) (2005) 173119.
- [27] Kołodziejczak-Radzimska, A. and Jesionowski, T., *Materials*, 7 (4) (2014) 2833.
- [28] Sirelkhatim, A. et al., *Nano-Micro Letters*, 7 (3) (2015) 219.

- [29] Hahn, Y.-B., Korean Journal of Chemical Engineering, 28 (9) (2011) 1797.
- [30] Ding, Y., Zhang, F. and Wang, Z.L., Nano-Research, 6 (4) (2013) 253.
- [31] Xie, Q. et al., Solid State Communications, 136 (5) (2005) 304.
- [32] Chen, W. et al., Applied Surface Science, 253 (16) (2007) 6749.
- [33] Haq, I.U. and Azad, A.-M., Sensors, 12 (6) (2012) 8259.
- [34] Wang, Z.L., Kong, X. and Zuo, J.-M., Physical Review Letters, 91 (18) (2003) 185502.
- [35] Dulub, O., Boatner, L.A. and Diebold, U., Surface Science, 519 (3) (2002) 201.
- [36] Kabbara, H. et al., Nano-Structures & Nano-Objects, 10 (2017) 22.
- [37] Manthina, V. and Agrios, A.G., Nano-Structures & Nano-Objects, 7 (2016) 1.
- [38] Gayen, R. and Paul, R., Thin Solid Films, 605 (2016) 248.
- [39] Ghorbani, H.R., Oriental Journal of Chemistry, 30 (4) (2014) 1941.
- [40] Chen, D. et al., High-energy Ball Milling, Mechanochemical Processing of Nanopowders (2010) 149.
- [41] Darroudi, M. et al., Ceramics International, 39 (8) (2013) 9195.
- [42] Moezzi, A., McDonagh, A.M. and Cortie, M.B., Chemical Engineering Journal, 185 (2012) 1.
- [43] Fan, J., Boettcher, S.W. and Stucky, G.D., Chemistry of Materials, 18 (26) (2006) 6391.
- [44] Salahuddin, N.A., El-Kemary, M. and Ibrahim, E.M., International Journal of Scientific and Research Publications, 5 (9) (2015) 1.
- [45] Madathil, A.N.P., Vanaja, K. and Jayaraj, M., Proc. in Nanophotonic Materials IV, 66390J (2007). International Society for Optics and Photonics.
- [46] Masuda, Y., Kinoshita, N. and Koumoto, K., ISRN Nanotechnology, 2012 (2012) 1.
- [47] Sinkó, K., Szabó, G. and Zrínyi, M., Journal of Nanoscience and Nanotechnology, 11 (5) (2011) 4127.
- [48] Sadraei, R., Research & Reviews: Journal of Chemistry, 2319 (2016) 9849.
- [49] Rodriguez-Paéz, J. et al., Journal of the European Ceramic Society, 21 (7) (2001) 925.
- [50] Kong, X.Y. and Wang, Z.L., Nano-letters, 3 (12) (2003) 1625.
- [51] Bai, X. et al., Applied Physics Letters, 82 (26) (2003) 4806.
- [52] Kuo, T.-J. et al., Chemistry of Materials, 19 (21) (2007) 5143.
- [53] Roduner, E., Chemical Society Reviews, 35 (7) (2006) 583.
- [54] Kukreja, L., Barik, S. and Misra, P., Journal of Crystal Growth, 268 (3-4) (2004) 531.
- [55] Hughes, W.L. and Wang, Z.L., Applied Physics Letters, 82 (17) (2003) 2886.
- [56] Kita, K., Kyuno, K. and Toriumi, A., Applied Physics Letters, 85 (1) (2004) 52.
- [57] Chu, D. and Li, S., New Journal of Glass and Ceramics, 2 (01) (2012) 13.
- [58] Madhuri, K.P., Bramhaiah, K. and John, N.S., In: AIP Conference Proceedings, (2016), AIP Publishing.
- [59] Yong-gang, W. and Xiao-gang, Z., Electrochimica Acta, 49 (12) (2004) 1957.
- [60] Gamby, J. et al., Journal of Power Sources, 101 (1) (2001) 109.
- [61] Raja, M. et al., Fullerenes, Nanotubes and Carbon Nanostructures, 23 (8) (2015) 691.
- [62] Song, W.-T. et al., Int. J. Electrochem. Sci., 7 (3) (2012) 2164.
- [63] Babu, K.S. and Narayanan, V., Chemical Science Transactions, 2 (S1) (2013) S33.
- [64] Luo, L. et al., Ceramics International, 42 (9) (2016) 10826.
- [65] Guler, M.O. et al., Microelectronic Engineering, 118 (2014) 54.
- [66] Rauwel, P. et al., Journal of Nanomaterials, 2016 (2016) 19.
- [67] El Hichou, A. et al., Journal of Luminescence, 113 (3-4) (2005) 183.
- [68] Osmond, M.J. and McCall, M.J., Nanotoxicology, 4 (1) (2010) 15.
- [69] Prasad, T. et al., Journal of Plant Nutrition, 35 (6) (2012) 905.
- [70] Paul, S. and Ban, D.K., International Journal of Advances in Chemical Engineering and Biological Sciences (IJACEBS), 1 (1) (2014) 1.

Theoretical Simulation of Backscattering Electron Coefficient for $\text{Si}_x\text{Ge}_{1-x}/\text{Si}$ Heterostructure as a Function of Primary Electron Beam Energy and Ge Concentration

A.M.D. Assa'd and H. Kawariq

Department of Basic Sciences, Faculty of Arts and Sciences, Al-Ahliyya Amman University, Amman 19328, Jordan.

Doi : <https://doi.org/10.47011/13.2.5>

Received on: 29/09/2019;

Accepted on: 16/2/2020

Abstract: This study aims to investigate the backscattering electron coefficient for $\text{Si}_x\text{Ge}_{1-x}/\text{Si}$ heterostructure sample as a function of primary electron beam energy (0.25-20 keV) and Ge concentration in the alloy. The results obtained have several characteristics that are as follows: the first one is that the intensity of the backscattered signal above the alloy is mainly related to the average atomic number of the $\text{Si}_x\text{Ge}_{1-x}$ alloy. The second feature is that the backscattering electron coefficient line scan shows a constant value above each layer at low primary electron energies below 5 keV. However, at 5 keV and above, a peak and a dip appeared on the line scan above Si-Ge alloy and Si, respectively, close to the interfacing line. Furthermore, the shape and height of peak and dip broadening depend on the primary electron energy and incidence position with respect to the interfacing line. The last feature is that the spatial resolution of the backscattered signal at the interfacing line is improving by decreasing the primary electron energy (below 5 keV) and the shared element (Si) concentration. On the other hand, a poor compositional contrast has been shown at low primary electron energy below 5 keV. For energies above 5 keV, the spatial resolution becomes weak. These results can be explained by the behavior of the incident electrons inside the solid (interaction volume), especially at a distance close to the interfacing line and their chance to backscatter out of the sample. In general, a good compositional contrast with a high spatial resolution can be achieved at primary electron energy equal to 1 keV.

Keywords: Monte Carlo model, Backscattering electron coefficient, Si-Ge/Si, Elastic scattering, Spatial resolution, Compositional contrast.

Introduction

The development on the field emission source in getting a small probe size at low electron energies in SEM has improved the spatial resolution in the topographic contrast and reduced the charging and radiation damage of biological and semiconductor samples [1-5]. Using SEM for nano-scale sample imaging becomes recently one of the most important challenges [1, 6]. The images on SEM are produced by collecting either the backscattered

electrons (BSEs) or secondary electrons (SEs). The image contrast in SEM is normally related to backscattering electron coefficient (η) and secondary electron yield (δ) which are functions of the target atomic number (Z), incident electron beam energy (E_p) and angle of incidence (θ). Conventionally, secondary electron yield (δ) is defined as the ratio of the number of the electrons escaping with energies below 50 eV to the number of the primary electrons. These secondary electrons are mainly generated as a

result of inelastic scattering between the primary electrons and the outer shell electrons of the target atoms. The collected secondary electrons are those electrons that escaped from the few nanometers depth beneath the surface [1, 2]. The backscattering electron coefficient (η) is defined as the ratio of the number of electrons that exit the surface with energy greater than 50 eV to the number of primary electrons impinging on the surface. The choice of the 50 eV value is purely arbitrary and historical. The secondary electrons with energy higher than 50 eV are produced as a result of electron beam–solid interaction. The number of these secondary electrons is rather small in comparison with the backscattered electrons and can be safely neglected [7]. BSE signals are normally used for the compositional contrast and elemental distribution, while SE signals are used for topographical contrast [1, 2]. Several experimental works have been conducted in order to provide accurate data for η and δ [7-14].

This paper presents the results of the Monte Carlo simulation of the backscattering electron coefficient for $\text{Si}_x\text{Ge}_{1-x}/\text{Si}$ heterostructure as a function of primary electron beam energy (0.25-20 keV) and Ge concentration using CASINO model [15]. The counted backscattered electrons are those primary electrons that escaped from the surface with energy above 50 eV. Si-Ge alloys are widely used in semiconductor industry [16]. Si-Ge alloys with different fractions of Ge (1-x) are used in MOSFETs as stressors to introduce strain into Si and Ge channels. This is due to the lattice constant of Si-Ge alloys which is different from that of Si and Ge and is easily controlled by the fraction of Ge [17]. The mechanical strength of the alloy becomes temperature-insensitive at elevated temperatures depending on the alloy composition [18]. Understanding electron-solid interaction is important for surface analysis in many technological applications. For example, in Scanning Electron Microscopy (SEM), this can help significantly improve the image quality in terms of contrast and spatial resolution. When analyzing insulator targets, sample charging phenomenon can have adverse effects on the resulting image to a certain extent. Another point concerns the obtaining of a good contrast between different objects, which depends on such quantities as, for example, the incident energy of the electron beam and the attenuation coefficient in different parts of the investigated target [1, 2]. The right choice of different

experimental parameters may significantly improve the resulting images. However, sometimes, there is no possibility to check all of them in one experiment (this can be time- and money-consuming). Therefore, the use of theoretical simulation can help predict the resulting image quality. One of the widely used approaches is the Monte Carlo simulation model which allows to take many different effects and parameters into account [19-25]. The result of such a simulation strongly depends on input parameters, such as electron scattering characteristics. The authors used the Mott elastic cross-sections to describe elastic scattering of electrons in solid which is indeed among the most reliable data [26]. The primary electron energy loss due to inelastic scattering has been calculated by applying the semi-empirical equation of Joy and Lui [27]. This equation is proved to be simple and accurate as it was applied in a wide range of primary electron energies, especially low electron energies. The primary electrons on one side of the target start penetrating and interacting with the target atoms until losing their energy (which becomes less than 50 eV), backscatter from the surface to vacuum or penetrate the interfacing line toward the next layer of the target. The interfacing line is considered as a surface of the penetrated layer. Hence, the electrons penetrating the interfacing line keep scattering inside the new layer until they backscatter to the old layer, backscatter to the vacuum from the target surface as backscattered electrons or lose all of their energy (minimum $E_p = 50$ eV).

Results and Discussion

Fig. 1 shows the simulation geometry of the present theoretical study and the corresponding profile of the volume of electron-solid interaction. The interaction volume is the place where the incident electrons are scattered (elastic and inelastic) with the solid atoms. Fig. 2 shows the interaction volume for Si and Ge layers at $E_p = 5, 10$ and 20 keV. It is clear that the incident electrons penetrating a target are broadened from the incidence position. The size and shape of the interaction volume are depending on the primary electron energy (E_p) and the characteristic parameters of the target material (average atomic number (Z_{avr}), atomic mass number (A) and density (ρ)) [1, 2, 28]. Generally, the interaction volume inside the Ge layer is smaller than that in the Si layer, since the

atomic number of Ge is larger than that of Si. Thus, the incident electrons have a small range inside the Ge layer. This keeps them interacting with the Ge atoms close to the layer surface and gives the incident electrons a chance to backscatter to vacuum with a small loss of their primary energy. In the case of Si layer, the incident electrons will penetrate deeper and spread wider than those electrons that penetrate the Ge layer. The incident electrons will also suffer a large amount of energy loss inside the Si layer more than inside the Ge layer. Fig. 2 shows

that as the incident electron energy increases, the interaction volume depth (R) and radius (r) increase [29]. Generally, the interaction volume of the incident electrons in the Si-Ge alloy with different Ge concentrations is smaller than in the pure Si side for the entire E_p range. This is due to that Z_{avr} of the Si-Ge alloy is larger than that of the Si layer. Therefore, the incident electrons in the alloy have a larger chance to reach the surface and be backscattered to vacuum after penetrating and scattering with the alloy atoms than those incident on the pure Si side.

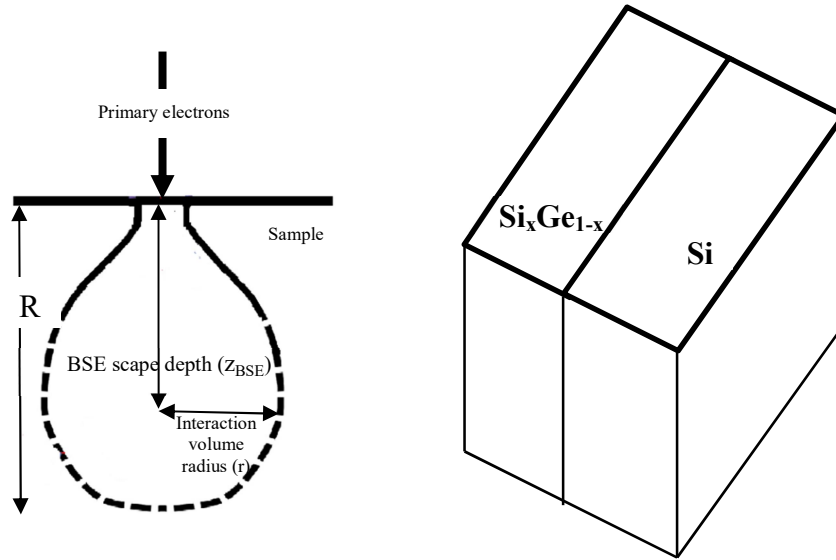


FIG. 1. Schematic diagram of the interaction volume of electron-solid interaction showing the BSE escape depth (Z_{BSE}) and the interaction volume radius (r).

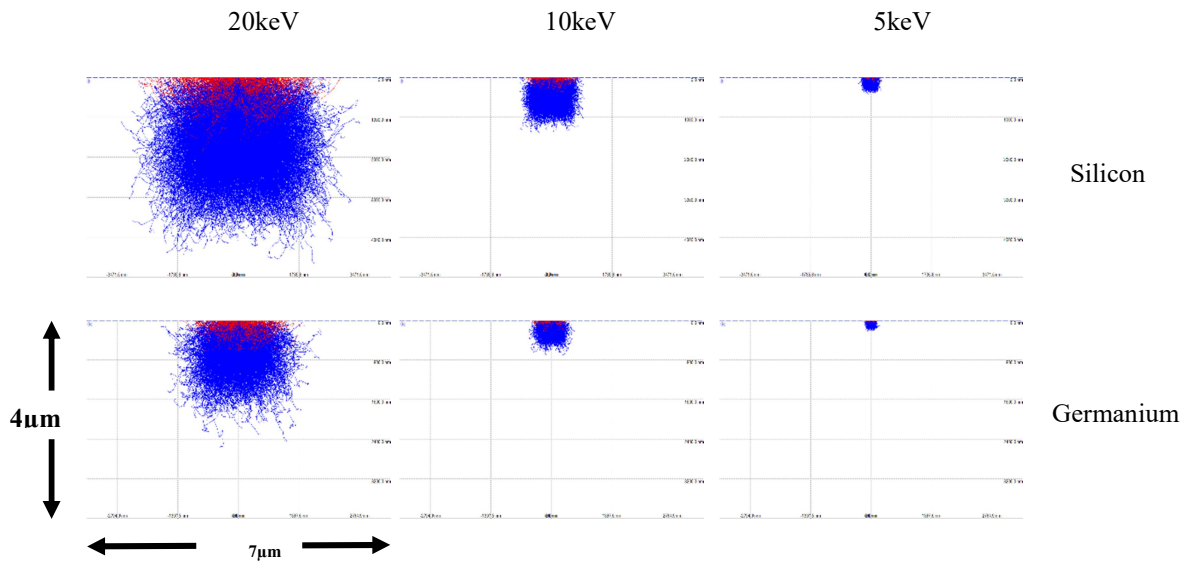
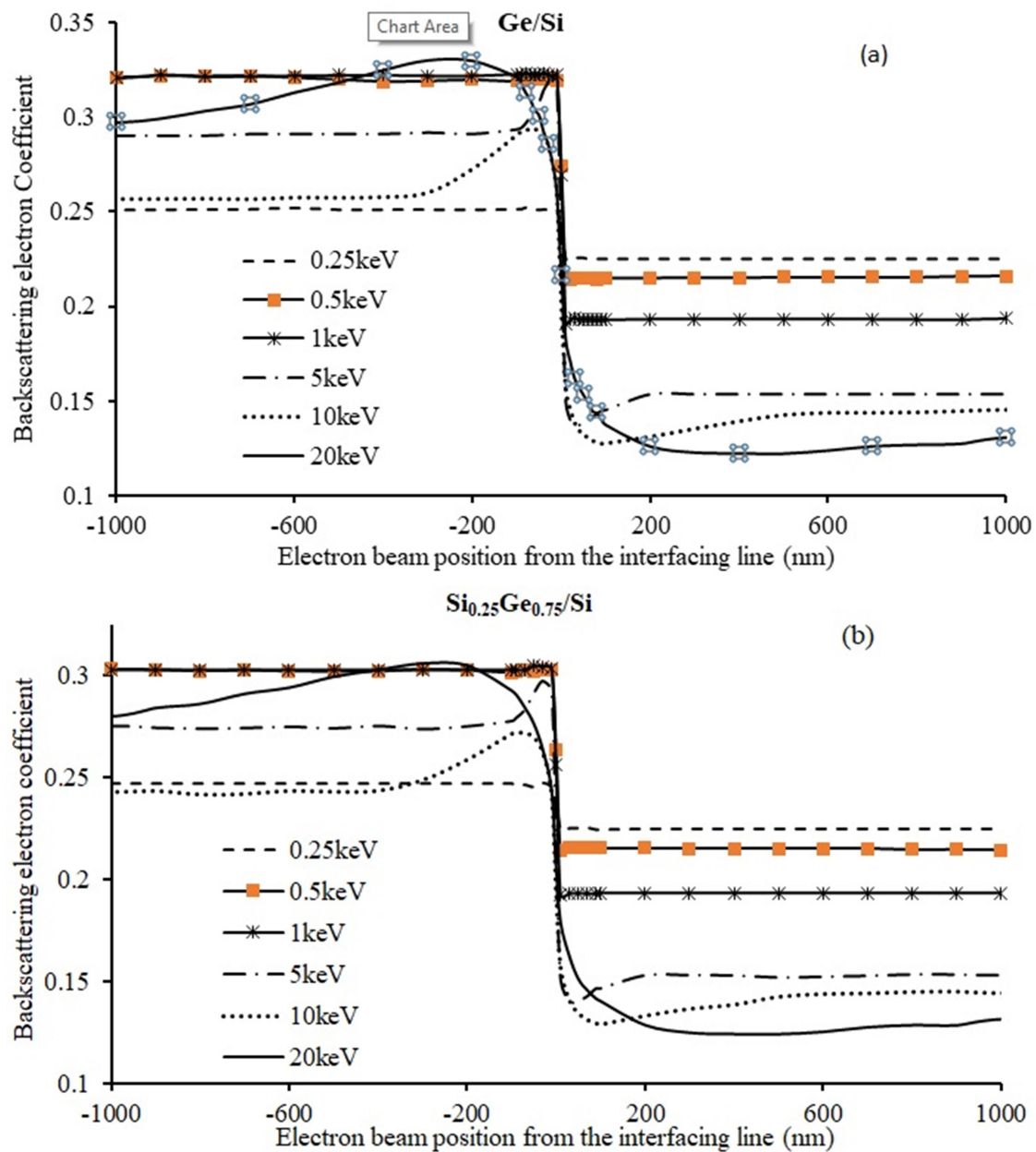


FIG. 2. Monte Carlo simulations of electron-solid interaction for Si and Ge at $E_p = 5$ keV, 10 keV and 20 keV.

In the case of micro-scale dimensions where the sample structure width is above 400 nm, η line scan has been calculated for different Ge concentrations as a function of E_p , as shown in Fig. 3. Fig. 4 also shows η line scan of different E_p values as a function of Ge concentration on $\text{Si}_x\text{Ge}_{1-x}$ alloy. The results show that the signal intensity above the alloy is higher than that above the Si side. The results also show that η above the Si-Ge alloy depends on the Ge concentration [30]. This is mainly because Z_{avr} is increasing as the Ge concentration increases. A peak above the alloy side and a dip above the pure Si side have been shown in the line scan around the interfacing line at primary electron energies of 5 keV and above; Fig. 4 (c, b, e). The

position, height and sharpness of the peak and the width of the dip are directly depending on Z_{avr} of the alloy, E_p and the beam incidence position from the interfacing line. These artefacts have been also observed in separate studies [31, 32], where the edge effect on η and the backscattered Auger signals have been investigated. The dip in the signal was explained due to the edge shadowing effect, whereas the peak was due to the increase in the escape probability of the incident electron from the edge side. Hence, the artefacts shown in the present results could be explained by studying the behavior of the incident electrons inside the sample close to the interfacing line.



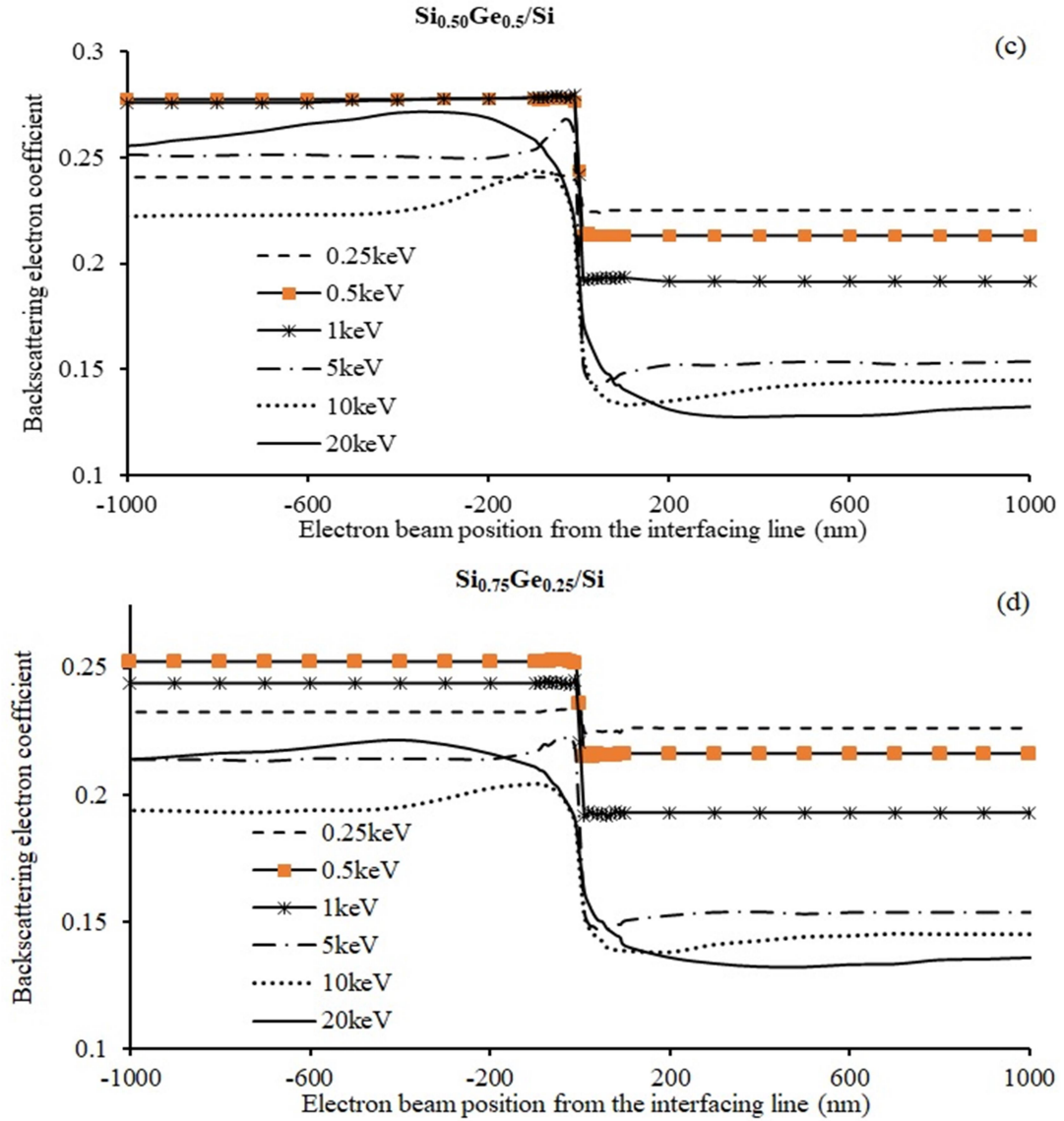
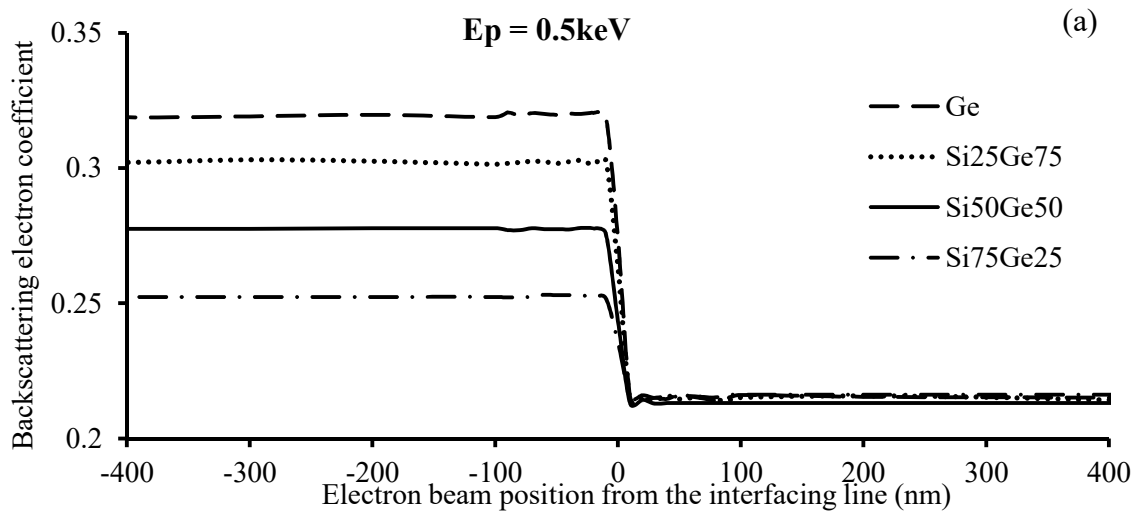
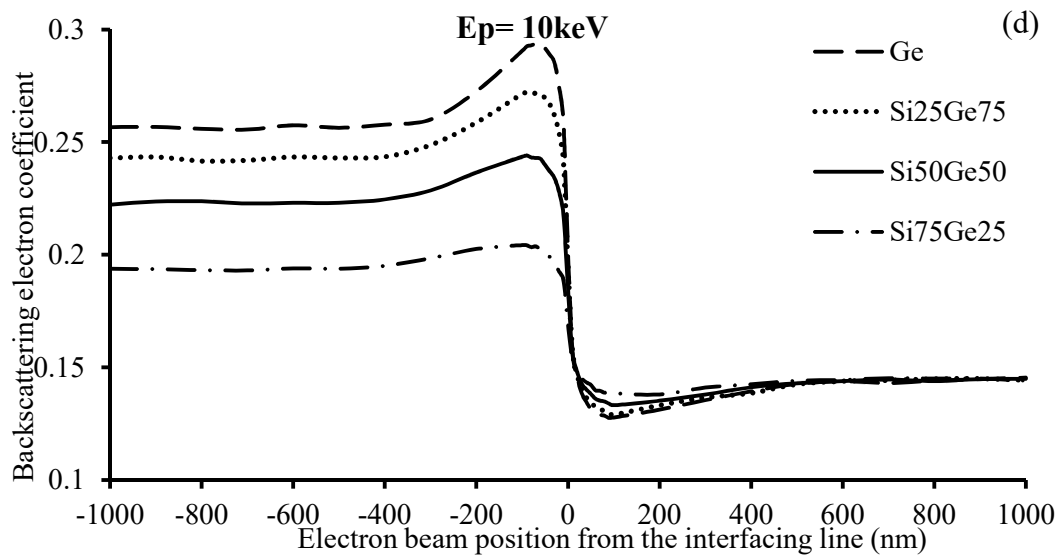
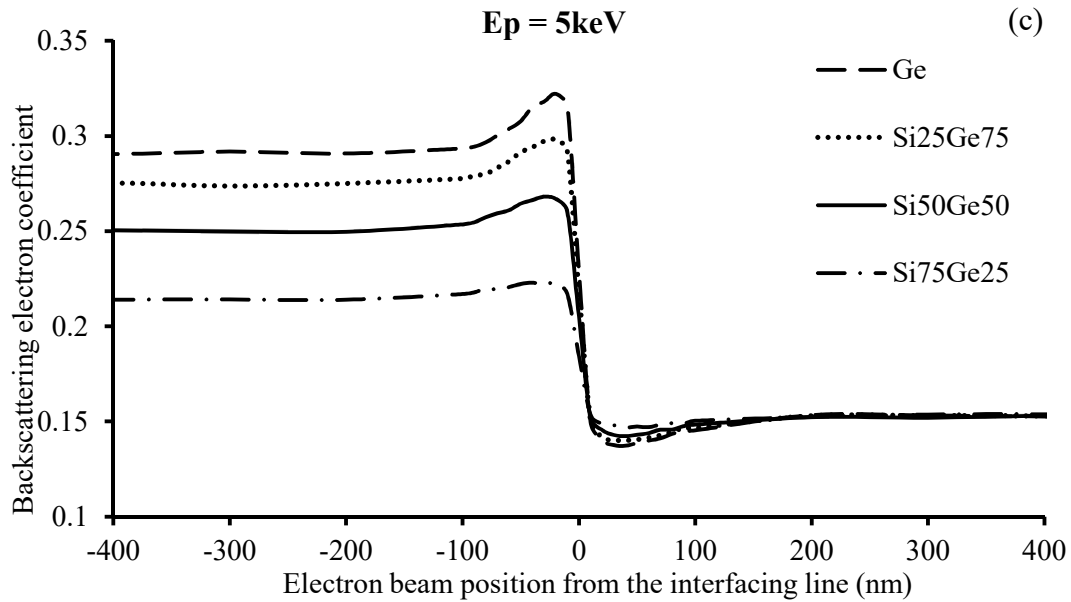
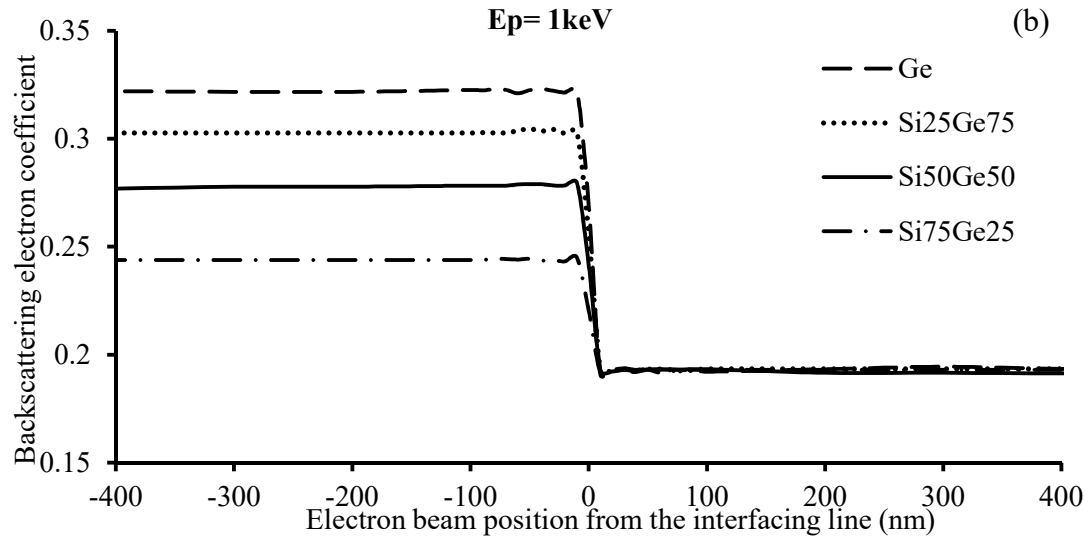


FIG. 3. Backscattering electron coefficient line scan as a function of primary electron energy for different x concentrations of $\text{Si}_x\text{Ge}_{1-x}/\text{Si}$ alloy.





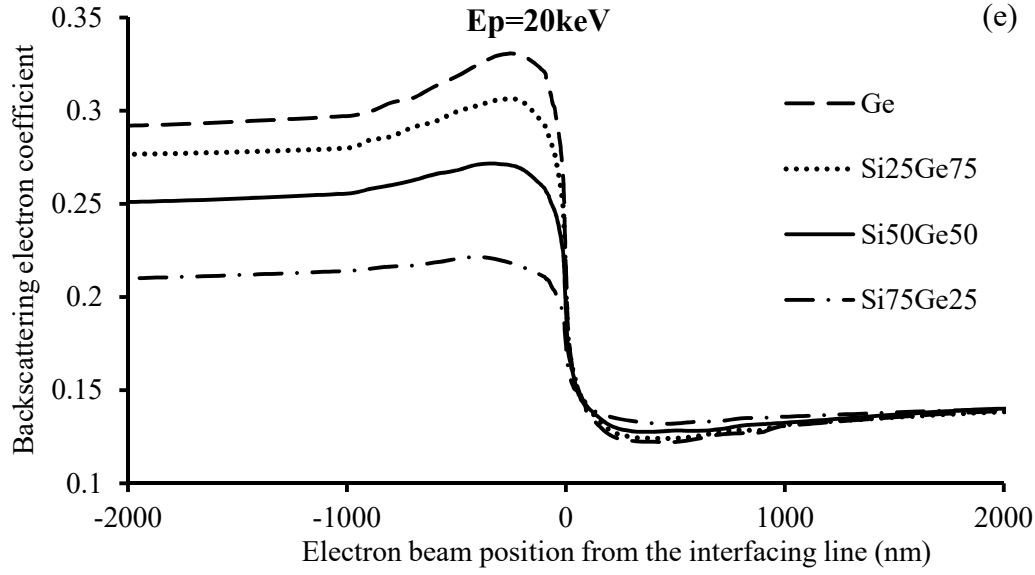


FIG. 4. Backscattering electron coefficient line scan as a function of x concentration of $\text{Si}_x\text{Ge}_{1-x}/\text{Si}$ at different primary electron energies ($E_p = 0.5\text{-}20$ keV).

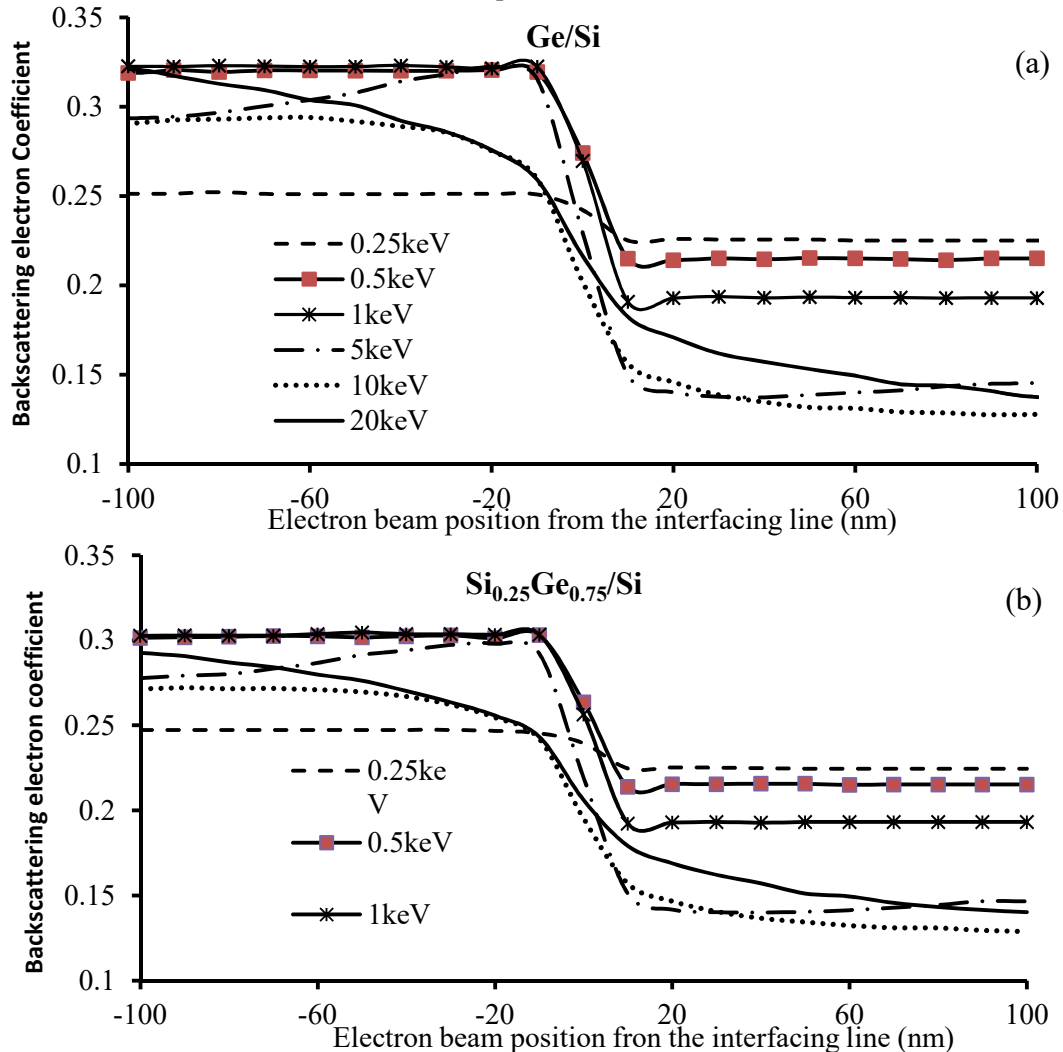
For $E_p \leq 1$ keV, the backscattering electron coefficient (η) line scan with a sharp step above the interfacing line can be observed for all Ge concentrations; Fig. 4 (a, b). This gives an indication that η data is reflected only from the primary electrons incident on the sample. This means that the interaction volume did not spread away from the incidence position. The latter is reflected on having a good spatial resolution for all x concentrations of $\text{Si}_x\text{Ge}_{1-x}$ alloy at low E_p . On the contrary, a compositional contrast between the Si-Ge alloy and Si reduces as E_p decreases (at $E_p = 0.25\text{keV}$) and the Ge concentration decreases; Fig. 3. This is because η values for the alloy and the Si layer become close to each other. In other words, the material contrast is no more proportional to the atomic number at primary electron energies below 0.5 keV [1, 7, 13]. As E_p increases above 1 keV, the compositional contrast improved while the spatial resolution reduced; Fig. 4 (c, d, e). This is due to the appearance of the peak above the Si-Ge alloy and the dip above the Si side. Also, the spatial resolution decreases as E_p increases and the Ge concentration decreases in the alloy. This appears in the increment in the distance between the peak and the dip. The reasons of having a peak and a dip above the Si-Ge alloy and Si, respectively, could be explained through the backscattered electron escape depth (z_{BSE}) and the interaction volume radius (r) of the primary electrons in the solid. When the primary electrons impinge on the Si-Ge alloy side at a

distance from the interfacing line smaller than the radius (r) of the interaction volume, many of these electrons will reach the Si layer through the interfacing line. And because of their small depth which is close to the surface and the sufficient energy in addition to their large mean free path length in the Si layer, these electrons could find their way to the vacuum through the Si surface. As E_p increases and Ge concentration decreases, the peak height decreases and becomes wider and shifting way from the interfacing line; Fig. 4. The reduction in η values is due to the reduction in the average atomic number (Z_{avr}) of the Si-Ge alloy as a result of the reduction in Ge concentration. The broadening in the peak is due to the increase in the mean free path length of the primary electrons in the alloy, which reflects on the increase of z_{BSE} and r . Hence, the interaction volume will cover part of the Si layer while the primary electrons are incident on the Si-Ge alloy at a long distance from the interfacing line. This means that as the Ge concentration decreases and E_p increases, more primary electrons can find their way to the vacuum through the Si side. The results also show that the peak appears on the line scan when the ratio of the incident position from the interfacing line to the interaction volume radius (r) is around 70% for all Ge concentrations and E_p .

In the case where primary electrons are incident on the Si side, a dip in the backscattering electron line scan is observed; Figs. 3 and 4. This is clear when the distance between the incidence position and the interfacing line is less than the interaction volume radius (r). This is due to the large depth of the interaction volume from the surface. When some electrons pass the interfacing line toward the Si-Ge alloy, they stay and interact with the alloy materials at a large depth from the alloy surface. Because of the small mean free path length of primary electrons inside the Si-Ge alloy, these electrons will not backscatter to the vacuum from this large depth where they entered the alloy from the Si side. Even though some of these primary electrons could be scattered back toward the Si side, this would occur with no enough energy that allows them to reach the surface. So, the Si-Ge alloy prevents the primary electrons that entered the alloy from reaching the surface and being backscattered to the vacuum. As E_p and Ge concentration increase, the dip

width increases and becomes deeper; Fig. 4. This is due to the large escape depth of the primary electrons in the Si side, as explained above.

Fig. 5 shows the backscattering electron coefficient (η) line scan for $\text{Si}_x\text{Ge}_{1-x}/\text{Si}$ with different x concentrations and E_p values at nano-scale dimensions (± 100 nm around the interfacing line). It is clear that there are several features that can be observed. At $E_p = 0.5$ and 1 keV, the compositional contrast between the two sides of the sample around the interfacing line is clear. However, at $E_p = 5$ keV, a wide peak appears above the alloy. At $E_p = 10$ keV and 20 keV, the compositional contrast becomes weaker, since the backscattering coefficient (η) increases above the alloy as the incidence position of the primary electron moves away from the interfacing line, while it decreases above the Si side. This shows that at $E_p = 0.5$ keV and 1 keV, a good spatial resolution and a compositional contrast can be obtained for all Ge concentrations in Si-Ge alloy.



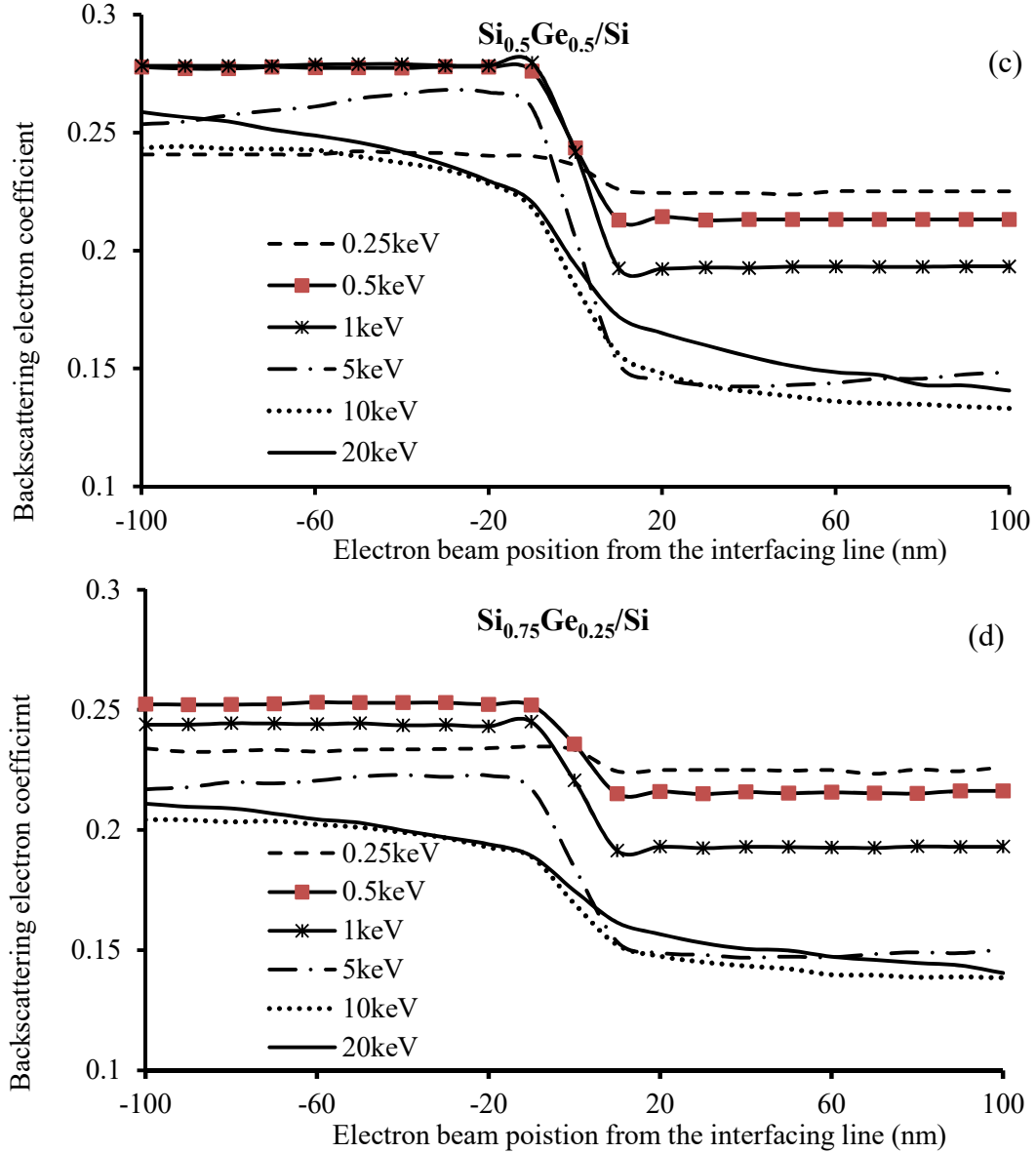


FIG. 5. Backscattering electron coefficient line scan as a function of primary electron energy for different x concentrations of $\text{Si}_x\text{Ge}_{1-x}/\text{Si}$ alloy at nano-scale dimensions ($\pm 100\text{nm}$ width around the interfacing line).

Conclusion

The Monte Carlo model is used in the present study in order to provide a better understanding of the artefacts shown in the backscattered electron signals obtained as a result of the interaction between the primary electrons and $\text{Si}_x\text{Ge}_{1-x}/\text{Si}$ heterostructure sample with different x concentrations and primary electron energies. The results show the effect of Ge concentration of the alloy and that of the primary electron energy on the compositional and spatial resolution of the backscattered signal. A good compositional contrast and spatial resolution in

SEM imaging could be obtained at low primary electron energies of 0.5 keV and 1 keV. At higher primary electron energies (above 1 keV), a peak and a dip have been shown in the backscattering electron coefficient, which affected the spatial resolution and the compositional contrast.

Acknowledgement

This work was supported by Al-Ahliyya Amman University Project No. 1/20/2018-2019.

References

- [1] Reimer, L., "Scanning Electron Microscopy, Physics of Image Formation and Microanalysis". (Springer, Berlin, Germany 1985).
- [2] Goldstein, G.I., Newbury, D.E., Echlin, P., Joy, D.C., Fiori, C. and Lifshin, E., "Scanning Electron Microscopy and X-ray Microanalysis". (New York, Plenum Press, 1981).
- [3] Jayakody, G.H., Wells, T.R.C. and El-Gomati, M.M., *Journal of Electron Spectroscopy and Related Phenomena*, 143 (2005) 2.
- [4] El-Gomati, M.M., Zaggout, F., Jayakody, H., Tear, S. and Wilson, K., *Surface and Interface Analysis*, 37 (11) (2005) 901.
- [5] Wuhterm, R. and Moran, K., *I.O.P Conf. Ser. Mater. Sci. Eng.*, 109 (2016) 1.
- [6] Vida-Simit, I., Jumate, N., Chicinas, I. and Batin, G., *Rom. Journ. Phys.*, 49 (9-10) (2004) 955.
- [7] El-Gomati, M.M., Walker C.G.H., Assa'd, A.M.D. and Zadrazil, M., *Scanning*, 30 (2008) 2.
- [8] Bronstein, I.M. and Fraiman, B.S. "Vtorichnaya Elektronnaya Emissiya", *Secondary Electron Emission*, (Nauka-Moskva, 1969).
- [9] Assad, A.M.D. and El-Gomati, M.M., *Scanning Microscopy*, 12 (1998) 185.
- [10] Joy, D.C. "A Database of electron solid interactions", Revision [04-02], (2006); <http://web.utk.edu/~srcutk/htm/interact.htm>.
- [11] Walker, C.G.H., El-Gomati, M.M., Assa'd, A.M.D. and Zadrazil, M., *Scanning*, 30 (2008) 365.
- [12] Liu, S., Liu, Y., Wang, P., Liu, W., Pei, G., Zeng, L. and Sun, X., *Review of Scientific Instruments*, 89 (2018) 023303
- [13] Hashimoto, Y., Muto, A., Woods, E., Walters, T. and Joy, D.C., *Microscopy Today*, May (2015) 20.
- [14] Suria, A., Prattb, A., Tear, S., Walker, W., Kincal, C., Kamber, U., Gurlud, O. and El-Gomati, M., *J. of Electron Spectroscopy and Related Phenomena* (2019), in press, <https://doi.org/10.1016/j.elspec.2019.02.002>.
- [15] Demers, H., Poirier-Demers, N., Couture, A.R., Joly, D., Guilmain, M., Jonge, N. and Drouin, D., *Scanning*, 33 (2011) 135.
- [16] Mastronardi, L., Banakar, M., Khokhar, A.Z., Hattasan, N., Rutirawut, T., Domínguez, Bucio, T., Grabska, K.M., Littlejohns, C., Bazin, A., Mashanovich, G. and Gardes, F.Y., *Optical Express*, 26 (6) (2018) 6663.
- [17] Takagi, S., "Silicon–Germanium (Si-Ge) Nanostructures (Production, Properties and Applications in Electronics)", (Woodhead Publishing Series in Electronic and Optical Materials, 2011), pp. 499–527.
- [18] Yonenaga, I., "Six Ge_{1-x} Bulk Crystals, Encyclopedia of Materials: Science and Technology", 2nd Ed. (Elsevier, 2003) pp. 8647-8651.
- [19] Bishop, H.E., *Proc. Phys. Soc.*, 85 (1965) 855.
- [20] Joy, D.C., *Journal of Microscopy*, 147 (1987) 51.
- [21] Yan, H., El-Gomati, M.M., Prutton, M., Wilkinson, D.K., Chu, D.P. et al., *Scanning*, 20 (1998) 465.
- [22] Salvat, F., Fernandez-Varea, J.M. and Sempau, J., In: *PENELOPE-2006 Workshop Proceedings*, Barcelona, Spain 4–7 July (2006).
- [23] Drouin, D., Couture, A.R., Joly, D.C., Tastet, X., Vincent, A. and Gauvin, R.M. *Scanning*, 29 (2007) 92.
- [24] Soref, R., *IEEE J. Sel. Top. Quantum Electron.*, 12 (6) (2006) 1678.
- [25] Gauvin, R., Lifshin, E., Demers, H., Horny, P. and Campbell, H., *Microsc. Microanal.*, 12 (2006) 49.
- [26] Mott, N.F. and Massey, H.S.W. "Theory of Atomic Collisions". (Oxford University Press, London, 1965).
- [27] Joy, D.C. and Luo, S., *Scanning*, 11 (1989) 176.
- [28] Lukiyanov, F.A., Rau, E.I. and Sennov, R.A., *Bulletin of the Russian Academy of Sciences: Physics*, 73 (4) (2009) 441.

- [29] Müllerová, I., Frank, L., Mikmeková, Š. and Mikmeková, E.M., *Microscopy and Microanalysis*, 25 (S2) (2019) 472.
- [30] Ajmal Khana, M., Algarnia, H., Bouarissac, N., Al-Hagana, O.A. and Alhuwaymeld, T.F., *Ultramicroscopy*, 195 (2018) 53.
- [31] El-Gomati, M.M. and Assa'd, A.M.D., "Modern Developments and Applications in Microbeam Analysis", (Springer, Vienna, 1998), p. 333.
- [32] Assa'd, A.M.D. and El-Gomati, M.M., *Ultramicroscopy*, 79 (1999) 1.

From Amorphous Red Phosphorus to a Few Layers of Black Phosphorus: A Low-cost and Efficient Preparation Process

G. Tiouitchi^{a,b}, F. ElManjli^{b,c}, O. Mounkachi^a, A. Mahmoud^d, F. Boschini^e,
A. Kara^e, H. Oughaddou^{f,g}, M. Hamedoun^b, A. Benyoussef^{b,h} and
M. Ait Ali^c

^a LaMCScI, B.P. 1014, Faculty of Science-Mohammed V University, Rabat, Morocco.

^b Materials and Nanomaterials Center, MAScIR Foundation, Rabat Design Center, Rue Mohamed Al Jazouli, Madinat Al Irfane, Rabat 10 100, Morocco.

^c Coordination Chemistry Laboratory, Cadi Ayyad University, Faculty of Sciences Semlalia (UCA-FSSM), B.P. 2390 - 40000 Marrakech, Morocco.

^d Greenmat, Cesam, Institute of Chemistry B6, University of Liege, 4000 Liège, Belgium.

^e Department of Physics, University of Central Florida, Orlando, Florida 32816, USA.

^f Institut des Sciences Moléculaires d'Orsay, ISMO-CNRS, Bât. 210, Université Paris-Sud, 91405 Orsay, France.

^g Département de Physique, Université de Cergy-Pontoise, 95031 Cergy-Pontoise Cedex, France.

^h Hassan II Academy of Science and Technology, Rabat, Morocco.

Doi : <https://doi.org/10.47011/13.2.6>

Received on: 08/08/2019;

Accepted on: 16/12/2019

Abstract: In this work, we present an efficiency synthesis method of phosphorene from red phosphorus by means of black phosphorus. The latter was synthesized by using copper, tin, tin iodide and red phosphorus as precursor at low pressure-temperature. Characterizations with powder X-ray diffraction, scanning electron microscopy (SEM), energy dispersive spectrometry (EDX), high-resolution TEM (HR-TEM) and Raman spectroscopy were performed to confirm the high quality and purity of black phosphorus crystal. Liquid phase method was used to exfoliate black phosphorus to phosphorene in N-methyl-2-pyrrolidone (NMP) as solvent. Atomic force microscopy and STEM were used to confirm the exfoliation of black phosphorus in a few layers of phosphorene.

Keywords: 2D materials, Red phosphorus, Black phosphorus, Phosphorene, Liquid-phase exfoliation.

Introduction

Black phosphorus (BP), the most stable form of phosphorus, is a 2D material expected to have potential applications [1], such as in nanocomposites [2], photovoltaics [3] and batteries [4]. While graphene (the 2D derivative of graphite) suffers from zero band gap [5] and molybdenite (MoS₂) suffers from the low mobility of its charge carriers [6], BP presents itself as a very promising material for the

electronics and energy market, due to its high mobility of charge and direct gap (from 0.3 to 1.5 eV as a function of its thickness) [7]. Black phosphorus can be prepared by several methods, such as high-pressure synthesis [8,9], recrystallization from Bi [10,11] or Hg [12] and melting and annealing sequence at high temperatures [12,13]. All these methods often lead to small crystals with limited crystallinity, take a long time and in some cases even involve

toxic chemicals. In 2007, S. Lange et al. [14] synthesized black phosphorus from red phosphorus at low pressure and 873 K by adding small quantities of Au-catalyst, tin and tin (IV) iodide in a silica tube sealed under vacuum. This method produces several secondary phases in the final product, difficult to be eliminated. Thus, the development of a safe and simple method allowing to obtain black phosphorus with high crystallinity remains one of the present challenges preventing the use of black phosphorus and phosphorene for industrial applications. We have recently developed a modified method based on the choice of a cheap, abundant and non-toxic catalyst (Cu) to synthesize black phosphorus with high quality [15]. The main objective of the present work is the optimization of BP synthesis conditions using copper as catalyst and its liquid exfoliation in N-methyl-2-pyrrolidone (NMP) to produce dispersible BP flakes with controllable size and thickness, as well as in high yield.

Experimental

Black phosphorus was synthesized from amorphous red phosphorus (RP) by using Cu, Sn and SnI₄. The mineralizing SnI₄ was synthesized by adding 0.5g of Sn (Chempur, 99.999%) and 2.0g of I₂ (Chempur, 99.8%) to a solution of 25 mL of glacial acetic acid and 25 ml of acetic anhydride. The suspension was heated to reflux until the solution turned orange, indicating the completion of the reaction. After cooling, the crude product, crystallized as an orange solid, was filtered and further purified by recrystallization in hot chloroform. Black phosphorus was prepared as follows: Cu (22.7mg), Sn (42.5mg), red phosphorus (155.2mg) and SnI₄ (10.0 mg) (molar ratio 1:1:14:0.045) were transferred into a silica glass ampoule, 10 cm in length, with an inner diameter of 1.0 cm and a wall thickness of 0.25 cm. The ampoule was sealed under vacuum placed horizontally in an oven and heated at 923K for 4 hours. The solid mixture was located in the hot end of the oven. The reaction was cooled to RT over a period of 72 hours with a slow rate of 0.2°C/min, which allows for better crystal growth. The product is formed in the cold section of the ampoule. The excess of SnI₄ was removed by refluxing the mixture in toluene several times until the toluene remains clear (ultrasonic bath 20–45 min). No traces of other elements were observed in the final product.

The free layers of black phosphorus (i.e., phosphorene) were obtained by liquid-phase exfoliation (LPE) method [16,17]. Black phosphorus was exfoliated in N-methyl-2-pyrrolidone (NMP) (1mg/ml) using a bath ultrasonication (VWR - USC 600 THD (45 Hz)) for 8 hours. Similar to mechanical exfoliation, liquid-phase exfoliation cannot produce 2D materials with uniform size and thickness. To get layers with uniform size and thickness, an additional centrifugation step is required. For each speed of centrifugation, the supernatant was then further centrifuged at a high speed up to 13000 rpm (MC Medline 20000). The crystalline structure of the synthesized samples was analyzed by powder X-ray diffraction (D8 Discover Bruker AXS diffractometer, CuK α radiation, λ = 1.540 Å). The microstructure and chemical composition of the prepared black phosphorus were studied using a high-resolution scanning electron microscope (Zeiss Ultra Plus, Zeiss, Germany) equipped with an energy dispersive x-ray spectrometer (INCA, Oxford, UK) and a scanning electron microscope (FEI, Quanta FEG 450) equipped with an EDX detector (BRUKER). Raman spectroscopy was carried out at room temperature using a confocal Labram 300 spectrometer (Horiba Jobin-Yvon) and λ =532 nm and acquired on different locations of the sample powder. Aberration-corrected STEM analysis was carried out on a Jeol 2100F microscope operating at 200 kV. The size distribution was determined using a Zetasizer Nano ZS (Malvern Instruments, Ltd., UK) at 25 °C and atomic force microscopy (AFM) imaging was performed by using the Veeco Dimension ICON system operating in tapping mode.

Results and Discussion

The optimization of the quantity of copper used as catalyst for the synthesis of BP was studied. The three tests were realized using the same procedure announced above and the products of the recovered tubes are then analyzed (cold zone and hot zone).

The diffractograms of the obtained phases during the optimization tests are represented in Fig. 1(a-e) according to the following nomenclature in Table 1.

Analysis of the phases recovered in the tubes revealed the compositions grouped in Table 2.

TABLE 1. Nominations used in the phase analysis.

Abbreviation	Signification
BP2QZF	Products recovered in the cold zone of the tube (synthesized with Cu 2Q) 2Q = 45.5 mg.
BP2QZC	Products recovered in the hot zone of the tube (synthesized with Cu 2Q).
BP1QZF	Products recovered in the cold zone of the tube (synthesized with Cu 1Q) 1Q = 22.75 mg.
BP1QZC	Products recovered in the hot zone of the tube (synthesized with Cu 1Q).
BP1QZC	Products recovered in the hot zone of the tube (synthesized with Cu 1/2Q) 1/Q = 11.37 mg.

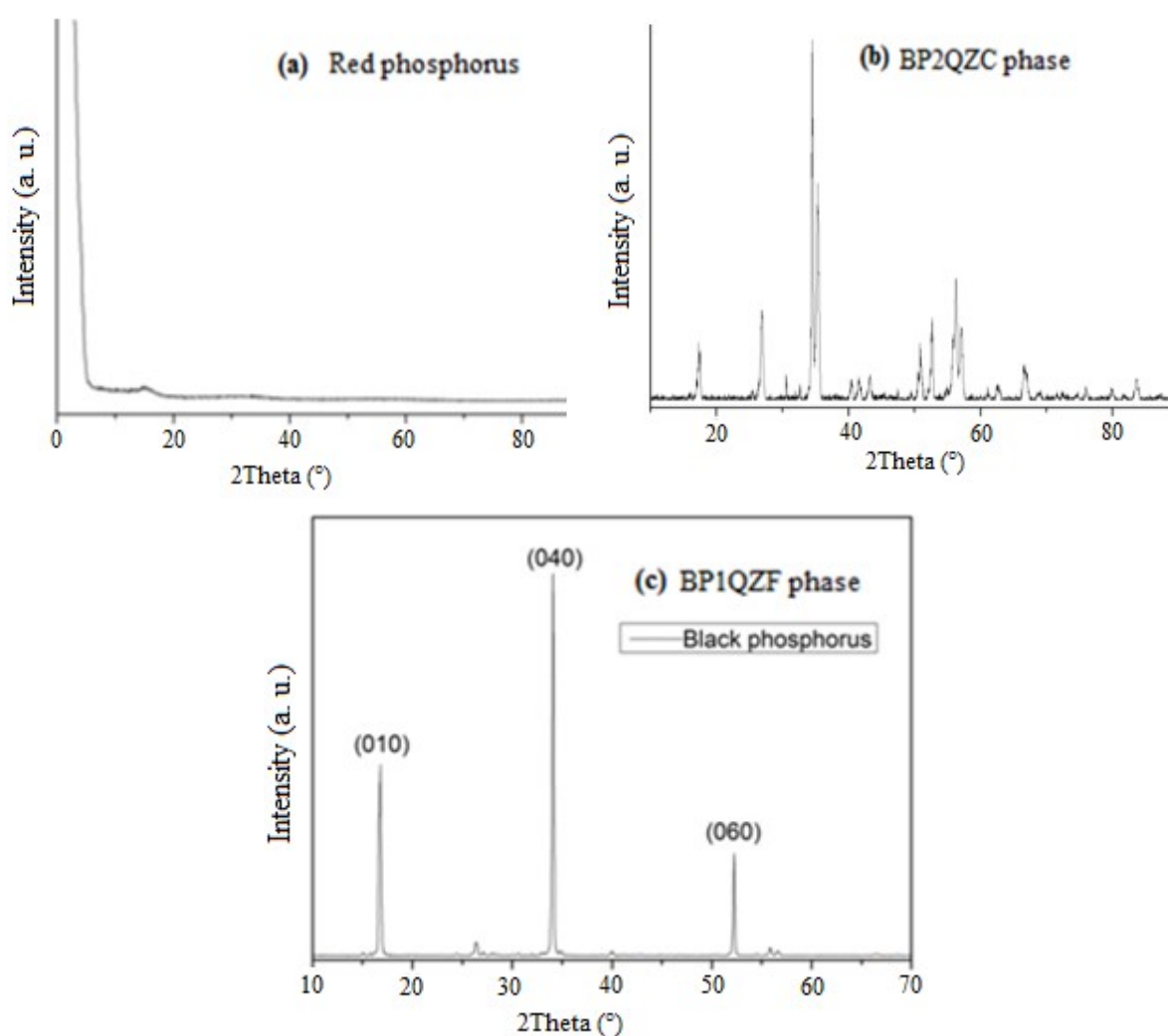


FIG. 1. X-ray powder diffraction: a) red phosphorus, b) BP2QZC phase and c) BP1QZF phase.

TABLE 2. Influence of the amount of Cu in the synthesis of black phosphorus.

Amount of Cu	Phases in the hot zone	Phases in the cold zone	Remarks
22.75 mg	$\text{Cu}_4\text{SnP}_{10}$ Cu_2P_7 SnCu_2P_2 Cu P_2O_5 PO_2	Black phosphorus (BP)	<ul style="list-style-type: none"> • High crystallinity of black phosphorus • Traces of oxygen in the tubes
45.5 mg	Cu_2P_7 $\text{Cu}_4\text{SnP}_{10}$ SnI_4	Black phosphorus (BP) Iodine SnI_4 SnP_3 CuSn	<ul style="list-style-type: none"> • Low crystallinity • a, b, c different from those of 1 Q • SnI_4 appeared, because washing is not performed.
11.37 mg	Amorphous RP Cu SnI_4	RP spread on the surface of the tube	<ul style="list-style-type: none"> • The amount of Cu is insufficient to convert RP into BP.

The existence of traces of oxygen in the tubes led to the existence of secondary phases composed by the starting materials. The optimal amount of Cu to produce black phosphorus with good crystallinity and purity was 22.75mg. The tests with 11.37mg of copper did not make it possible to obtain black phosphorus; the quantity of Cu could not convert red phosphorus into black phosphorus. The tube analysis showed the existence of black phosphorus spread on the surface of the tube in the hot zone and in the cold zone.

The XRD pattern of the obtained black phosphorus using 22.75mg of copper is presented in Fig 1.c and shows the presence of only three peaks corresponding to the planes (020), (040) and (060), indicating a pure and well-crystallized BP material according to the BP (PDF: 04-015-0991), space group Cmce (No: 64). The X-ray data demonstrates the high purity and crystallinity of BP without impurities. The strong preferential orientation along the b-axis is observed by analyzing the (040) diffraction peak. The obtained lattice parameters are $a = 3.314 \text{ \AA}$, $b = 10.482 \text{ \AA}$ and $c = 4.375 \text{ \AA}$.

Typical SEM micrographs and EDX spectra of the obtained black phosphorus are shown in Fig.2. The SEM pictures clearly show the layer architecture of black phosphorus. A semi-quantitative EDX measurement is used to determine the chemical composition of the crystal,

revealing a composition of P (97.83wt %) and O_2 (2.17wt %). The detected oxygen can be attributed to the exposure of black phosphorus to air during handling and characterization.

The identification of the vibrational mode of black phosphorus was found to be in agreement with the studies reported in the literature [18,19]. In the low-frequency region, we observe a mode with medium to low intensities. As shown in Fig. 3, three Raman peaks are observed at 362.5 cm^{-1} , 438.6 cm^{-1} and 467.5 cm^{-1} , corresponding to A^1_g , B^2_g and A^2_g normal vibrational modes (Fig. 3a, 3b), which are in good agreement with the reported data on black phosphorus in literature. These results are consistent with the XRD data and confirm the high purity of the prepared BP.

Transmission electron microscopy (TEM) analysis of the as-synthesized BP is shown in Fig. 4. Large crystalline grains with a size of about $6 \times 15 \text{ \mu m}^2$ are observed (Fig. 4a), where single crystallinity is shown in the high resolution which is an important request for electronic applications. A careful measurement of the lattice fringes in the HR image (Fig. 4b) gives a value of around 2.3 \AA that corresponds to the (014) planes of a bulk BP crystal, which is coherent with well-known BP lattice parameters.

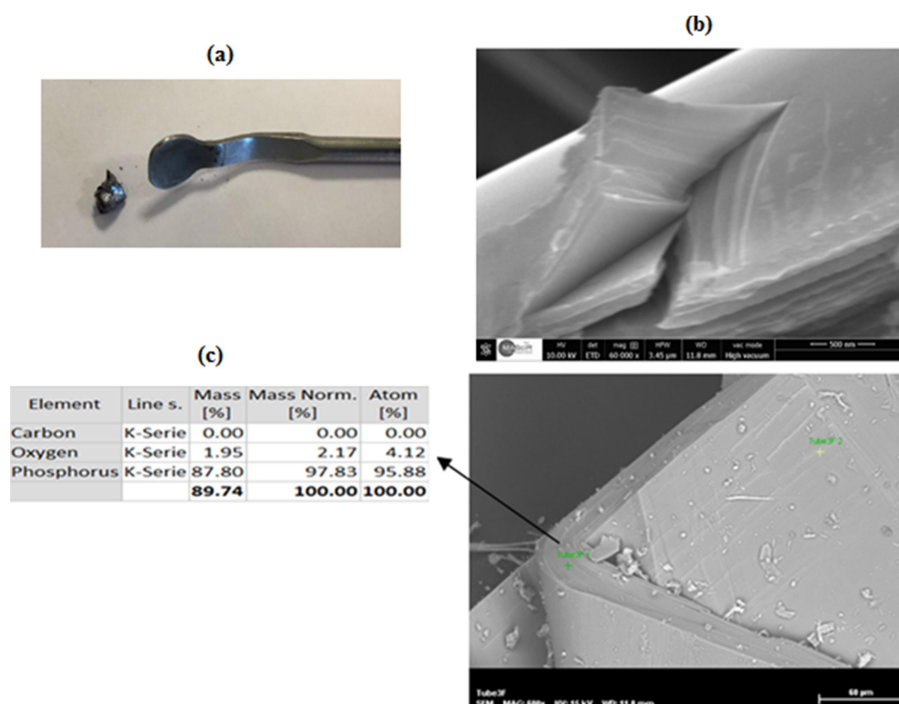


FIG. 2. (a) Photograph of black phosphorus, (b) SEM images of black phosphorus and (c) EDX measurements.

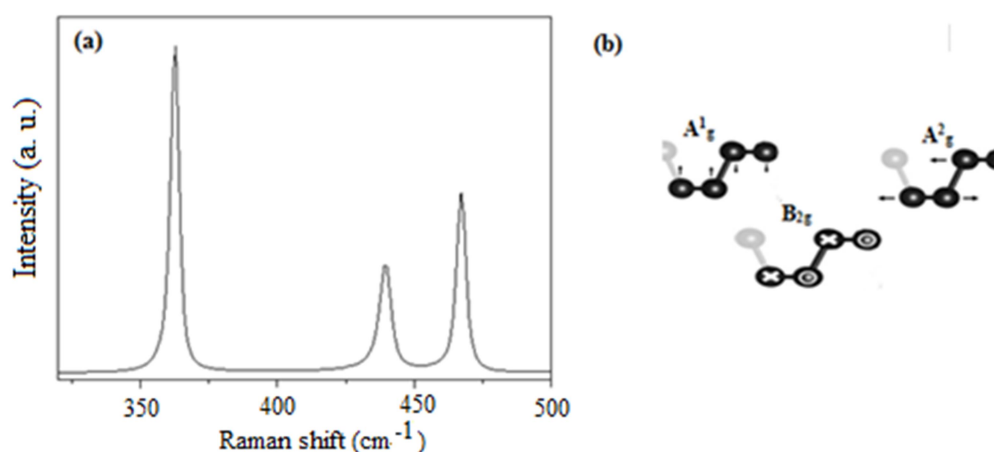


FIG. 3. (a) Raman spectrum of as-prepared black phosphorus recorded at room temperature and (b) vibrational modes of black phosphorus.

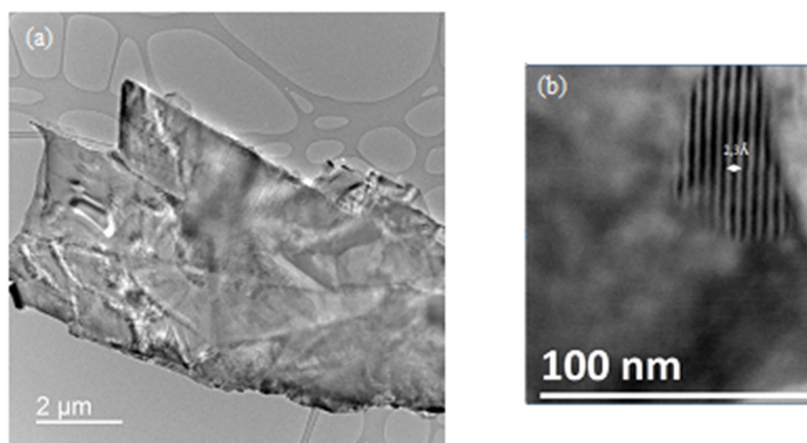


FIG. 4. (a) TEM analysis of black phosphorus and (b) corresponding lattice fringes.

Liquid exfoliation of the prepared black phosphorus in NMP gave a dispersed supernatant which was centrifuged at 13000 rpm. STEM analysis (Fig. 5) shows the dispersion of the nanosheets, which approves the success of BP exfoliation.

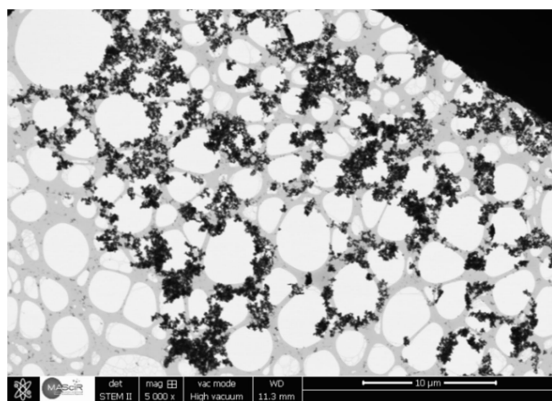


FIG. 5. STEM analysis of exfoliated black phosphorus (13000 rpm).

AFM experiments revealed the presence of layers with a narrow range of shapes and sizes. Height profiles taken on large nanosheets revealed a thickness of about 23 nm (Fig. 6). Previous AFM measurements in the literature [20] suggest that single-layer phosphorene has a thickness of 0.9 nm. Therefore, AFM images here suggest that the large nanosheets consist of 18-20 phosphorene layers. However, single- or bilayer phosphorene (0.9-1.6 nm) thickness can be produced by improving the experimental conditions (sonification power and time, centrifugation speed, ... etc.). The AFM results suggest that increasing the exfoliation time for more than 8 hours breaks down the larger sheets into smaller nanosheets that could be predominantly single- and bilayer phosphorene. We have shown by this exfoliation that our synthetic product is easily exfoliable and could potentially give high-quality systems with controlled number of layers.

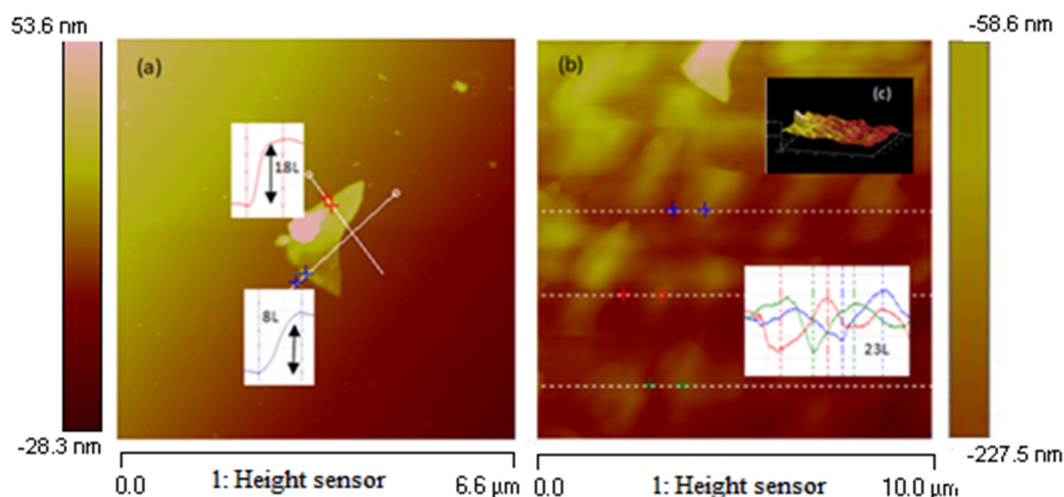


FIG. 6. AFM image of exfoliated BP layers deposited on SiO_2/Si a) lower concentration of BP in NMP (1 mg/ml), b) higher concentration (5 mg/ml) and c) three-dimensional representation of the surface in (c).

Conclusion

In this paper, we have improved the conditions of synthesis of black phosphorus with high yield and quality. This method also reduces phases that appear with gold as catalyst, which are sometimes difficult to remove. The presence of some traces of SnI_4 on the final product can be eliminated by washing with toluene. The crystal quality is proved by X-ray,

Raman and SEM. The crystal with sizes in the order of several millimeters can be exfoliated easily (8h-sonification followed by centrifugation) into one or more layers depending on the speed of centrifugation and the solvent used. These layers of phosphorene are interesting for various applications in microelectronics and photo catalysis.

References

- [1] Samuel Reich, E., *Nature*, 506 (2014) 19.
- [2] Tiouitchi, G., Raji, M., Mounkachi, O., Ait Ali, M., Mahmoud, A., Boschini, F., Essabir, H., Bouhfid, R. and El Kacem Qaiss, A., *Compos., Part B: Eng.*, 175 (2019) 107165.
- [3] Buscema, M., Groenendijk, D.J., Steele, G.A., van der Zant, H.S.J. and Castellanos-Gomez, A., *Nat. Commun.*, 5 (2014) 4651.
- [4] Park, C.-M. and Sohn, H.-J., *Adv. Mater.*, 19 (2007) 2465.
- [5] Gui, G., Morgan, D., Booske, J., Zhong, J. and Ma, Z., *Appl. Phys. Lett.*, 106 (2015), DOI 10.1063/1.4907410.
- [6] Fivaz, R. and Mooser, E., *Phys. Rev.*, 163 (1967) 743.
- [7] Tran, V., Soklaski, R., Liang, Y. and Yang, L., *Phys. Rev. B*, 89 (2014) 235319.
- [8] Shirotani, I., *Mol. Cryst. Liq. Cryst.*, 86 (1982) 203.
- [9] Jamieson, J.C., *Science*, 139 (1963) 1291.
- [10] Bridgman, P.W., *J. Am. Chem. Soc.*, 36 (1914) 1344.
- [11] Maruyama, Y., Suzuki, S., Kobayashi, K. and Tanuma, S., *Phys. B+C*, 105 (1981) 99.
- [12] Krebs, H., Weitz, H. and Worms, K.H., *ZAAC J. Inorg. Gen. Chem.*, 280 (1955) 119.
- [13] Baillargeon, J.N., Cheng, K.-Y., Cho, A.Y., Chu, S.-N., Chu, G. and Hwang, W.-Y., *Lucent Technol. Inc., Murray Hill, N.J., Assignee*, (2000) 2.
- [14] Lange, S., Schmidt, P. and Nilges, T., *Inorg. Chem.*, 46 (2007) 4028.
- [15] Tiouitchi, G., Ait Ali, M., Benyoussef, A., Hamedoun, M., Lachgar, A., Benaissa, M., Kara, A., Ennaoui, A., Mahmoud, A., Boschini, F., Oughaddou, H., El Kenz, A. and Mounkachi, O., *Mater. Lett.*, 236 (2019) 56.
- [16] Backes, C., Higgins, T.M., Kelly, A., Boland, C., Harvey, A., Hanlon, D. and Coleman, J.N., *Chem. Mater.*, 29 (2017) 243.
- [17] Brent, J.R., Savjani, N., Lewis, E.A., Haigh, S.J., Lewis, D.J. and O'Brien, P., *Chem. Commun.*, 50 (2014) 13338.
- [18] Sugai, S., Ueda, T. and Murase, K., *J. Phys. Soc. Japan*, 50 (1981) 3356.
- [19] Vanderborgh, C.A. and Schiferl, D., *Phys. Rev. B*, 40 (1989) 9595.
- [20] Liu, H., Neal, A.T., Zhu, Z., Luo, Z., Xu, X., Tománek, D. and Ye, P.D., *ACS Nano*, 8 (2014) 4033.

Structural, Electrical and Thermal Properties of Composites Based on Conducting Polymer

N. Aribou^a, S. Barnoss^a, M. El Hasnaoui^a, M. E. Achour^a and L. C. Costa^b

^aLaboratory of Material Physics and Subatomic, Faculty of Sciences, Ibn Tofail University, BP 242, 14000 Kenitra, Morocco.

^bI3N and Physics Department, University of Aveiro, 3810-193 Aveiro, Portugal.

Doi : <https://doi.org/10.47011/13.2.7>

Received on: 08/08/2019;

Accepted on: 3/11/2019

Abstract: In this work, we report the structural, thermal and electrical properties of composites consisting of polypyrrole particles in a polymethylmethacrylate matrix. Electrical resistivity analysis of these percolating composites showed a remarkable change in the conduction mechanisms below and above the percolation threshold. Structural properties were studied using X-ray diffraction, showing increases in the crystallinity index for filler concentrations above the critical percolation. Thermogravimetric analysis was used to study thermal degradation. It shows a transition from a single peak for concentrations below the percolation threshold to a double peak for concentrations above that point. The increase in the degradation temperature with the concentration of polypyrrole indicates the increase of thermal stability.

Keywords: Conducting polymer, Percolation threshold, Crystallinity, Thermal degradation, X-Ray diffraction.

Introduction

Conducting polymers are the purpose of many types of research, not only at the fundamental level, but also as several potential applications [1-4]. These materials can combine the electrical properties of the filler with the mechanical properties of the matrix. The description of the mechanisms of electronic transport of these composites is based on the concept of percolation [5]. Percolating systems based on composite materials are formed with insulating matrix loaded with conducting charges. One of the most important conducting polymers is polypyrrole (PPy); it exhibits interesting properties, such as high conductivity and can easily mix with a polymeric matrix [6]. On the other hand, polymethylmethacrylate (PMMA) is a suitable matrix, because it is readily available and easy to cast into desired

forms maintaining the mechanical integrity of the matrix.

A study of the electrical and dielectric properties of PMMA/PPy composite has been already presented. El Hasnaoui et al. [7] analyzed the electrical conductivity spectrum, finding that the hopping of charge carriers between localized states is the dominant conduction mechanism. Aribou et al. [8] performed an analysis on the real and imaginary parts of permittivity in a wide range of frequency using the impedance spectroscopy, concluding that the response of these materials has an abnormal low-frequency dispersion due to the localized or almost free charge carriers. Thus, in order to complete these studies, the thermal and structural properties of these composites were investigated. In this paper, we explore experimental measurements on such composites

in order to obtain the structure, electrical resistivity and thermal properties characterizing the electrical transport mechanisms governing this type of material.

Experimental

Samples Preparation

The PPy powder was obtained by doping intrinsic PPy with tosylate anion TS^- . The doping rate was controlled by the XPS technique and was found of the order of one sulphur (S) for four nitrogen (N); that is, one tosylate ion TS^- for four pyrrole monomers [9]. The average grain size of PPy is in the range of 10–15 μm . The two powders, PMMA and PPy, were mixed in several proportions of filler and pressed at 5000 $\text{kg}\cdot\text{cm}^{-2}$ and 150 $^{\circ}\text{C}$. Then, the samples were allowed to cool freely to room temperature to give solid disc-shaped samples. All discs had a diameter of 13 mm and 3–4 mm thickness. The direct current conductivities of the PPy and PMMA matrix are, respectively, 54 and 3.10^{-8} ($\Omega\cdot\text{m}$) $^{-1}$ and the densities are 1.20 and 1.14–1.20 $\text{g}\cdot\text{cm}^{-3}$, respectively. The glass transition temperature of PMMA polymer is $T_g \approx 115$ $^{\circ}\text{C}$ [5].

Characterization

Structural characterizations were made by X-ray diffraction (XRD) using a Philips X'pert MPD diffractometer, operating at 40 kV and 30 mA, equipped with a Cu anticathode of wavelength $\lambda = 1.5406$ \AA .

The electrical resistivity was measured using a 617 Keithley electrometer, at constant temperature $T=300$ K. The samples were prepared as discs of thickness of about 3–4 mm with aluminum electrodes of 10 mm diameter on the opposite sides of the sample. The electrical contacts were made with silver paint.

TGA was carried out using a Shimadzu TGA-50 Thermogravimetric Analyzer. The measurements were taken under an atmosphere of nitrogen with a flow rate of 30 $\text{mL}\cdot\text{min}^{-1}$, at temperatures between 20 and 800 $^{\circ}\text{C}$ and a heating rate of 5 $^{\circ}\text{C}\cdot\text{min}^{-1}$. The samples were placed in platinum cells.

Results and Discussion

X-ray Diffraction

X-ray diffraction (XRD) diagrams of four samples of the PMMA/PPy composites are shown in Fig. 1. It allows us to make an analysis of the dispersion of the PPy inclusions in the PMMA matrix. The diffraction peak that is observed at 31.2° corresponds to conducting filler that is the TS^- -doped PPy structure. The peak intensity increases with PPy concentration, which means that the crystallinity of the PMMA/PPy composite increases. The crystallinity index (CrI) was calculated from XRD data according to the Segal empirical method [10] written as follows:

$$CrI = [(I_f - I_s)/I_f] \times 100 \quad (1)$$

where I_f is the intensity of both crystalline and amorphous peak corresponding to PPy-doped TS^- particles at $2\theta = 31.2^{\circ}$ and I_s is the minimum height between two peaks at about $2\theta = 26^{\circ}$. The crystallinity index (CrI) of PMMA/PPy composites has been calculated for all concentrations of PPy particles by taking the amorphous and crystalline contributions to the diffraction intensity and the results are shown in Fig. 2. As can be seen, the obtained values of CrI are between 40 and 70 % which are greater than those obtained in two series: PMMA/CdS composites that are between 39 and 42 % [11] and PMMA/ TiO_2 composites that are between 10 and 19 % [12]. These differences are related to the type of conducting charges used in each series; i.e., the PPy doped with TS^- has more effect on PMMA crystallinity than cadmium sulfide (CdS) and titanium dioxide (TiO_2) semiconductor particles. It can also be noticed that there is a significant change in the value of the crystallinity index below and above the percolation threshold, which will be determined into "electrical resistivity analysis" section. Above the percolation threshold, the crystalline index takes the highest value, which demonstrates the significant effect of PPy particles on electrical transport mechanisms governing this conducting composite.

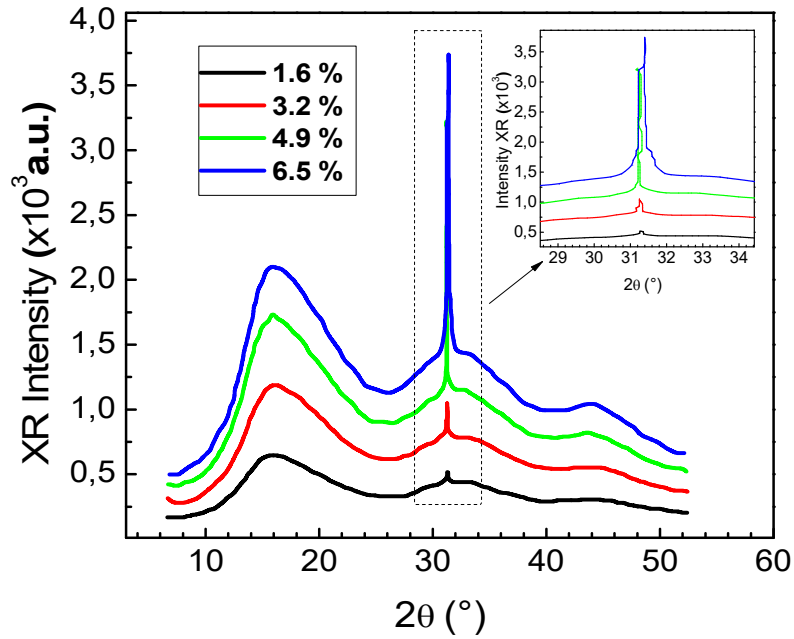


FIG. 1. X-ray diffraction (XRD) diffractograms of PMMA/PPy composites.

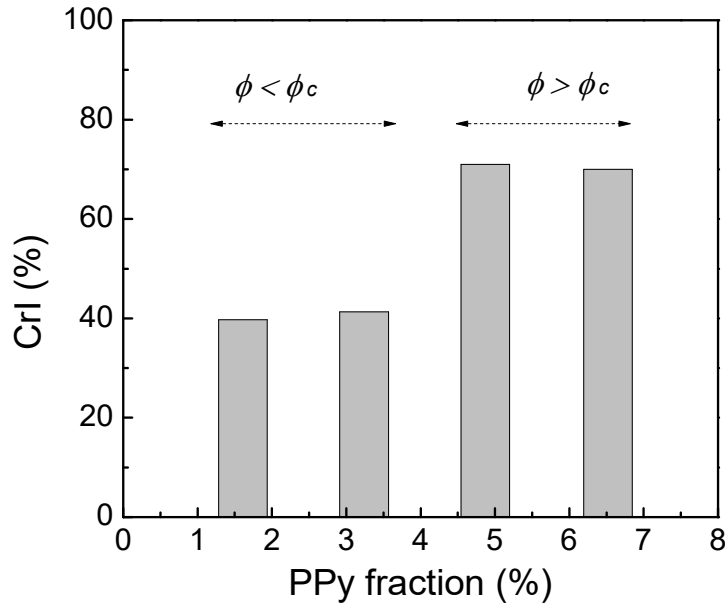


FIG. 2. The crystallinity index (CrI) as a function of PPy concentration at a temperature of 300 K.

Electrical Resistivity Analysis

Fig. 3 shows the semi-logarithmic curve of ρ as a function of PPy fraction embedded in a PMMA polymer matrix, at a temperature of $T=300$ K. As can be seen, the behavior of ρ can be divided into three regions [13]. In region I, the small decrease in resistivity of the composite can be attributed to the transportation of the small number of conducting charges through the PMMA/PPy composite without having any continuous conductive path. In region II,

resistivity decreases sharply due to a continuous conductive path developed in the PMMA matrix. The estimated percolation threshold, ϕ_c , is about 3.24%, where resistivity begins to decrease abruptly. This major jump in resistivity could be attributed to the formation of an infinite agglomerate pathway that allows electrons to travel a macroscopic distance through the PMMA matrix. In region III, further addition of conducting particles has a marginal effect on resistivity. The creation of PPy conducting network-like structure in the PMMA/PPy

composites results in removing the static charge from the sample surface [14]. The behavior of experimental data, in this region, could be modelled by the percolation model [15,16] written as follows:

$$\rho = \rho_o(\phi - \phi_c)^{-t} \text{ for } \phi > \phi_c \quad (2)$$

where, the exponent t is a parameter related to the dimensionality of the composite and ρ_o is a pre-exponent factor. Fig. 4 shows $\log \rho$ as a function of $\log(\phi - \phi_c)$ for the PPy fractions above the percolation threshold. Fitting the percolation model (Eq. (2)) to the experimental data yields the pre-exponent $\rho_o = 34,7 (\Omega.m)$ and $t = 1.69 \pm 0.12$. This value is close to that of the universal three-dimensional

percolating systems that is equal to 2 [17]. Omastov and Simon [14] have presented a study on the same composites, finding the same behavior, but with a lower percolation threshold. This can be justified by the prepared procedure, where they used a dilution with 25% of water, containing FeCl_3 particles. In our case, the composites contain TS^- anions, changing the viscosity of the PMMA/PPy composite. It is known that low percolation thresholds are always achieved with low viscosity composites [18] and could be also the result of the degree of dispersion or interfacial adhesion between PPy particles and the PMMA matrix [19].

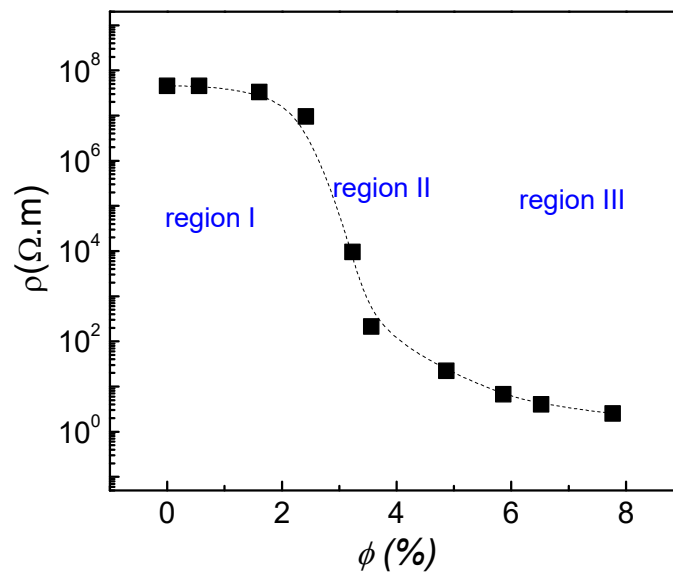


FIG. 3. Semi-log plot of electrical resistivity ρ versus PPy concentration at room temperature. Dashed line is drawn to guide the eyes.

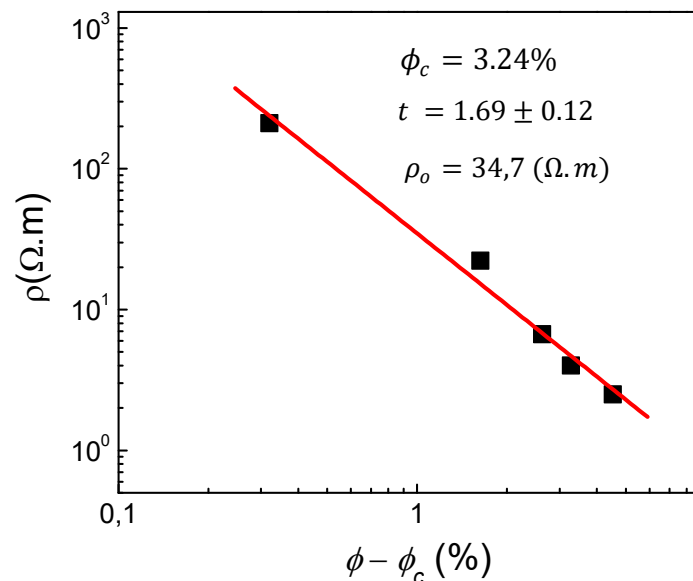


FIG. 4. Log-log plot of ρ versus $\phi - \phi_c$ for concentrations above the percolation threshold at a temperature of $T = 300$ K. Solid line represents the best linear fit of data with a correlation coefficient $R^2 = 0.98$.

Thermal Properties

We have reported in Fig. 5 the measured relative evolution of the mass losses of four samples obtained from the TGA spectrum in the range of temperature from 20 to 500 °C. It is clearly seen that the thermal degradation of these samples starts around 250 °C with a significant mass loss of approximately 97%, corresponding to thermal degradation of the PMMA polymer. The loss of mass reaches its maximum value beyond 440 °C for a given PPy concentration and the rate of degradation slightly depends on the PPy fraction in the matrix. In order to look for deep analysis and identify the significant

variations of these curves, we calculated the derivative weight of each curve. Figs. 6 and 7 show the comparative curves of weight loss and its derivatives for the PPy fraction-reinforced PMMA matrix. The thermal decomposition temperatures of the PMMA/PPy composites increased with increasing the concentration of PPy. The presence of the PPy particles can lead to the stabilization of the PMMA matrix and good interfacial adhesion between the PPy and the PMMA may restrict the thermal motion of the PMMA molecules [20], resulting in increased thermal stability of the PMMA/PPy composites.

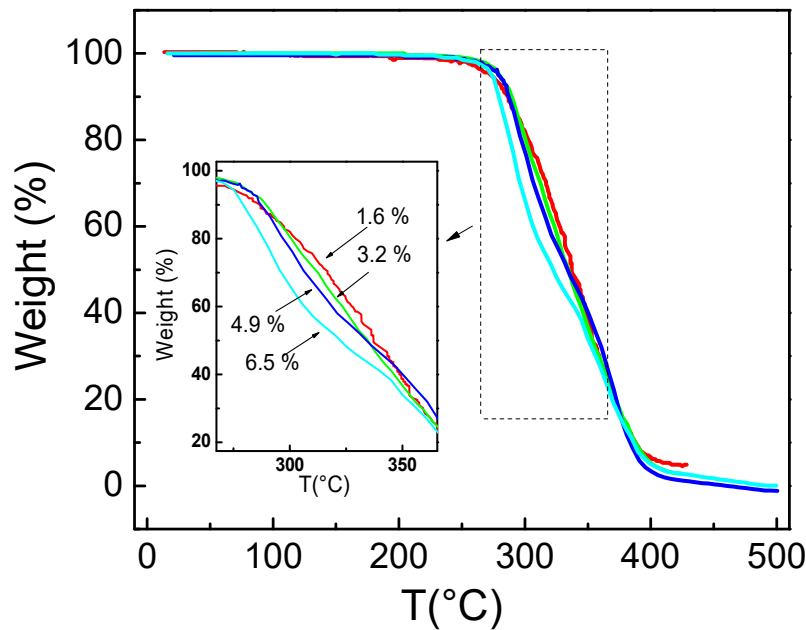


FIG. 5. TGA thermograms of PMMA/PPy composites for different PPy concentrations.

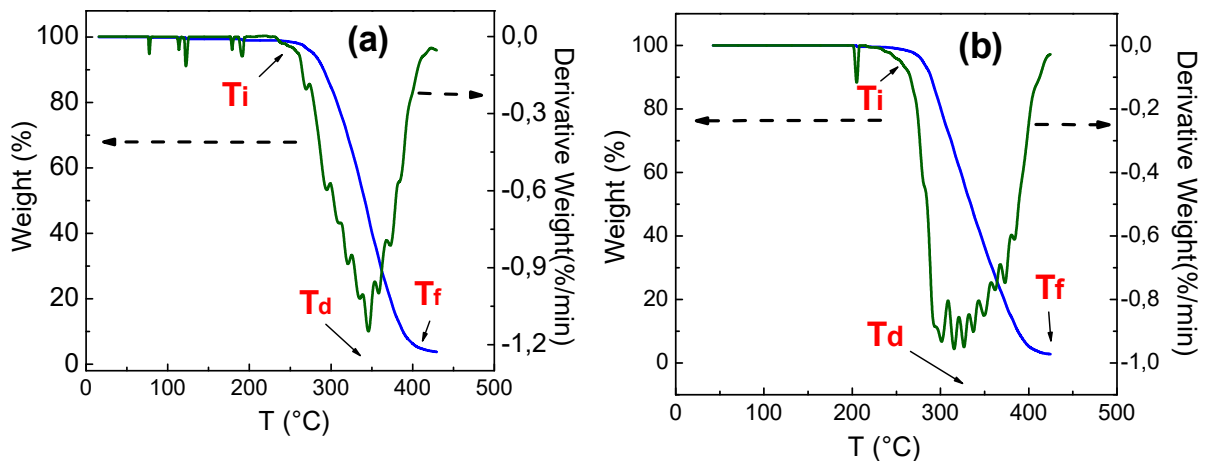


FIG. 6. TGA and derivative thermograms of PMMA/PPy composites for PPy concentrations below the percolation threshold, 1.6 % (a) and 3.2 % (b).

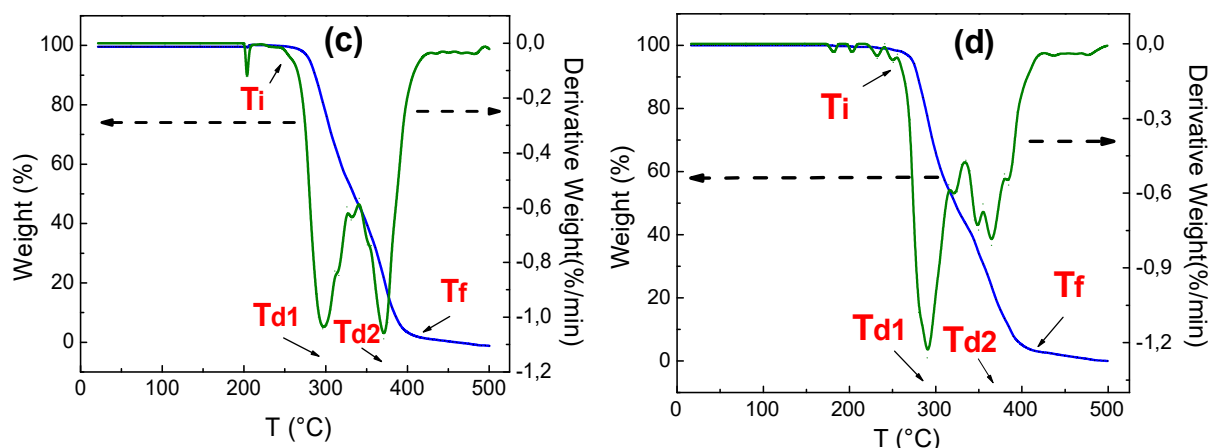


FIG. 7. TGA and derivative thermograms of PMMA/PPy composites for PPy concentrations below the percolation threshold, 4.9 % (c) and 5.6 % (d).

It clearly appeared from Table 1 that, for concentrations below the percolation threshold ϕ_c (Fig. 6), there is only a single endothermic peak in derivative weight, whereas there are double endothermic peaks for concentrations above ϕ_c (Fig. 7). Table 1 illustrates the temperature values of initial degradation T_i , first degradation T_{d1} , second degradation T_{d2} and final degradation T_f . We observe that there are significant changes in the values of these parameters; i.e., when the PPy filler increases from low concentrations ($\phi < \phi_c$) to high concentrations ($\phi > \phi_c$), the temperature of

initial degradation (243-245 °C) is increased to (253-254 °C) and the degradation of PMMA/PPy follows two steps, characterizing two thermal degradations. We attribute this behavior to the existence of two non-compatible phases forming the molecular level of composites that explains the phenomenon of degradation found below and above the percolation threshold. The same behavior was observed in thermal analysis of PMMA/multiwalled carbon nanotube (MWCNT) composites presented by Choi et al. [21], where they found that the addition of MWNTs as a filler improved the intrinsic properties.

TABLE 1. Temperature and mass loss characteristics of thermal degradation of PMMA/PPy composites.

ϕ (%)	1.6	3.2	4.9	6.5
T_i (°C)	243	245	254	253
T_{d1} (°C)	345	327	297	290
T_{d2} (°C)			370	365
T_f (°C)	405	408	405	403
Mass of loss (step I) (%)			49	48
Mass of loss (step II) (%)	95	96	48.5	48.5
Mass of loss			97.5	96.5

Conclusion

This paper presents a study of structural, electrical and thermal properties of PPM/PPy composites. Analysis of electrical resistivity *versus* PPy fraction showed a percolation threshold at which the behavior of transport mechanism changes. Thermal gravimetric

analysis was used to study the evolution of the thermal stability of PMMA/PPy composites; it shows that the rate of degradation slightly depends on the PPy content in the PMMA matrix. Moreover, X-ray diffraction patterns indicate that the crystallinity index of composites increases with increasing the PPy fraction.

References

- [1] Chandrasekhar, P., "Conducting Polymers, Fundamentals and Applications: Including Carbon Nanotubes and Graphene", 2nd Ed., (Cham Switzerland: Springer International Publishing, 2018), pp. 549-714.
- [2] Deshpande, P.P. and Sazou, D., "Corrosion protection of metals by intrinsically conducting polymers", 1st Ed., (CRC Press LLC, New York, 2016).
- [3] Otero, T.F., Schneider, H.J. and Shahinpoor, M., "Conducting-polymers: bioinspired intelligent materials and devices", (Croydon U.K.: Royal Society of Chemistry, 2015).
- [4] Bouknaitir, I., Aribou, N., Elhad Kassim, S.A., El Hasnaoui, M., Melo, B.M.G., Achour, M.E. and Costa, L.C., *Spectro. Lett.*, 50 (2017) 196.
- [5] Achour, M.E., Droussi, A., Zoulef, S., Gmati, F., Fattoum, A., Belhadj, M.A. and Zangar, H., *Spectro. Lett.*, 41 (2008) 328.
- [6] Costa, L.C., Henry, F., Valente, M.A., Mendiratta, S.K. and Sombra, A.S., *Eur. Polym. J.*, 38 (2002) 1495.
- [7] El Hasnaoui, M., Abazine, K., Achour, M.E. and Costa, L.C., *J. Optoelectron. Adv. Mater.*, 18 (2016) 389.
- [8] Aribou, N., Elmansouri, A., Achour, M.E., Costa, L.C., Belhadj, M.A., Oueriagli, A. and Outzourhit, A., *Spectro. Lett.*, 45 (2012) 477.
- [9] Belhadj, M.A., Miane, J.L. and Zangar, H., *Polym. Int.*, 50 (2001) 773.
- [10] Segal, L., Creely, J.J., Martin Jr., A.E. and Conrad, C.M., *Textile Res. J.*, 29 (1959) 786.
- [11] Patel, A.K., Jain, N., Patel, P., Das, K. and Bajpai, R., *AIP Conference Proceedings*, 1942 (2018) 070029.
- [12] El-Zaher, N.A., Melegy, M.S. and Guirguis, O.W., *Natural Science*, 6 (2014) 859.
- [13] Foulger, S.H., *J. Appl. Polym. Sci.*, 72 (1999) 1573.
- [14] Omastov, M. and Simon, F., *J. Mater. Sci.*, 35 (2000) 1743.
- [15] Stauffer, D. and Aharony, A., "Introduction to percolation theory", (Taylor and Francis, London, 1992).
- [16] Kirkpatrick, S., *Rev. Mod. Phys.*, 45 (1973) 574.
- [17] Grimaldi, C and Balberg, I., *Phys. Rev. Lett.*, 96 (1) (2006) 066602.
- [18] Kovacs, J.Z., Velagala, B.S., Schulte, K. and Bauhofer, W., *Compos. Sci. Technol.*, 67 (2007) 922.
- [19] Ma, P.-C., Siddiqui, N.A., Marom, G. and Kim, J.K., *Compos., Part A: Appl. Sci. Manuf.*, 41 (2010) 1345.
- [20] El-Zaher, N.A., Melegy, M.S. and Guirguis, O.W., *Natural Science*, 6 (2014) 859.
- [21] Choi, H.J., Lim, J.Y. and Zhang, K., *Diamond Relat. Mater.*, 17 (2008) 1498.

Structural and Dielectric Properties of $\text{Zn}_{1-x}\text{Mo}_x\text{O}$ Nanoparticles

H. Basma, F. Al-Mokdad and R. Awad

Department of Physics, Faculty of Science, Materials Science Lab, Beirut Arab University, Debbieh, Lebanon.

Doi : <https://doi.org/10.47011/13.2.8>

Received on: 08/08/2019;

Accepted on: 26/2/2020

Abstract: In this work, samples of zinc oxide nanoparticles doped by molybdenum ($\text{Zn}_{1-x}\text{Mo}_x\text{O}$ with $0 \leq x \leq 0.1$) were prepared by using the wet co-precipitation method. The characterization of the prepared samples was carried out by means of X-ray powder diffraction (XRD). The samples reserved their hexagonal wurtzite structure with Mo doping and showed a decrease in the crystallite size up to $x = 0.04$ followed by a further increase. On the other hand, dielectric measurements were performed using an LCR meter. The effect of frequency and temperature on the dielectric properties such as the real and imaginary parts of dielectric constant (ϵ' and ϵ'' , respectively), dielectric loss ($\tan\delta$) and ac-conductivity (σ_{ac}) of Mo-doped zinc oxide samples, was studied in the frequency range (100 Hz - 1 MHz) and at temperatures (300 - 773 K). The values of room temperature dielectric parameters were found to be strongly dependent on the Mo-doping. However, the increase in temperature caused an enhancement in the values of the dielectric parameters, particularly at 773 K.

Keywords: Zinc oxide, XRD, Dielectric constants, Ac-conductivity.

Introduction

Among diluted semiconductors, extensive research was employed to study ZnO due to its interesting features, such as wide direct band gap, large exciton binding energy and high transparency in the visible region [1]. Thanks these interesting features, ZnO has been employed in various applications as light emitting diodes, piezoelectric devices, solar cells and gas sensors [2]. Research has shown that doping ZnO with transition metals enhances their structural, optical and electrical properties, which is useful in the fabrication of optoelectronic devices. Studies have reported the effects of transition metal doping on ZnO properties [3-6]. Sundar and John [7] investigated the dielectric properties of ZnO doped with Mn. The dielectric properties increased with temperature, confirming the space-charge contribution in the charge transport process and polarizability. Belkhaoui et al. [8]

studied Mn-doped ZnO nanoparticles. The ac-conductivity was decreased with Mn addition, which is attributed to the increase of defects. Boukachem et al. [9] explored the effect of Mo on ZnO thin films. The high-frequency dielectric constant and plasma pulsation showed a decrease with Mo content. Gosh et al. [10] studied the impact of Ni on ZnO prepared by precipitation method and reported the decrease in dielectric constant with the increase in Ni-doping percentages.

Doping with Mo is favorable, since it has multiple valence states and hence produces free carriers by single doping. Furthermore, the ion scattering effect is reduced due to the difference in the valence electrons between Mo and Zn ions. Therefore, the aim of this work is to study the structural, as well as dielectric properties of $\text{Zn}_{1-x}\text{Mo}_x\text{O}$ ($0.00 \leq x \leq 0.10$) nanoparticles prepared by the co-precipitation method.

Experimental Techniques

Nanoparticles of general formula $\text{Zn}_{1-x}\text{Mo}_x\text{O}$ were prepared by the wet chemical co-precipitation method as reported previously for $\text{Zn}_{1-x}\text{Er}_x\text{O}$ [11]. The structure of the samples was examined by room temperature X-Ray powder diffraction using Shimadzu-7000 advance powder diffractometer with Cu-K_α radiation ($\lambda = 1.54056 \text{ \AA}$) in the range $25^\circ \leq 2\theta \leq 75^\circ$. The dielectric properties were measured as a function of frequency and temperature using HIOKI 3532- 50 LCR Hi-tester.

Results and Discussion

Structural Properties

The XRD patterns of $\text{Zn}_{1-x}\text{Mo}_x\text{O}$ nanoparticles with $0 \leq x \leq 0.10$ are shown in Fig. 1. The diffraction peaks of the pure and Mo-doped samples confirmed the formation of a hexagonal wurtzite structure. No additional phase was observed in the XRD patterns of the Mo-doped ZnO samples up to doping value $x = 0.04$. However, a diffraction peak corresponding to MoO_3 was observed in the XRD pattern for the samples with $x = 0.06$ and $x = 0.1$. Table 1 depicts the values of the lattice parameters (a and c), the unit cell volume (v), the crystallite size

(D) and the Zn-O bond length (l) for pure and Mo-doped samples. It is noticed that both lattice parameters a and c show a decrease with x up to 0.06 and then increase for $x > 0.06$. The decrease in lattice parameter c is probably due to the fact that Mo^{6+} ions have smaller ionic radii than Zn^{2+} and a higher valence state. This causes a contraction of the unit cell and hence a decrease in its volume. The lattice parameter c increases for $x > 0.06$ and reaches the value of pure ZnO. A reasonable interpretation might be the migration of smaller Mo^{6+} ions from ZnO lattice to form MoO_3 impurity as confirmed by the XRD patterns for samples with $x \geq 0.06$. The values of the crystallite size D was obtained from the stress-strain plots. They show a decrease with x up to 0.04 and then increase to 30.11 nm for $x = 0.1$. The decrease in D might be attributed to the lowering of nucleation and decreasing growth rate of ZnO crystals resulting from the deformation of the ZnO lattice by Mo^{6+} -doping. At high substitutions of Mo^{6+} , the migration of Mo^{6+} from the ZnO matrix to form MoO_3 reduces the deformation of the lattice, changing back the value of crystallite size to that of pure ZnO sample. The Zn-O bond length decreased with x due to the substitution of Zn^{2+} ions by Mo^{6+} ions.

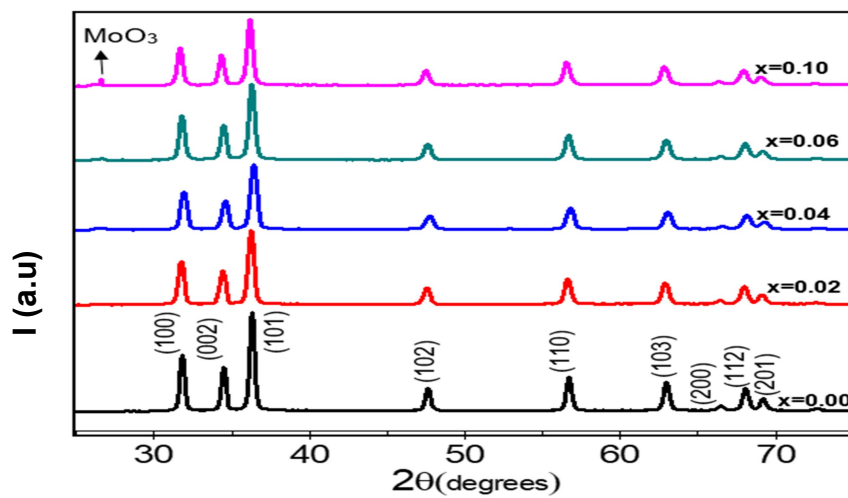


FIG. 1. XRD patterns of $\text{Zn}_{1-x}\text{Mo}_x\text{O}$ nanoparticles with $0 \leq x \leq 0.1$.

TABLE 1. Lattice parameters, unit cell volume, crystallite size and Zn-O bond length as functions of x .

x	$a (\text{\AA})$	$c (\text{\AA})$	$v (\text{\AA}^3)$	$D(\text{nm})$	$l (\text{\AA})$
0.00	3.24	5.22	47.68	31.85	1.978
0.02	3.24	5.21	47.53	27.09	1.976
0.04	3.23	5.18	47.09	26.46	1.970
0.06	3.22	5.16	46.48	29.60	1.961
0.10	3.25	5.20	46.01	30.11	1.955

Dielectric Properties

Fig. 2(a - d) shows the dependence of the real and imaginary parts of the dielectric constants (ϵ'), (ϵ''), dielectric loss tangent ($\tan \delta$) and ac-conductivity (σ_{ac}) at room temperature of pure and Mo-doped ZnO nanoparticles. For all samples, the dielectric constant (ϵ') (Fig. 2.a) shows a sharp decrease at low frequencies followed by a marginal decrease to obtain constant values up to a frequency of 1 MHz. This behavior is explained by the Maxwell-Wagner model [12] which agrees with Koop's phenomenological theory [13]. The samples consist of strongly conducting grains surrounded by weakly conducting grain boundaries. Upon the application of an external field, the charge carriers within the grains migrate and accumulate at the grain boundaries. This high accumulation causes large polarization and consequently high dielectric constants. Another

reason behind the high dielectric constant at low frequencies is the contribution of interfacial/space polarization which arises due to the inhomogeneous dielectric structure. Furthermore, as the frequency increases, the hopping between the different metal cations (Zn^{2+} and Mo^{6+}) cannot follow the applied field anymore and this explains the frequency independence of the dielectric constant at high frequencies. The variation of ϵ' with Mo doping shows an unsystematic decrease with x up to 0.06 followed by an increase for $x = 0.1$. Research has shown that polarization in nanoparticles varies by doping according to several factors, including crystallite size, cation distribution, defect density, inhomogenities, porosity of samples, number of oxidation states of the dopant element, lattice distortions and variation of bond length [14–16].

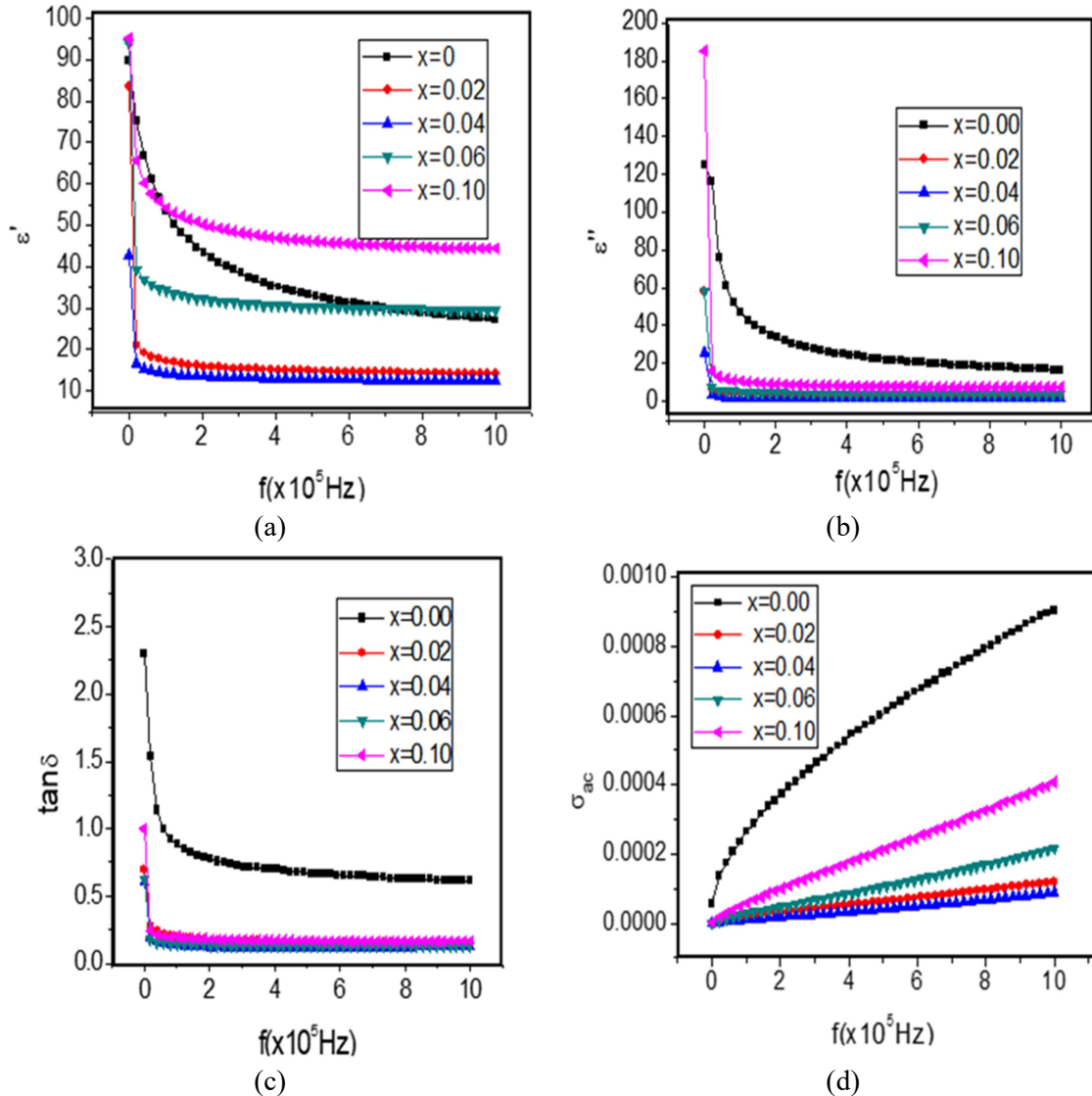


FIG. 2. Variation of ϵ' (a), ϵ'' (b), σ_{ac} (c) and $\tan \delta$ (d) versus f at $T = 300\text{K}$.

For the samples under study, the variation of the crystallite size with doping, as shown in Table 1, causes a variation in the surface to volume ratio and hence the variation of interfaces and boundary defects, at which polarization takes place, which results in a variation in the dielectric constant. Again, the incorporation of Mo ions gives rise to lattice distortion and a decrease of bond lengths, as shown in Table 1, which varies polarizability and thus dielectric constant.

Finally, the interaction between different Mo ions found in different valence states and distributed randomly over different crystallographic sites changes the polarizability and the dielectric constant.

The values of ϵ'' (Fig. 2.b) for all samples show a decrease with frequency for all samples. The values of ϵ'' are high at low frequency due to high resistivity of grain boundaries at this range of frequency, which requires more energy for polarization, resulting in a high energy loss. As frequency increases, the effect of the grain boundary decreases, accordingly less energy will be required for the hopping process. Thus, less energy is dissipated for polarization, which results in lower dielectric losses. Higher doping caused a sharp decrease in the dielectric loss at higher frequencies. The migration of Mo ions from the grain boundaries to form the MoO_3 phase reduces their contribution in dielectric losses and hence we obtain a decrease in ϵ'' . Therefore, one can conclude that the doped samples might be used in high-frequency device applications [17].

$\tan \delta$ displayed in Fig. 2.c represents the ratio of the dielectric loss to the dielectric constant and exhibits a similar trend, such that it decreases with frequency increase and increases with temperature increase, confirming Koop's theory.

For all samples, σ_{ac} (Fig. 2.d) shows a gradual increase with frequency, with a faster increment at higher frequencies. As the frequency increases, more charges can migrate between

grains as they acquire enough energy to overcome the poor conducting- grain boundary barrier [18]. Moreover, the values of σ_{ac} decrease with Mo doping. So, Mo doping hinders the hopping mechanism and hence decreases the value of σ_{ac} . This might be linked to the enhancement of zinc interstitials and oxygen vacancies by Mo doping [3]. These defects segregate at grain boundaries and assist the formation of the barrier resulting in a decrease in conductivity [13]. The small values of σ_{ac} are attributed to the space charge contribution to the charge transport process and polarizability. When the grain size is smaller than the electron mean free path, grain boundary scattering dominates and hence electrical resistivity is increased.

Fig. 3(a-d) represents the temperature dependence of all the dielectric parameters at a fixed frequency equal to 10^5 Hz. All the parameters showed an increase with temperature. This can be attributed to the increase in the number of accumulated charges at the grain boundaries due to temperature increase, which consequently leads to polarization increment and hence to an increase in dielectric constants. At lower temperatures, the charge carriers possess a weak contribution to the dielectric response. As a result, they cannot orient themselves with respect to the direction of the applied field [19]. However, as temperature increases, the drift mobility of these charge carriers increases causing an enhancement in the dielectric parameters. The contribution from space charge polarization depends on the purity and perfection of the crystal structure, which in turn are strongly dependent on temperature [20]. Hence, the large values of dielectric parameters obtained at higher temperatures may be ascribed to the creation of crystal defects as the temperature increases leading to the dominance of space charge polarization contribution [21]. It is remarkable to note that the sample of highest Mo doping possesses the highest dielectric constants with temperature.

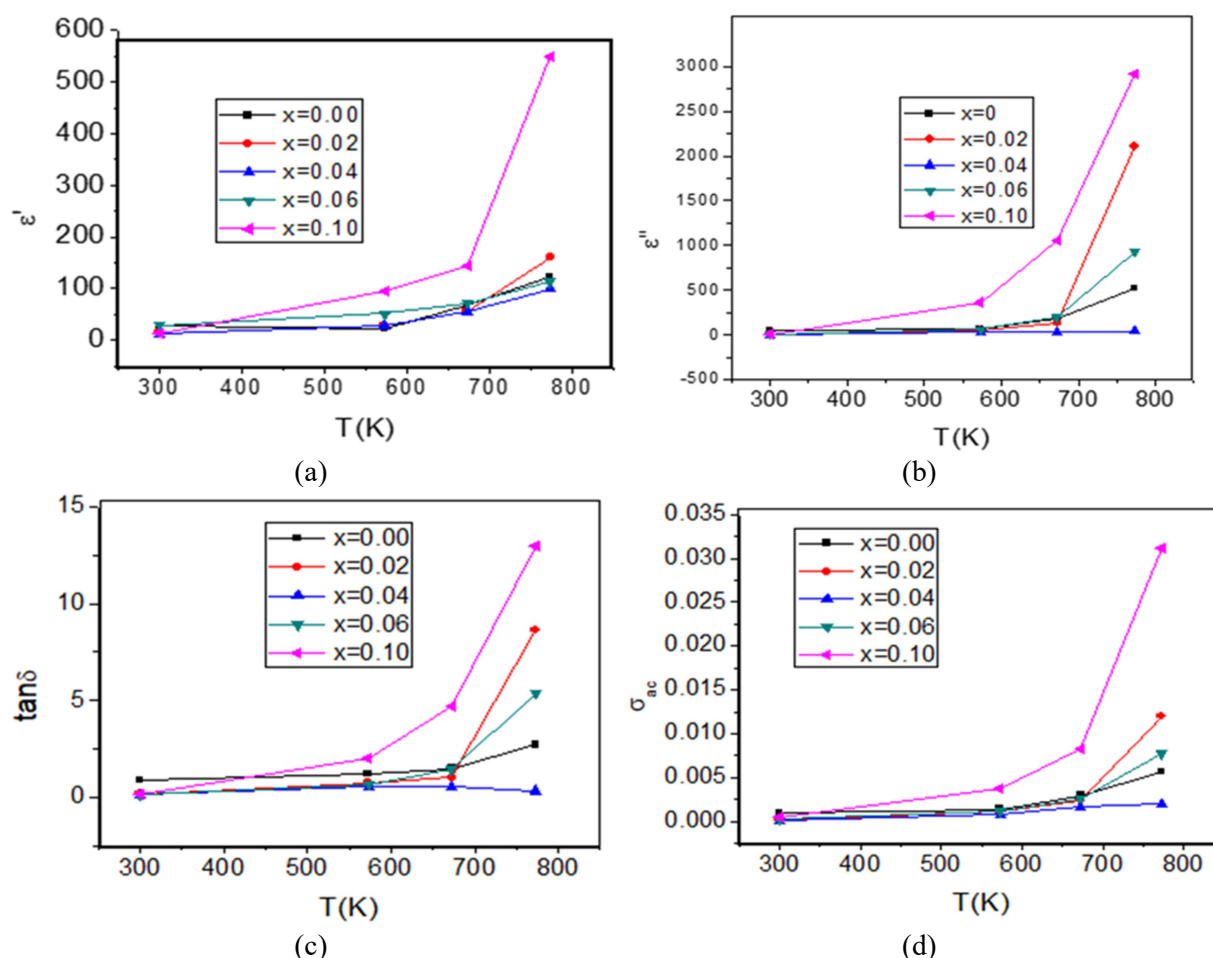


FIG. 3. Variation of ϵ' (a), ϵ'' (b), σ_{ac} (c) and $\tan\delta$ (d) versus T at $f=10^5$ Hz.

Conclusion

Mo-doped ZnO nanoparticles were successfully prepared using the wet chemical coprecipitation method. XRD measurements revealed that Mo substituted Zn without altering the hexagonal crystal structure. Room temperature dielectric measurements showed a non-systematic decrease in dielectric constant

with frequency due to electron exchange interaction. The dielectric loss was found to decrease with Mo-doping, indicating that Mo-doped ZnO nanoparticles are important for high-frequency applications. At a fixed frequency, all dielectric parameters showed an increment with the increase in temperature for both pure and doped samples.

References

- [1] Liang, P., Cai, H., Yang, X., Li, H., Zhang, W., Xu, N., Sun, J. and Wu, J., *Spectrochimica Acta, Part B: Atomic Spectroscopy*, 125 (1) (2016) 18.
- [2] Anta, J.A., Guillén, E. and Tena-Zaera, R., *J. Phys. Chem. C*, 116 (21) (2012) 11413.
- [3] Basma, H., Rahal, H.T., Al-Mokdad, F., Romie, M. and Awad, R., *Mater. Res. Express*, 6 (7) (2019) 075001.
- [4] Kumar, P., Joshi, R., Gaur, A., Kumar, L. and Asokan, K., *Mater. Res. Express*, 2 (4) (2015) 045901.
- [5] Akhtari, F., Zorriasatein, S., Farahmandjou, M. and Elahi, S.M., *Mater. Res. Express*, 5 (6) (2018) 065015.
- [6] Sharrouf, M., Awad, R., Marhaba, S. and El-Said-Bakeer, D., *Nano*, 11 (04) (2016) 1650042.
- [7] Sundar, S.A. and John, N.J., *IJEAS*, 3 (3) (2016) 26.
- [8] Belkhaoui, C., Mzabi, N. and Smaoui, H., *Mater. Res. Bull.*, 111 (2019) 70.

- [9] Boughalmi, R., Boukhachem, A., Gaied, I., Boubaker, K., Bouhafs, M. and Amlouk, M., *Mat. Sci. Semicon. Proc.*, 16 (6) (2013) 1584.
- [10] Ghosh, C.K., Malkhandi, S., Mitra, M.K. and Chattopadhyay, K.K., *J. Phys. D*, 41 (24) (2008) 245113.
- [11] Farhat, S., Rekaby, M. and Awad, R., *JSNM*, 31 (9) (2018) 3051.
- [12] Prodromakis, T. and Papavassiliou, C., *Appl. Surf. Sci.*, 255 (15) (2009) 6989.
- [13] Koops, C.G., *Phys. Rev.*, 83 (1) (1951) 121.
- [14] Thomas, N., Jithin, P.V., Sudheesh, V.D. and Sebastian, V., *J. Ceramint.*, 43 (2017) 7305.
- [15] Rajesh Kumar, B., Hymavathi, B. and Subba-Rao, T., *Journal of Science: Advanced Materials and Devices*, 3 (4) (2018) 433.
- [16] Das, P.S. and Singh, G.P., *J. Magn. Magn. Mater.*, 401 (2016) 918.
- [17] Zamiri, R., Kaushal, A., Rebelo, A. and Ferreira, J.M.F., *Ceram. Int.*, 40 (1) (2014) 1635.
- [18] Ashokkumar, M. and Muthukumaran, S., *J. Lumin.*, 162 (2015) 97.
- [19] Kingery, W.D. et al., "Introduction to Ceramics", (John Wiley, New York, 1975), p. 913.
- [20] Moulson, A.J. and Herbert, J.M., "Electroceramics: Materials, Properties, Applications", 2nd Ed., (John Wiley & Sons, Ltd., 2003).
- [21] Smyth, C.P., "Dielectric Behavior and Structure", (McGraw-Hill, NewYork, 1955).

Similarities and Differences between Two Researches in Field Electron Emission: A Way to Develop a More Powerful Electron Source

M. S. Mousa^a, A. Knápek^b and L. Grmela^c

^a Department of Physics, Mu'tah University, Al-Karak 61710, Jordan.

^b Institute of Scientific Instruments of the CAS, Královopolská 147, Brno 61264, Czech Republic.

^c Department of Physics, Brno University of Technology, Technická 8, Brno 61600, Czech Republic.

Doi : <https://doi.org/10.47011/13.2.9>

Received on: 28/11/2019;

Accepted on: 20/2/2020

Abstract: This paper discusses the similarities and differences between two studies that deal with resin-coated field-emission cathodes. The two works that are compared within this paper are entitled: *Hot Electron Emission from Composite-Insulator Micropoint Cathodes* and *Methods of Preparation and Characterization of Experimental Field-Emission Cathodes*. Within the text, both studies are reviewed and put into context, pointing out and commenting the advantageous features of this type of cathodes. The comparison focuses mainly on the method of preparation including deposition of a thin film on the cathode tip and the characterization of the coating itself. The effect of the coating on the field emission is discussed as well.

Keywords: Cold field emission, Epoxylite 478, Epoxylite EPR-4.

Introduction

At present, field electron emission from a metal through a dielectric layer is a subject of considerable interest. Its importance is caused mainly by electron devices utilizing a focused electron beam which requires a high-quality source of free electrons that is sufficiently bright and able to provide high current density and work in low-quality vacuum conditions [1, 2]. This paper discusses and further compares two experimental emitters appearing in two separate projects, implying a single way to develop the ultimate electron source.

An experimental field-emission emitter based on tungsten ultra-sharp emitter with a metal-oxide-dielectric structure proved to be the ideal candidate based on the conditions stated above. Regarding the advantages of cold field-emission

sources, it should be emphasized that only slight demagnification is required to obtain a 1nm-diameter probe, because of the small virtual source starting from 2 up to 5 nm [2]. Secondly, there is only a very small energy spread, which enables operation at low accelerating voltages. This, in turn, enables to obtain a very sharp, high-contrast image without major radiation damage, especially when working with biological specimens (e.g. tissues or single cells). Lastly, thanks the epoxy layer, it is possible to work in relatively low-quality vacuum (less than 10^{-6} Pa), preventing the ion-bombardment and chemi/physisorption of residuals on the surface of the tip. The preservation of the lower vacuum also enables faster manipulation with the sample and a generally lower price compared to devices working with UHV exceeding 10^{-7} Pa [2].

The need for a better understanding of high-voltage phenomena and development of theories of field electric emission from epoxy-coated tips represents the motivation to study further the behavior of composite tips [1-4]. In general, field electron emission occurs after switch-on voltage is applied to the tip, which has been introduced in previous papers [5-8]. This produces an emission current at considerably lower voltage compared to pure (virgin) tungsten cathodes. Cycling of the voltage provides reproducible I-V characteristics [7,8] with an improved stability [9,10] and a brighter spot [11].

The summary that is presented in this paper concerns our investigations carried out under high vacuum following the pressure 10^{-6} Pa and baking the system at 150–200 °C. In this work, all the experiments were carried out using a high-purity single/polycrystalline tungsten wire, due to its favorable properties, such as: high melting point, high hardness, high work function

and significant heat resistance at high temperatures [1-4].

Methods of Preparing Cathodes

Ultra-sharp tips used as a metallic substrate of epoxy-coated emitters were prepared by the same method based on electrolytic etching in both cases [1, 2]. For the electrolyte, a solution of 2–2.5 molar sodium hydroxide was used. After applying the two-phase etching method [4], the samples were cleaned by HF and ethylene (or isopropyl alcohol) in the first step. In the second step, the samples were further cleaned in water for a few minutes using ultrasonic bath in order to get rid of the contaminants originating from the electrochemical etching that are discussed further in the text. The composition of a typical cathode is obtained by Energy Dispersive X-ray spectroscopy (EDS), as illustrated in Fig. 1.

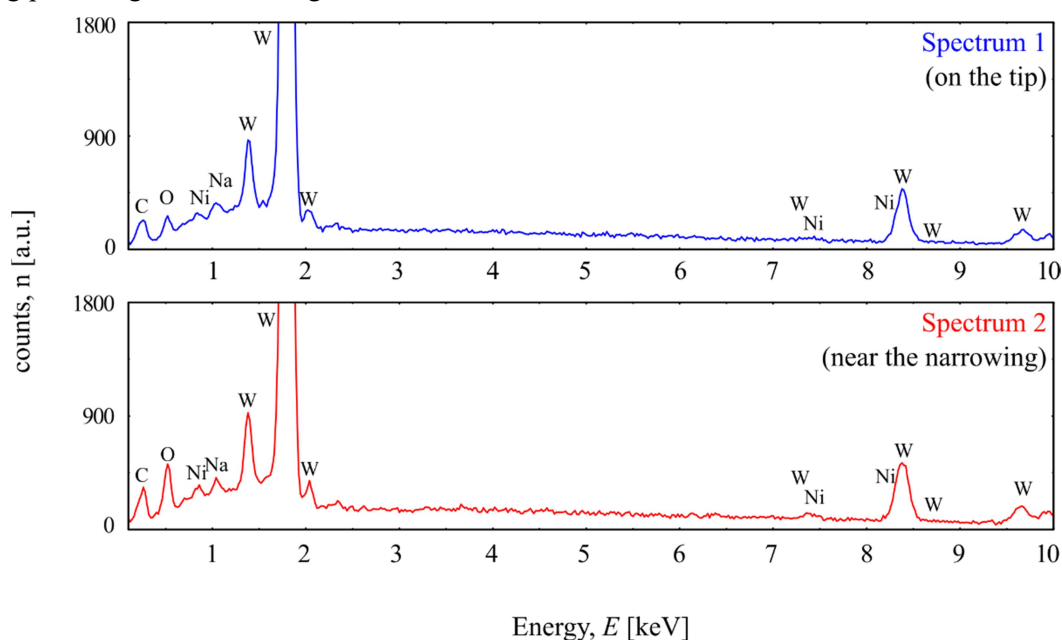


FIG. 1. The spectra of the SEM-EDS analysis for a sample coated by (478 Epoxy resin) a) EDS on the tip (blue). b) EDS in the area of wire narrowing (red).

From the results of the EDS analysis of the second emitter, it can be seen that even though tungsten predominates, there is a certain amount of contaminants present. The EDS spectrum was measured twice: on the coated surface (blue) and on the narrowing (uncoated area). Both measurements are comparable and show only a limited influence of the epoxy thin film on the chemical composition. Contaminants, such as Nickel (Ni) and Sodium (Na), originate from a

grounded electrode (cathode) that releases some of the components from its surface during the etching process.

These contaminants move from the cathode towards the etched tip and attach to the surface of the etched tip. Despite the fact that this analysis was performed only in the second study, it can be concluded that it goes also for the first study, since it depends on the chemical composition of the etched wire (that was pure

tungsten in both cases) and on the composition of the grounded electrode (that was steel in both cases as well).

After the final etching step, the tip was in both cases coated by epoxy resin: in the first paper, commercially available resin branded *EpoxyLite UPR-4* is used, whereas in the second paper, the *EpoxyLite 478* is used. In both cases, resins are cured in an electric furnace at two different phases, each at a different temperature. The first phase, where the temperature is usually about 100 °C, serves for degassing of the epoxy. The second phase serves for reaching the glass

transition temperature. Fig. 2 shows the emitters coated by using transmission electron microscopy (TEM) and scanning electron microscopy (SEM). The TEM shows a slight difference of the contrast between the dielectric layer and the metallic core. The SEM, on the other hand, shows surface contrast and hence the part of the tip that has been coated. Both methods are complementary and provide different information about coating. The coating method itself in both cases is based on dipping the tip in the epoxy and covering the very top of the tip by a homogeneous layer.

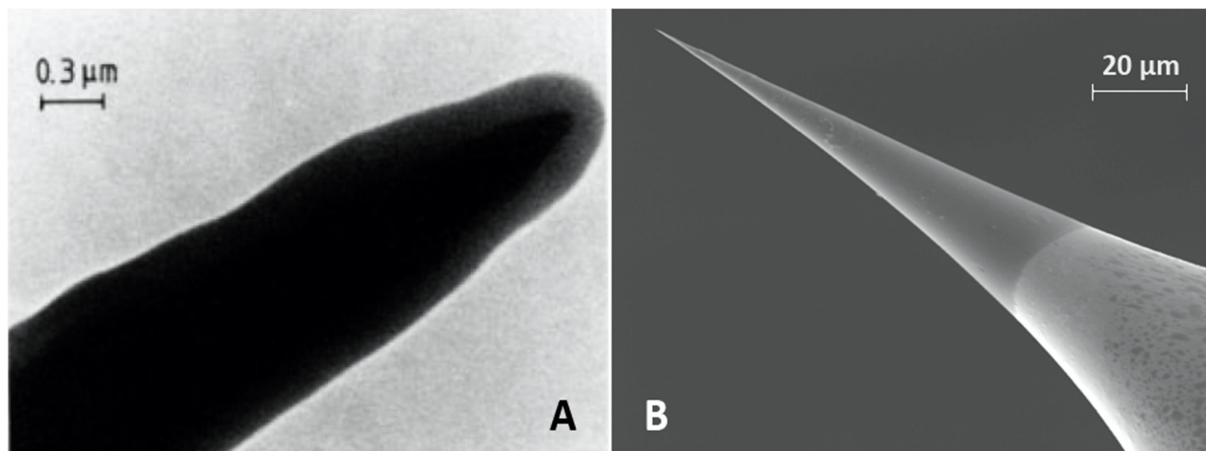


FIG. 2. a) TEM micrograph of W-tip coated by *EpoxyLite UPR-4* with a diameter of approx. 200 nm; b) SEM micrograph of W-tip coated by *EpoxyLite 478* with a diameter of approx. 20–30 nm.

In the first case, the tip is dipped twelve times into the *EpoxyLite UPR-4* epoxy, where the concentration ratio of the A and B components was 1:1. The single dip creates a layer that is approximately 15 nm thick. The ultra-sharp tips used as a metallic substrate of the epoxy-coated emitters were prepared by using the same method based on electrolytic etching in both cases [1, 2]. The layer thickness is approximately 200 nm. In the second case, the tip is dipped only once into the *EpoxyLite 478* which is a single component epoxy resin creating a layer of 20–30 nm thickness. Both epoxy resins are based on a *Bisphenol A diglycidyl ether* which is a colorless solid that melts slightly above room temperature. The UPR-4 is a two-component epoxy, whilst the 478 is a single-component epoxy. The difference in thickness amongst the two epoxy resins is caused mainly by different densities of the epoxy resins. In both cases, the tip is then subjected to a curing cycle. In the first case, the tip is baked directly in the vacuum chamber during the degassing procedure, whilst in the second case, the tip is

cured in the electric oven. The first part of the curing procedure takes thirty minutes at 100 °C to expel the solvents, followed by thirty minutes at 160 °C to complete the curing of the resin [2, 3]. In both cases, the epoxy resin undergoes glass transition and becomes a hard and relatively brittle “glassy” matter.

Comparison of the Experimental Results

In this part, the experimental results obtained by several methods are described and compared in more detail. Those methods are, in particular:

- Current-voltage (I-V) characterization and Fowler-Nordheim (F-N) analysis of the I-V data,
- Analysis of the switch-on phenomena and the emission patterns,
- Energy and noise spectral analysis of the electron beam.

a. Current-Voltage Characterization and Fowler-Nordheim Analysis

The I-V curve is used to determine basic parameters of the field-emission cathode and to model its behavior during operation. In Fig. 3, curve A shows the I-V characteristics for an uncoated tungsten emitter with a 30nm tip apex connected in a simple diode configuration. Compared to curve A, curve B represents the

characteristics of a coated tip by 200 nm of Epoxylite UPR-4 resin. It can be seen that the threshold voltage V_{th} decreased and an additional hysteresis appeared, slightly moving the characteristics toward higher current values when the applied voltage is increased in contrary to the opposite way. These effects have been already described and discussed in several papers [1, 5, 7].

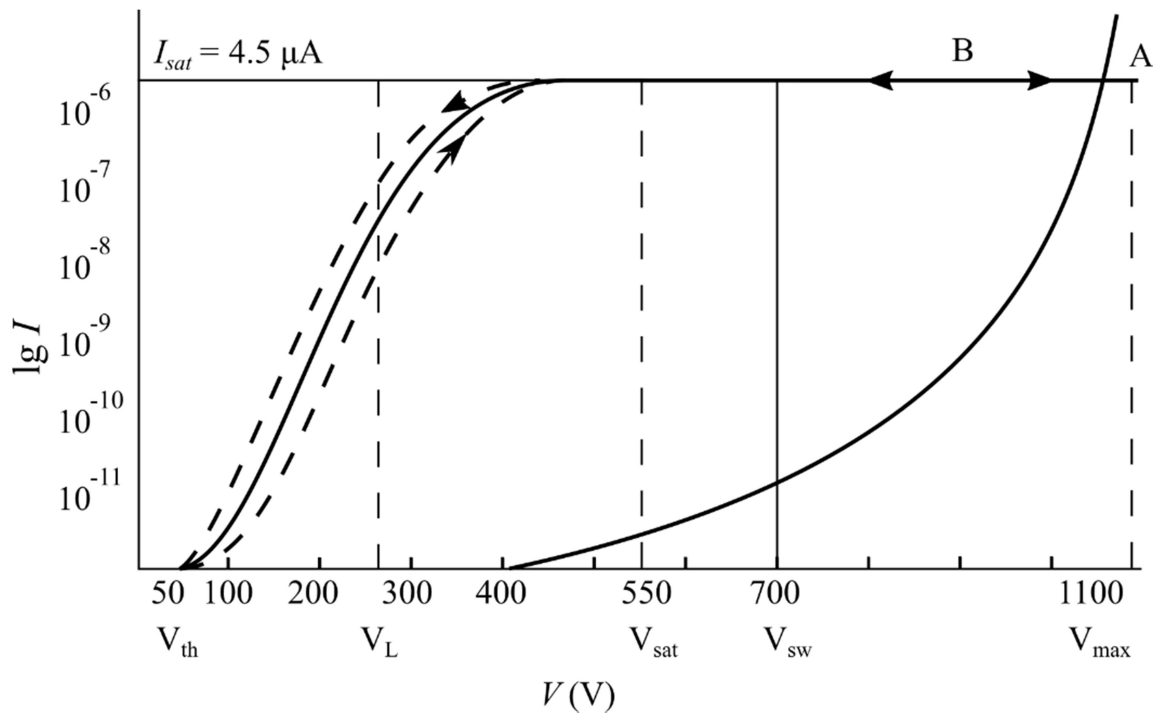


FIG. 3. A comparison of I-V characteristics of an uncoated (A) vs. coated (B) W-emitter of a tip radius of 30 nm and an epoxy coating of approx. 200 nm (UPR-4 Epoxylite resin).

Fig.4 shows the Fowler-Nordheim plots of the uncoated (curve A) and the resin-coated (Epoxylite UPR-4) sharp tip. The Fowler-Nordheim plot is the most common method of analyzing the I-V characteristics and it is used to graphically interpret and analyze data obtained from the theoretical equation derived by Fowler-Nordheim [11]. The original idea was to obtain an exact straight line of slope S_{FN} , which would be a ratio related to the parameters appearing in the exponent of a Fowler-Nordheim-type equation of I-V form by: $S_{FN} = -b\phi^{3/2}/\beta$; and therefore the knowledge of the work-function ϕ would enable the determination of field enhancement factor β and *vice versa*. From Fig. 4, a certain difference between slopes of lines representing uncoated (A) and coated (B) emitters can be seen. A decrease in the slope of the F-N plots of the coated cathode at room temperature is obtained with a factor β of 3 to 4. This also results in a decrease in the work

function ϕ with respect to that of the uncoated W-tip of 4.52 eV [5].

In Fig. 5, the left curve shows the I-V characteristic for a sample coated with (478 Epoxylite resin) [4, 8]. The cathode was measured in the triode mode incorporating an additional anode called *the extractor* electrode which is located close (approx. 0.75 mm) to the field emission tip. This configuration is used mostly for devices utilizing a focused electron beam, where it is possible to change the size of the cross-over simply by changing the ratio between voltages applied. The extractor electrode makes the electrons leave the surface and the additional (acceleration) energy is provided by the anode which serves as the main acceleration electrode here. The particular set-up and the precise measurement method is described in more detail by Knápek [4].

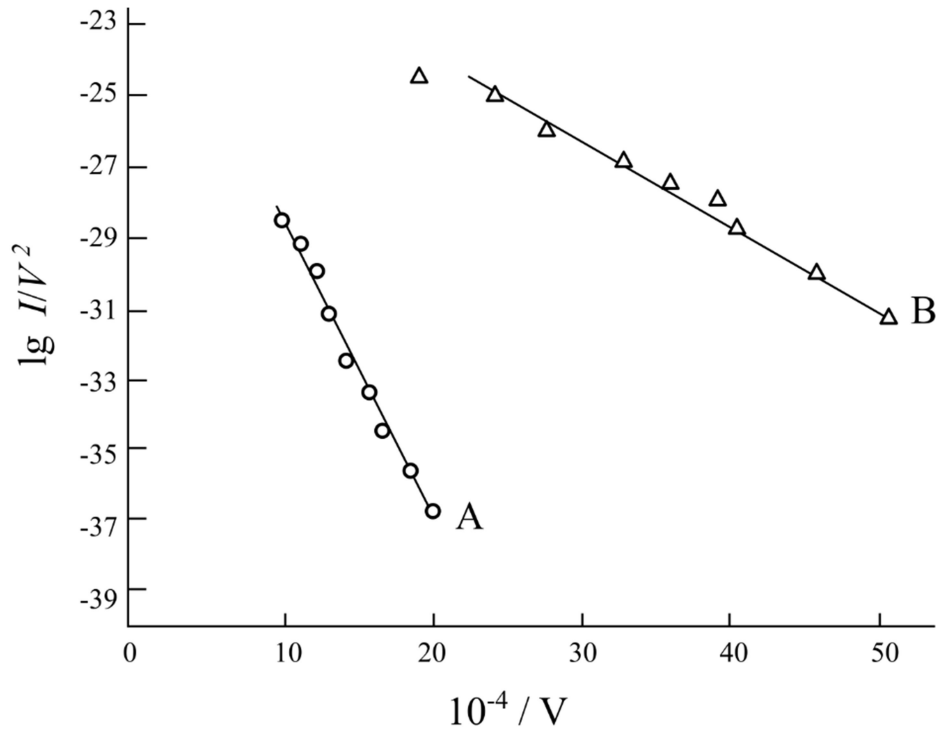


FIG. 4. The Fowler-Nordheim plots of the uncoated (curve A) and *Epoxylite UPR-4* coated tip (curve B).

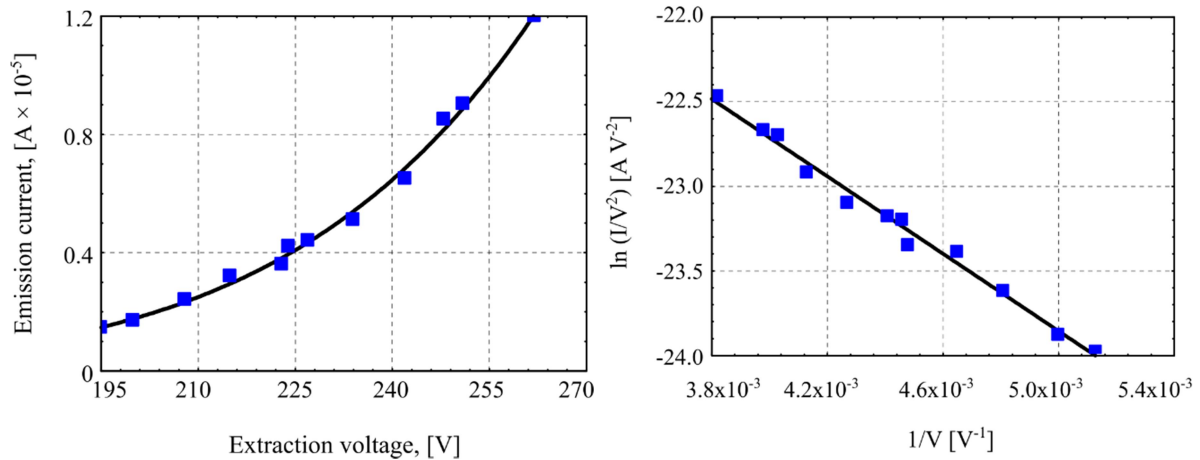


FIG. 5. Electrical characteristics of the tip coated by *Epoxylite 478*. Left: I-V characteristics of the emission current based on extraction voltage following exponential function. Right: calculated Fowler-Nordheim plot following linear slope.

The current-voltage measurements of the second sample are represented by Fig. 5 left (I-V characteristics) and right (F-N plot). Even though the I-V characteristics curve covers just a limited range of extraction voltages (195–270 V), it implies that the current there follows the same exponential function as the previous coated sample illustrated in Fig. 3. B. The difference of the nominal current is caused mainly by a different operation mode (the triode mode vs. the diode mode), by a different detection method (the Al-coated scintillation crystal vs.

phosphorus screen in the previous case) and by different coating where both layer thickness and different chemical structure affect the emission. In the F-N plot illustrated in the right part of Fig. 5, it can be seen that there is a certain similarity to the previous sample implying the same effect on the field emission. This effect was explained in more detail by Mousa [12].

The ideal thickness of the *Epoxylite 478* coating whose relative permittivity $\epsilon_r = 4$ has been theoretically calculated (based on WKB approximation) and found to be around 5 nm [2].

To conclude this part, the typical slope of a coated emitter is $\approx 1/4$ that of the uncoated tungsten emitter. The maximum voltage that may be applied for stable emission is typically twice the voltage required for saturated emission [1, 6, 8].

b. Analysis of Switch-on Phenomena and Emission Patterns

The initiation of the field emission is observed after a “switch-on” voltage has been applied to the tip. This produces a saturated emission current that can then be maintained at much lower voltages. A summary of the most important results was reviewed in a paper published by Mousa [5]. The projection images that appear on the screen are also referred to as emission patterns due to their geometric arrangement for single-crystalline emitters. In

each of the studies, the analysis of the emission pattern is made from a different point of view. For the first paper, the difference between virgin (uncoated) and coated emitters is analyzed, whilst for the second, the effect of the extractor voltage is analyzed for the coated emitter.

The field emission pattern displays the projected work function map of the emitter surface. The closely packed faces $\{110\}$, $\{100\}$, and $\{211\}$ have higher work functions than atomically rough regions and they thus appear in the image as dark spots on the brighter background (see Fig. 6. A). In the right part of the figure, the effect of epoxy coating can be seen creating a single emission region in the position of the facet $\{110\}$. This is one of the most important and interesting features of using the epoxy coating.

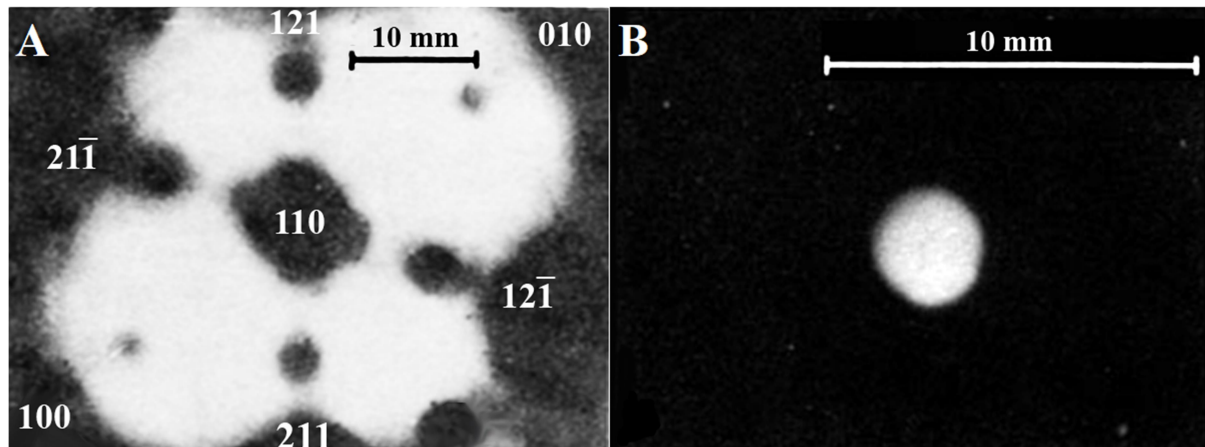


FIG. 6. Emission pattern obtained from a) the clean tungsten emitter and from b) the emitter that was coated by a 150nm layer of *Epoxylite UPR-4* resin. Both images were recorded with the same tip-to-screen separation and the same emission current of 4.5 pA [1, 6].

For the tips that were coated by Epoxylite 478 in the second work, it has been experimented with an increasing extractor voltage and its effect on the shape of the field-emission-active area. Instead of the phosphorus screen used in the previous case, in this case, a Cerium-doped Yttrium Aluminium garnet was used to display the emission pattern and to conduct a constant part of the electron beam that has been used for analysis. The measurement is illustrated in Fig. 7, showing 4 extracting V_{ex}

voltages and the corresponding spot size d . It has been found out that the intensity of the spot size is equally distributed and the shape is equidistant in respect to the optical axis. Another pursued parameter is the relative light intensity that is a parameter based on the number of photons impinging on the surface of the CCD chip of a camera used to record the image, which is expressed in percents. Authors have found out that the relative light intensity L follows the linear function [2].

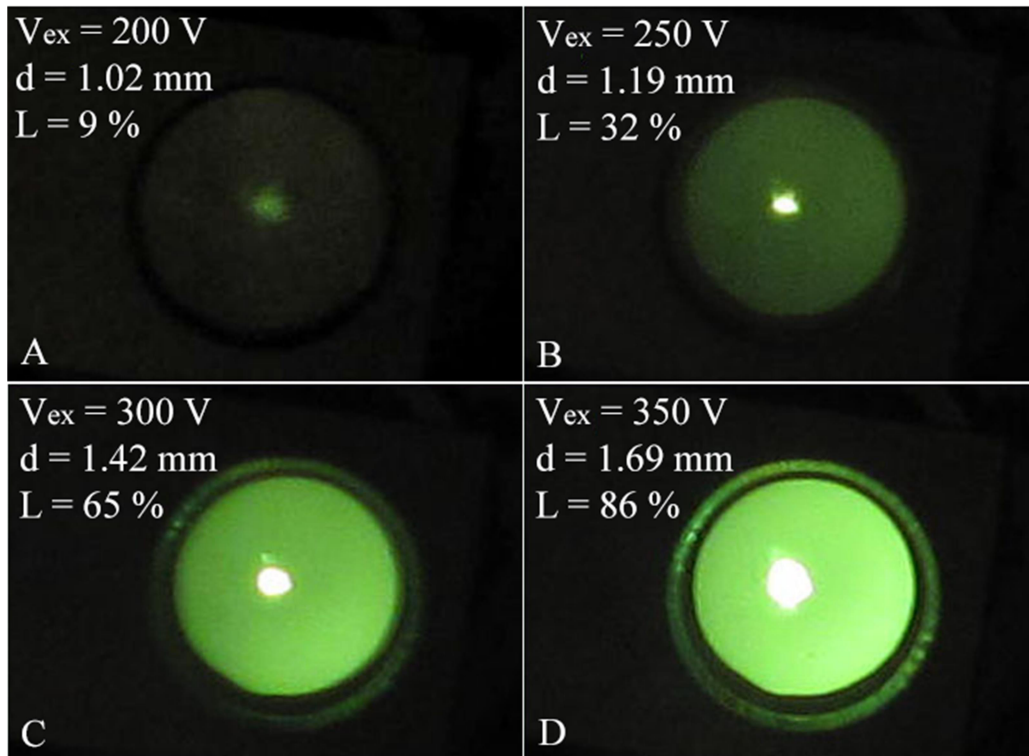


FIG. 7. The emission patterns vs. the extraction voltage for the sample coated by *EpoxyLite 478* resin [8].

c. Energy and Noise Spectral Analysis of the Electron Beam

The electron spectra were measured only for the cathodes coated by EpoxyLite UPR-4 to provide important information on the emission mechanism associated with the composite regimes. The measurements were performed using a well-known retarding potential analyzer design of Van Oostrom (1966), but incorporating fully automated electronically controlled drive and detection systems [1]. In particular, a lock-in

amplifier technique was used to obtain a direct differential spectral output providing an output that is comparable to the more widely used hemispherical type of analyzer [1].

Fig. 8 illustrates and compares the energy spectra obtained from a tungsten emitter before (A) and after (B) coating with a 200nm thick layer of the EpoxyLite UPR-4 resin. In both cases, the emission currents were equal to 4 pA.

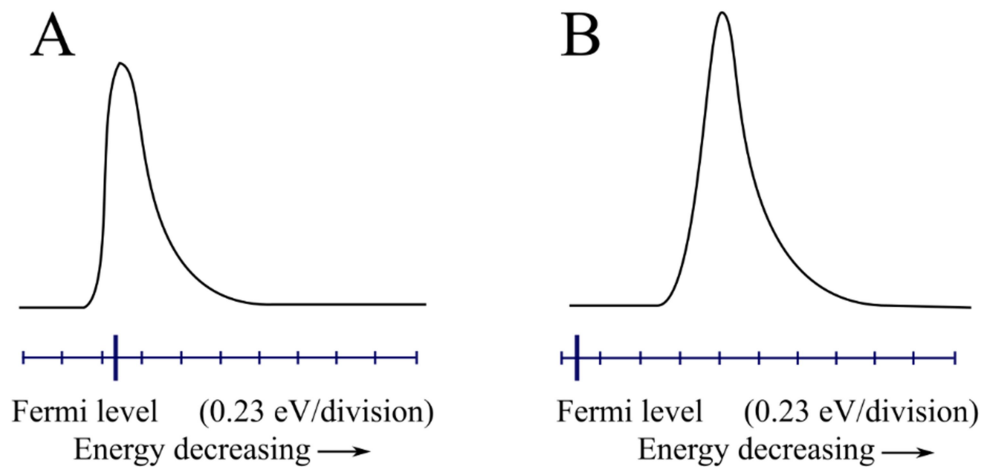


FIG. 8. A comparison of the energy spectra obtained from the tungsten emitter (a) before and (b) after coating with a 150 nm thick layer of resin at identical emission currents of 4 pA.

These results have shown that with respect to the Fermi level, the spectrum obtained in the metal cathode is displaced towards lower energies by approx. 0.7 eV and that the composite emitter has a significantly larger full width at half-maximum compared to the uncoated one. Last, but not least, the measurements showed that the spectrum of the composite emitter is more symmetrical compared to the clean tungsten tip [1, 5].

In the second case, for the Epoxylite 478-coated tip, the electron beam was analyzed using a method that is based on evaluating the slope of the power noise spectral density spectrum of the total emission current. This method is mostly used for semiconductor analysis and it is obtained by performing the Fourier transformation on the sampled emission current. From the slope of the spectrum at particular frequency bands, it is possible to identify processes responsible for particular events that are responsible for the noise at the quantum level. The precise method was described by Knápek [10].

From the measurements shown in Fig. 9, it is evident that the power spectral density of whole spectra is being slowly increased in time and that the slope is staying constant. From the slope, which is constantly about 1.5, it is evident that the measured noise has characteristics of the so-called $1/f$ (flickering) noise. The $1/f$ noise is a process with a frequency spectrum, such that the power spectral density is proportional to the reciprocal of the frequency. We can see that, for the red curve, the parameters changed to $a = 1.5 \times 10^{-4}$, the slope $n = -1.3$ and the time constant remains the same, $b = 1 \times 10^{-3}$ s. In conclusion, the period τ between each hop to the different energy level is computed as 1.59×10^{-4} s. The cutting frequency is located near 1000 Hz. The $1/f^n$ noise (where $n > 1$) originates from the superposition of particular $1/f$ and generation-recombination (G-R) processes which originate from adsorption and desorption of various atoms present with some residual gas in the vacuum chamber.

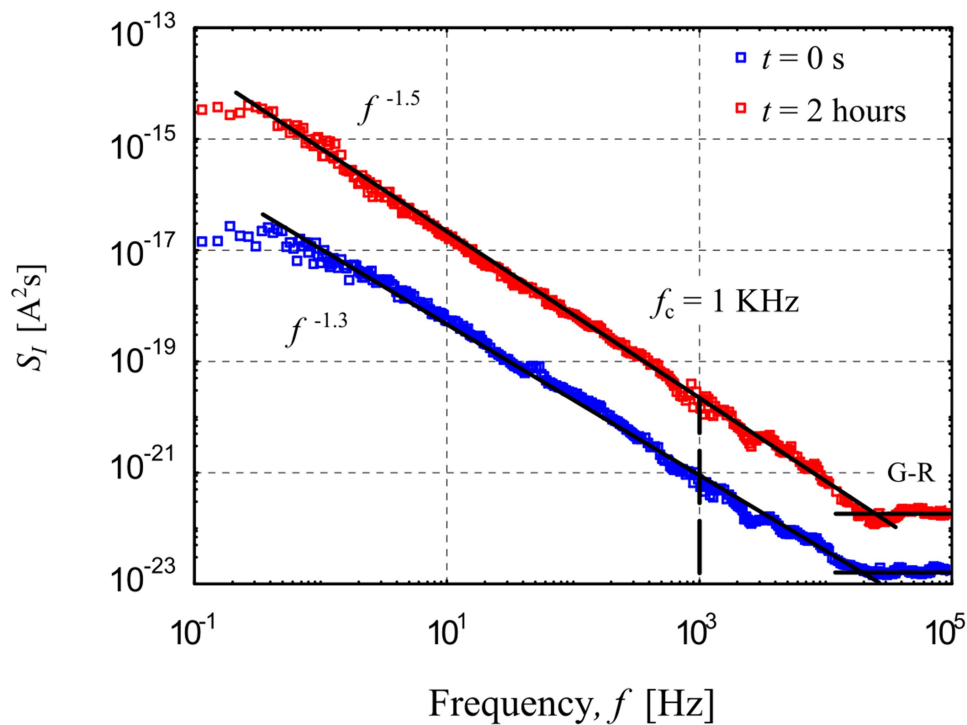


FIG. 9. A comparison of long-time noise power spectrum density measured at $V_{ex} = 200$ V, from $t = 0$ s (blue) to $t = 120$ min (red).

The results suggest that the ions which are bombarding the cathode's surface can be observed from the noise measurement as well. They prove themselves by random *burst noise*. The bombardment reduces the epoxy layer, which leads to its unavoidable damage. The

noise spectral density (where the $1/f$ noise prevails) changes to $1/f^n$, where n is located between 1 and 2. In general, the $1/f^n$ noise originates from the superposition of particular $1/f$ and generation-recombination (G-R) processes. Therefore, the higher the n , the more significant

the G-R. Generation-recombination is caused mostly by the chemisorption of the ion residuals present in the chamber. These effects of chemisorption are unavoidable, since only the surface on the tip is protected by the epoxy layer.

Conclusions

In this paper, two similar studies have been compared with the emphasis on similar features, confirming the excellent field emission behavior of the dielectric-coated emitter tip. This is a prospective candidate for a future advanced electron field emitter.

Amongst the most suitable attributes, the most interesting are the low operating voltages and the high current densities. The resin coating protects the surface of the emission plane from unwanted chemical or physical sorption of ions which are attracted backwards towards the cathode and cause a massive bombardment of the tip. This protection enables the cathode to

work at lower vacuum than for classical field emission. The coating also slightly reduces the emission current, making the energy more symmetrically distributed compared to the distribution of the uncoated emitter. The epoxy influence of the coating thickness on emission stability will be discussed later in a follow-up publication. For now, it can be concluded that the coating is very thin. Epoxy coating also causes a decrease in the beam energy spectrum which is lower by ≈ 0.7 eV with respect to the Fermi level of the metallic cathode, as we can see in the electron spectra.

Acknowledgements

From the Czech part: The research was supported by the Ministry of Industry and Trade of the Czech Republic, MPO-TRIO project FV10618. The research infrastructure was funded by the Czech Academy of Sciences (project RVO:68081731).

References

- [1] Mousa, M.S. and Latham, R.V., *Le Journal de Physique Colloques*, 47 (C7) (1986) C7-139.
- [2] Knápek, A. and Grmela, L., "Methods of Preparation and Characterisation of Experimental Field-Emission Cathodes", (Brno University of Technology, Brno, Czech Republic, 2013).
- [3] Knápek, A. and Grmela, L., *Chemické Listy*, 107 (7) (2013) 545.
- [4] Knápek, A. et al., *Microelectronic Engineering*, 173 (2017) 42.
- [5] Mousa, M.S., Karpowicz, A. and Surma, S., *Vacuum*, 45 (2-3) (1994) 249.
- [6] Al-Qudah, A.A., Mousa, M.S. and Fischer, A., *IOP Conference Series: Materials Science and Engineering*, 92 (2015) 012021.
- [7] Mousa, M.S., *Surface Science*, 231 (1-2) (1990) 142.
- [8] Mousa, M.S., *Surface and Interface Analysis*, 39 (2-3) (2007) 102.
- [9] Latham, R.V. and Salim, M.A., *Journal of Physics E: Scientific Instruments*, 20 (2) (1987) 181.
- [10] Knápek, A. et al., *Metrology and Measurement Systems*, 19 (2) (2012) 417.
- [11] Forbes, R.G. et al., *Journal of Vacuum Science & Technology B: Microelectronics and Nanometer Structures Processing, Measurement and Phenomena*, 22 (3) (2004) 1222.
- [12] Mousa, M.S., *Le Journal de Physique Colloques*, 48 (C6) (1987) C6-115.

Authors Index

A. A. Barzinjy	123
A. Benyoussef	149
A. Kara	149
A. Knápek	93, 171
A. Mahmoud	149
A. Oueriagli	113
A.M.D. Assa'd	137
F. Al-Mokdad	165
F. Boschini	149
F. ElManjli	149
G. Tiouitchi	149
H. Basma	165
H. H. Azeez	123
H. Kawariq	137
H. Oughaddou	149
J. Chlumská	93
L. C. Costa	113, 157
L. Grmela	171
M. Ait Ali	149
M. Drozd	93
M. E. Achour	113, 157
M. El Hasnaoui	157
M. Hamedoun	149
M. M. Allaham	101
M. Matějka	93
M. S. Mousa	101, 171
N. Aribou	157
N. Éber	113
O. Mounkachi	149
R. Awad	165
R. Belhimria	113
R. G. Forbes	101
S. Barnoss	157
S. Boukheir	113
S. Král	93
S. M. Hamad	123
V. Kolařík	93
Z. Samir	113

Subject Index

2D materials	149
Ac-conductivity.....	165
Applications	123
Backscattering electron coefficient	137
Black phosphorus	149
Carbon nanotubes	113
Cold field emission.....	171
Composites.....	113
Compositional contrast.....	137
Conducting polymer.....	157
Crystallinity	157
Dielectric constants	165
Elastic scattering	137
Epoxy lite 478	171
Epoxy lite EPR-4.....	171
Equivalent circuit model	113
Field electron emission.....	101
Field emission	101
Fowler-Nordheim plot.....	101
Grain effect.....	113
Grain-boundary effect	113
Impedance spectroscopy.....	113
Liquid-phase exfoliation	149
Millikan-Lauritsen plot	101
Monte Carlo model.....	137
Murphy-Good plot.....	101
Nanoparticles.....	123
Non-patterned wafer.....	93
Optical inspection.....	93
Orthodoxy test.....	101
Percolation threshold.....	157
Phosphorene	149
Quality control	93
Red phosphorus.....	149
Resist layer.....	93
Si-Ge/Si	137
Spatial resolution.....	137
Structure	123
Synthesis	123
Thermal degradation	157
X-Ray diffraction	157
XRD	165
Zinc oxide.....	165
ZnO	123

المراجع: يجب طباعة المراجع بأسطر مزدوجة ومرقمة حسب تسلسلها في النص. وتكتب المراجع في النص بين قوسين مربعين. ويتم اعتماد اختصارات الدوريات حسب نظام Wordlist of Scientific Reviewers.

الجدول: تعطى الجداول أرقاماً متسلسلة يشار إليها في النص. ويجب طباعة كل جدول على صفحة منفصلة مع عنوان فوق الجدول. أما الحواشي التفسيرية، التي يشار إليها بحرف فوقي، فتكتب أسفل الجدول.

الرسوم التوضيحية: يتم ترقيم الأشكال والرسومات والرسومات البيانية (المخططات) والصور، بصورة متسلسلة كما وردت في النص.

تقبل الرسوم التوضيحية المستخرجة من الحاسوب والصور الرقمية ذات النوعية الجيدة بالأبيض والأسود، على أن تكون أصيلة وليست نسخة عنها، وكل منها على ورقة منفصلة ومعرفة برقمها بالمقابل. ويجب تزويد المجلة بالرسومات بحجمها الأصلي بحيث لا تحتاج إلى معالجة لاحقة، وألا تقل الحروف عن الحجم 8 من نوع Times New Roman، وألا تقل سماكة الخطوط عن 0.5 وبكثافة متجانسة. ويجب إزالة جميع الألوان من الرسومات ما عدا تلك التي ستنتشر ملونة. وفي حالة إرسال الرسومات بصورة رقمية، يجب أن تتوافق مع متطلبات الحد الأدنى من التمايز (1200 dpi Resolution) لرسومات الأبيض والأسود الخطية، و 600 dpi للرسومات باللون الرمادي، و 300 dpi للرسومات الملونة. ويجب تخزين جميع ملفات الرسومات على شكل (jpg)، وأن ترسل الرسوم التوضيحية بالحجم الفعلي الذي سيظهر في المجلة. وسواء أرسل المخطوط بالبريد أو عن طريق الشبكة (Online)، يجب إرسال نسخة ورقية أصلية ذات نوعية جيدة للرسومات التوضيحية.

مواد إضافية: تشجع المجلة الباحثين على إرفاق جميع المواد الإضافية التي يمكن أن تسهل عملية التحكيم. وتشمل المواد الإضافية أي اشتقاقات رياضية مفصلة لا تظهر في المخطوط.

المخطوط المنقح (المعدل) والأقراص المدمجة: بعد قبول البحث للنشر وإجراء جميع التعديلات المطلوبة، فعلى الباحثين تقديم نسخة أصلية ونسخة أخرى مطابقة للأصلية مطبوعة بأسطر مزدوجة، وكذلك تقديم نسخة إلكترونية تحتوي على المخطوط كاملاً مكتوباً على Microsoft Word for Windows 2000 أو ما هو استجد منه. ويجب إرفاق الأشكال الأصلية مع المخطوط النهائي المعدل حتى لو تم تقديم الأشكال إلكترونياً. وتخزن جميع ملفات الرسومات على شكل (jpg)، وتقدم جميع الرسومات التوضيحية بالحجم الحقيقي الذي ستظهر به في المجلة. ويجب إرفاق قائمة ببرامج الحاسوب التي استعملت في كتابة النص، وأسماء الملفات على قرص مدمج، حيث يعلم القرص بالاسم الأخير للباحث، وبالرقم المرجعي للمخطوط للمراسلة، وعنوان المقالة، والتاريخ. ويحفظ في مغلف وق.



حقوق الطبع

يُشكّل تقديم مخطوط البحث للمجلة اعترافاً صريحاً من الباحثين بأن مخطوط البحث لم يُنشر ولم يُقدّم للنشر لدى أي جهة أخرى كانت وبأي صيغة ورقية أو إلكترونية أو غيرها. ويُشترط على الباحثين ملء نموذج ينصّ على نقل حقوق الطبع لتصبح ملكاً لجامعة اليرموك قبل الموافقة على نشر المخطوط. ويقوم رئيس التحرير بتزويد الباحثين بنموذج نقل حقوق الطبع مع النسخة المُرسلة للتتقيق. كما ويُمنع إعادة إنتاج أي جزء من الأعمال المنشورة في المجلة من دون إذن خطّي مُسبق من رئيس التحرير.

إخلاء المسؤولية

إن ما ورد في هذه المجلة يعبر عن آراء المؤلفين، ولا يعكس بالضرورة آراء هيئة التحرير أو الجامعة أو سياسة اللجنة العليا للبحث العلمي أو وزارة التعليم العالي والبحث العلمي. ولا يتحمل ناشر المجلة أي تبعات مادية أو معنوية أو مسؤوليات عن استعمال المعلومات المنشورة في المجلة أو سوء استعمالها.

الفهرسة: المجلة مفهرسة في:

 ULRICHSWEB™ GLOBAL SERIALS DIRECTORY	Emerging Sources Citation Index (ESCI)	
--	---	---

المجلة الأردنية للفيزياء هي مجلة بحوث علمية عالمية متخصصة مُحكمة تصدر بدعم من صندوق دعم البحث العلمي، وزارة التعليم العالي والبحث العلمي، عمان، الأردن. وتقوم بنشر المجلة عمادة البحث العلمي والدراسات العليا في جامعة اليرموك، إربد، الأردن. وتنتشر البحوث العلمية الأصلية، إضافة إلى المراسلات القصيرة Short Communications، والملاحظات الفنية Technical Notes، والمقالات الخاصة Feature Articles، ومقالات المراجعة Review Articles، في مجالات الفيزياء النظرية والتجريبية، باللغتين العربية والإنجليزية.

تقديم مخطوط البحث

تقدم البحوث عن طريق إرسالها إلى البريد الإلكتروني : jjp@yu.edu.jo

تقديم المخطوطات إلكترونياً: اتبع التعليمات في موقع المجلة على الشبكة العنكبوتية.

ويجري تحكيمُ البحوث الأصلية والمراسلات القصيرة والملاحظات الفنية من جانب مُحكمين اثنين في الأقل من ذوي الاختصاص والخبرة. وتُشجّع المجلة الباحثين على اقتراح أسماء المحكمين. أما نشر المقالات الخاصة في المجالات الفيزيائية النشطة، فيتم بدعوة من هيئة التحرير، ويُشار إليها كذلك عند النشر. ويُطلب من كاتب المقال الخاص تقديم تقرير واضح يتسم بالدقة والإيجاز عن مجال البحث تمهيداً للمقال. وتنتشر المجلة أيضاً مقالات المراجعة في الحقول الفيزيائية النشطة سريعة التغير، وتشجّع كاتبي مقالات المراجعة أو مُستكثبيها على إرسال مقترح من صفحتين إلى رئيس التحرير. ويُرفق مع البحث المكتوب باللغة العربية ملخص (Abstract) وكلمات دالة (Keywords) باللغة الإنجليزية.

ترتيب مخطوط البحث

يجب أن تتم طباعة مخطوط البحث ببنت 12 نوعه Times New Roman، وبسطر مزدوج، على وجه واحد من ورق A4 (21.6 × 27.9 سم) مع حواشي 3.71 سم، باستخدام معالج كلمات ميكروسوفت وورد 2000 أو ما استُجد منه. ويجري تنظيم أجزاء المخطوط وفق الترتيب التالي: صفحة العنوان، الملخص، رموز التصنيف (PACS)، المقدمة، طرق البحث، النتائج، المناقشة، الخلاصة، الشكر والعرفان، المراجع، الجداول، قائمة بدليل الأشكال والصور والإيضاحات، ثم الأشكال والصور والإيضاحات. وتُكتب العناوين الرئيسية بخط غامق، بينما تُكتب العناوين الفرعية بخط مائل.

صفحة العنوان: وتشمل عنوان المقالة، أسماء الباحثين الكاملة وعناوين العمل كاملة. ويكتب الباحث المسؤول عن المراسلات اسمه مشاراً إليه بنجمة، والبريد الإلكتروني الخاص به. ويجب أن يكون عنوان المقالة موجزاً وواضحاً ومعبراً عن فحوى (محتوى) المخطوط، وذلك لأهمية هذا العنوان لأغراض استرجاع المعلومات.

الملخص: المطلوب كتابة فقرة واحدة لا تزيد على مائتي كلمة، موضحة هدف البحث، والمنهج المتبع فيه والنتائج وأهم ما توصل إليه الباحثون.

الكلمات الدالة: يجب أن يلي الملخص قائمة من 4-6 كلمات دالة تعبر عن المحتوى الدقيق للمخطوط لأغراض الفهرسة.

PACS: يجب إرفاق الرموز التصنيفية، وهي متوفرة في الموقع <http://www.aip.org/pacs/pacs06/pacs06-toc.html>.

المقدمة: يجب أن توضّح الهدف من الدراسة وعلاقتها بالأعمال السابقة في المجال، لا أن تكون مراجعة مكثفة لما نشر (لا تزيد المقدمة عن صفحة ونصف الصفحة مطبوعة).

طرائق البحث (التجريبية / النظرية): يجب أن تكون هذه الطرائق موضحة بتفصيل كاف لإتاحة إعادة إجرائها بكفاءة، ولكن باختصار مناسب، حتى لا تكون تكراراً للطرائق المنشورة سابقاً.

النتائج: يستحسن عرض النتائج على صورة جداول وأشكال حيثما أمكن، مع شرح قليل في النص ومن دون مناقشة تفصيلية.

المناقشة: يجب أن تكون موجزة وتركز على تفسير النتائج.

الاستنتاج: يجب أن يكون وصفاً موجزاً لأهم ما توصلت إليه الدراسة ولا يزيد عن صفحة مطبوعة واحدة.

الشكر والعرفان: الشكر والإشارة إلى مصدر المنح والدعم المالي يكتبان في فقرة واحدة تسبق المراجع مباشرة.

Jordan Journal of

PHYSICSAn International Peer-Reviewed Research Journal issued by the
Support of the Scientific Research Support Fund

Published by the Deanship of Research & Graduate Studies, Yarmouk University, Irbid, Jordan

Name: الأسم:
 Specialty: التخصص:
 Address: العنوان:
 P.O. Box: صندوق البريد:
 City & Postal Code: المدينة/الرمز البريدي:
 Country: الدولة:
 Phone: رقم الهاتف:
 Fax No: رقم الفاكس:
 E-mail: البريد الإلكتروني:
 No. of Subscription: عدد الاشتراكات:
 Method of Payment: طريقة الدفع:
 Amount Enclosed: المبلغ المرفق:
 Signature: التوقيع:

Cheques should be paid to Deanship of Research and Graduate Studies - Yarmouk University.

I would like to subscribe to the Journal
For

- ☐ One Year
☐ Two Years
☐ Three Years

One Year Subscription Rates

	Inside Jordan	Outside Jordan
Individuals	JD 8	€ 40
Students	JD 4	€ 20
Institutions	JD 12	€ 60

Correspondence**Subscriptions and Sales:**

Prof. Ibrahim O. Abu Al-Jarayesh
 Deanship of Research and Graduate Studies
 Yarmouk University
 Irbid – Jordan
Telephone: 00 962 2 711111 Ext. 2075
Fax No.: 00 962 2 7211121



جامعة اليرموك



المملكة الأردنية الهاشمية

المجلة الأردنية
للفيزياء

مجلة بحوث علمية عالمية متخصصة محكمة
تصدر بدعم من صندوق دعم البحث العلمي

المجلة الأردنية
للفيزياء
مجلة بحوث علمية عالمية محكمة

المجلد (13)، العدد (2)، آب 2020م / محرم 1442هـ

المجلة الأردنية للفيزياء: مجلة علمية عالمية متخصصة محكمة تصدر بدعم من صندوق دعم البحث العلمي، عمان، الأردن، وتصدر عن عمادة البحث العلمي والدراسات العليا، جامعة اليرموك، إربد، الأردن.

رئيس التحرير:

ابراهيم عثمان أبو الجرايش

قسم الفيزياء، جامعة اليرموك، إربد، الأردن.

ijaraysh@yu.edu.jo

هيئة التحرير:

نبيل يوسف أيوب

رئيس الجامعة الأمريكية في مادبا، مادبا، الأردن.

nabil.ayoub@gju.edu.jo

جميل محمود خليفة

قسم الفيزياء، الجامعة الأردنية، عمان، الأردن.

jkalifa@ju.edu.jo

طارق فتحي حسين

قسم الفيزياء، الجامعة الأردنية، عمان، الأردن.

t.hussein@ju.edu.jo

مروان سليمان موسى

قسم الفيزياء، جامعة مؤتة، الكرك، الأردن.

mmousa@mutah.edu.jo

محمد خالد الصغير

قسم الفيزياء، الجامعة الهاشمية، الزرقاء، الأردن.

msugh@hu.edu.jo

عبد المجيد الياسين

قسم الفيزياء، جامعة اليرموك، إربد، الأردن.

alyassin@yu.edu.jo

محمد العمري

قسم الفيزياء، جامعة العلوم والتكنولوجيا، إربد، الأردن.

alakmoh@just.edu.jo

إبراهيم البصول

قسم الفيزياء، جامعة آل البيت، المفرق، الأردن.

Ibrahimbsoul@yahoo.com

سكرتير التحرير: مجدي الشناق

ترسل البحوث إلى العنوان التالي:

الأستاذ الدكتور إبراهيم عثمان أبو الجرايش
رئيس تحرير المجلة الأردنية للفيزياء
عمادة البحث العلمي والدراسات العليا، جامعة اليرموك
إربد، الأردن

هاتف 00 962 2 7211111 فرعي 2075

E-mail: jjp@yu.edu.jo Website: <http://Journals.yu.edu.jo/jjp>